DSM-BASED PREDICTION OF DISTORTIONAL FAILURE LOADS OF
COLD-FORMED STEEL COLUMNS AT ELEVATED TEMPERATURES

Fernanda Cristina Moreira da Silva Costa

Tese de Doutorado apresentada ao Programa de
Pós-graduação em Engenharia Civil, COPPE, da
Universidade Federal do Rio de Janeiro, como
parte dos requisitos necessários à obtenção do
título de Doutor em Engenharia Civil.

Orientadores: Alexandre Landesmann
　　　　　　　　Dinar Reis Zamith Camotim

Rio de Janeiro
Setembro de 2019

DSM-BASED PREDICTION OF DISTORTIONAL FAILURE LOADS OF COLD-FORMED STEEL COLUMNS AT ELEVATED TEMPERATURES

Fernanda Cristina Moreira da Silva Costa

TESE SUBMETIDA AO CORPO DOCENTE DO INSTITUTO ALBERTO LUIZ COIMBRA DE PÓS-GRADUAÇÃO E PESQUISA DE ENGENHARIA (COPPE) DA UNIVERSIDADE FEDERAL DO RIO DE JANEIRO COMO PARTE DOS REQUISITOS NECESSÁRIOS PARA A OBTENÇÃO DO GRAU DE DOUTOR EM CIÊNCIAS EM ENGENHARIA CIVIL.

Examinada por:

_____
Prof. Alexandre Landesmann, D.Sc.

_____
Prof. Eduardo de Miranda Batista, D.Sc.

_____
Prof. Wendell Diniz Varela, D.Sc.

_____
Profª. Eliane Maria Lopes Carvalho, D.Sc.

_____
Prof. Luciano Rodrigues Ornelas de Lima, D.Sc.

RIO DE JANEIRO, RJ - BRASIL
SETEMBRO DE 2019

A Deus, por tudo,

Aos meus pais, Jobel e Rosenir, e meus irmãos, Renata e Rafael,

Ao meu marido, Rafael.

Agradecimentos

A Deus, por ter me iluminado ao longo de toda a minha trajetória acadêmica e por ter me dado saúde e força para que eu conseguisse cumprir mais uma etapa tão importante na minha vida.

Aos meus orientadores, Prof. Alexandre Landesmann e Prof. Dinar Camotim, pelo conhecimento compartilhado. Em especial ao Prof. Alexandre, pelo apoio e orientação que me dedicou durante o desenvolvimento de cada etapa deste trabalho. Obrigada pelos conselhos, pela paciência, pela pronta disponibilidade, por não medir esforços para garantir a continuação das pesquisas de cada aluno do grupo e por nos mostrar, a cada dia, a importância do trabalho de qualidade. O seu constante incentivo para buscarmos sempre evoluir dentro da área acadêmica fez (e continuará fazendo) toda diferença na minha caminhada. Certamente, concluo esta etapa mais madura.

Ao meu marido, Rafael, pelo apoio e carinho incondicionais que me dedica a cada dia. Obrigada pelos incentivos incansáveis, por não me deixar esmorecer, por acreditar que eu chegaria aqui, pela paciência, por me trazer para o "eixo" sempre que preciso e me fazer enxergar o lado racional dos problemas. Por fim, obrigada pela compreensão e companhia nos inúmeros finais de semana de estudo e dedicação, mesmo sendo estes os nossos únicos dias juntos. Sua participação em todos os momentos (mesmo de longe, muitas vezes) me deu muito suporte e tornou esta caminhada mais feliz. Te amo muito.

Aos meus pais, Jobel e Rosenir, minha base e meus maiores exemplos, pelo suporte, educação, amor e carinho, que sempre me dedicaram. Obrigada por me apoiarem nos momentos difíceis e por estarem sempre a postos para qualquer necessidade. Aos meus irmãos, Renata e Rafael, meus eternos companheiros, pelos momentos maravilhosos. À minha avó, Maria Tosca, pelo carinho e pelas orações. Amo muito todos vocês.

Às minhas queridas amigas, Gabriela e Monique, que me acompanharam diariamente nesses anos do curso de doutorado. Conhecê-las foi um dos melhores presentes que o doutorado me trouxe. Obrigada pela amizade, pela companhia, pelo apoio e carinho em momentos muito difíceis, pelas experiências/convivência maravilhosas dentro e fora da COPPE. E, mais que tudo, obrigada pelas melhores risadas, pelos cafés e almoços animados, enfim, pela alegria que nos uniu e nos ajuda a seguir em frente de forma mais leve. Aos meus colegas da COPPE, Marcela, Natasha, Carol, Ana, Pedro, Laila, Andréa e Mariana, pela convivência sempre muito agradável e produtiva.

Ao CNPq, pelo suporte financeiro durante a primeira fase do doutorado. À FAPERJ, pelo importante apoio financeiro na segunda fase da pesquisa. Sem dúvida, estes auxílios foram essenciais para a realização deste trabalho. Sou grata também à coordenação do PEC, que me indicou para bolsa da FAPERJ, e à equipe da secretaria do PEC, que sempre colaborou comigo.

À UFRJ, por toda a minha formação acadêmica, desde a graduação, o mestrado e, agora, o doutorado. Minha sincera gratidão aos professores que contribuíram brilhantemente para a minha capacitação e que, certamente, fizeram a diferença tanto na minha carreira acadêmica como na profissional. Tenho um carinho enorme por esta instituição.

Resumo da Tese apresentada à COPPE/UFRJ como parte dos requisitos necessários para a obtenção do grau de Doutor em Ciências (D.Sc.)

RESISTÊNCIA SEGUNDO MRD DE COLUNAS DE AÇO EM PERFIL FORMADO A FRIO SOB MODO DE FALHA DISTORCIONAL EM ALTAS TEMPERATURAS

Fernanda Cristina Moreira da Silva Costa

Setembro/2019

Orientadores: Alexandre Landesmann

Dinar Reis Zamith Camotim

Programa: Engenharia Civil

O presente trabalho é dedicado à investigação numérica do comportamento estrutural e da resistência de colunas de aço em perfil formado a frio submetidas ao modo de falha distorcional sob altas temperaturas, considerando o Método da Resistência Direta (MRD) para efeitos de dimensionamento. Os resultados obtidos através de análises com elementos finitos de casca no programa ANSYS abrangem colunas com (*i*) dois tipos de condições de apoio (fixado e simplesmente apoiado), (*ii*) seção transversal em formato U enrijecido com diferentes dimensões (relação alma/mesa ~ *0.7*, *1.0* e *1.4*), (*iii*) diversos valores de tensão de escoamento em temperatura ambiente (esbeltez distorcional até ~ *3.5*), (*iv*) imperfeições geométricas iniciais sob modo crítico distorcional com pequenas amplitudes, e (*v*) sujeitas a oito temperaturas uniformes (até *800* $^{\circ}$C). As equações codificadas segundo o MRD mostram-se incapazes de estimar adequadamente a resistência última de colunas sob falha distorcional, em condições de incêndio. Para simular a dependência/relação das propriedades do aço com o efeito da temperatura, é aplicado o modelo prescrito na Parte 1.2 do Eurocode 3 (EC3-1.2) para aço formado a frio. As cargas últimas obtidas são usadas para avaliar como essa dependência do modelo constitutivo do aço com a temperatura influencia na qualidade das estimativas segundo as curvas de resistência distorcional do atual MRD. Finalmente, são desenvolvidas curvas modificadas para colunas fixadas e apoiadas, apresentando uma melhora significativa na performance do MRD quanto à previsão da resistência última de peças sob falha distorcional e temperaturas elevadas.

Abstract of Thesis presented to COPPE/UFRJ as a partial fulfillment of the requirements for the degree of Doctor of Science (D.Sc.)

DSM-BASED PREDICTION OF DISTORTIONAL FAILURE LOADS OF COLD-FORMED STEEL COLUMNS AT ELEVATED TEMPERATURES

Fernanda Cristina Moreira da Silva Costa

September/2019

Advisors: Alexandre Landesmann
                 Dinar Reis Zamith Camotim

Department: Civil Engineering

This work is dedicated to investigate the structural behavior, strength and Direct Strength Method (DSM) design of cold-formed steel columns failing in distortional modes at elevated temperatures. The numerical results, obtained by means of ANSYS shell finite element analyses (SFEA), concern columns with (*i*) two end support conditions (fixed and pinned end supports), (*ii*) lipped channel cross-section shape with different dimensions (b_w/b_f equal ~ *0.7*, *1.0* and *1.4*), (*iii*) several room temperature yield stresses (distortional slenderness range up to ~ *3.5*), (*iv*) critical-mode (distortional) initial geometrical imperfections with small amplitudes, and (*v*) subjected to eight uniform temperatures (up to *800* $^{\circ}$C). It is shown that the currently codified DSM distortional design equations are unable to predict adequately failure loads under fire conditions. The temperature dependence of the steel material properties is simulated using the model prescribed in part 1.2 of Eurocode 3 (EC3-1.2) for cold-formed steel. The column failure load data obtained are used to appraise how the quality of the predictions provided by the existing DSM distortional strength curves is influenced by the temperature-dependent steel constitutive model. Finally, modified curves are developed for fixed and pinned end members, exhibiting a significant improvement of the DSM distortional design in estimating the ultimate strength of the CFS columns submitted to elevated temperatures.

INDEX

List of Figures

Symbols

Capital roman letters (abbreviations)

CFS   cold-formed steel

HRS   hot-rolled steel

DSM   Direct Strength Method

GBT   Generalized Beam Theory

EWM   Effective Width Method

ESM   Effective Section Method

LMM   Lee, Mahendran and Makelainen [12]

RM   Ranawaka and Mahendran [14]

WJ   Wei and Jihong [16]

LSB   Landesmann, Silva and Batista [15]

C   lipped channel cross-section column

F   fixed end support conditions

P   pinned end support conditions

FEA   Finite Element Analyses

Italic roman letters

b_w web width

b_f flange width

lip lip width

t thickness

T temperature (ºC)

E_{20} Young's modulus at room temperature (*20* ºC)

E_T Young's modulus at temperature T

k_y yield stress reduction factor for CFS

k_E Young's modulus reduction factor

k_p reduction factor for proportional limit

$k_{p0.2}$ yield stress reduction factor for CFS

L length

L_D length associated with the critical distortional buckling

A	cross-section area
P	axial load
$P_{y.20}$	squash load at room temperature (related to the yield stress)
$P_{y.T}$	squash load at temperature T (related to the yield stress)
$P_{u.20}$	ultimate/failure load at room temperature
$P_{u.T}$	ultimate/failure load at temperature T
$P_{cr.D}$	elastic critical (distortional) buckling load
$P_{cr.D.20}$	critical distortional buckling load at room temperature
$P_{L.20}$	lowest local buckling load at room temperature
$P_{G.20}$	lowest global buckling load at room temperature
$P_{cr.D.T}$	critical distortional buckling load at temperature T
$P_{n.D.20}$	nominal ultimate load at room temperature (for columns failing in distortional modes)
$P_{n.D.20(P)}$	nominal ultimate load at room temperature (for P columns failing in distortional modes)
$P_{n.D.T}$	nominal ultimate load at temperature T (for columns failing in distortional modes)
$P_{n.D.T(P)}$	nominal ultimate load at temperature T (for P columns failing in distortional modes)
$P_{n.D.T}^{P}$	modified/proposed nominal ultimate load for P columns
$P_{n.D.T}^{F}$	modified/proposed nominal ultimate load for F columns

Greek letters

β	coefficient/parameter of Ramberg and Osgood equation
η_T	coefficient/parameter, for temperature T, of Ramberg and Osgood equation
$\varepsilon_{y.T}$	yield strain at temperature T
$\varepsilon_{u.T}$	ultimate strain at temperature T
$\varepsilon_{p.T}$	strain corresponding to the proportional limit at temperature T
$\lambda_{D.20}$	distortional slenderness at room temperature
$\lambda_{D.T}$	distortional slenderness at temperature T
δ	imperfection (related to transversal deflection)
$\sigma_{y.20}$	yield stress at room temperature ($20\ ^oC$)
$\sigma_{v.M}$	von Mises stress
$\sigma_{y.T}$	yield stress at temperature T
σ_T	stress at temperature T
$\sigma_{p.T}$	stress corresponding to the proportional limit at temperature T
η	transition value associated to modified DSM curves for P columns

1 Introduction

In recent years, the technical-scientific advances in the steel construction industry have prompted the search for more flexible and economical design solutions. These include fabrication versatility and low production costs. In order to increase productivity and attend the high demand for new constructions, more efficient structure systems have been widely required [1]. In this context, the use of cold-formed steel (CFS) structures has grown steadily, due to their novel cross-section shapes that present higher strength-to-weight ratios and, thus, are structurally more efficient. The current extensive use in low rise residential, industrial and commercial buildings and also in high storage structures shows that CFS structures became extremely popular in different areas of civil construction, as exemplified by Figures 1.1 (a)-(b). The knowledge about the structural behavior of CFS members at room temperature has advanced considerably in the last few years and, moreover, such advances have been incorporated in design specifications at a fairly rapid pace.

(a)   (b)

Figure 1.1: Examples of CFS structural systems: (a) residence in light steel framing system [2] and, (b) storage structure [3].

Linked to the above trend, the need arises for a more specific study on the instability phenomenon that particularly affects the behavior of this type of structures,

due to the high strength of metals. Such property inevitably leads to the use of very slender structures, which makes light gauge CFS members being susceptible to various buckling modes and, consequently, to collapse by instability. Furthermore, when it comes to concern these structures subjected to fire conditions, there is an insufficient amount of research works carried out in this field. In addition to the fact that CFS members easily fail under buckling modes displaying large deflections, they present even more complex behavior at elevated temperatures.

Since it is well known that many CFS members are prone to distortional failure, the current design specifications include provisions dealing with this collapse mode. In particular, the Direct Strength Method (DSM - *e.g.* SCHAFER [4]), which has been incorporated into the previous and current versions of the North-American [5], Australian/New Zealand [6] and Brazilian [7] specifications for CFS structures, includes specific provisions (strength curves) for the design of columns and beams against distortional failure - their application requires only knowing the distortional buckling load/moment and the corresponding cross-section capacity. Nevertheless, such curves were developed and validated for CFS members at room temperature and it is still unknown whether they can also be adopted to estimate the ultimate strength of members under elevated temperatures, which alter considerably the steel constitutive model, namely its Young's modulus, yield strength and non-linearity.

1.1 Historic

The use of light steel structures in building construction began in the United States and England around 1850, but it was still limited to small residential constructions. During this period, some houses were built with steel roof structures, among other elements made also in steel, and most of these components were executed in CFS. During and after Second World War, the steel industry began to develop on a larger scale, enabling the improvement in the manufacturing processes of CFS. In 1933, at the Chicago World's Fair, a prototype of light steel framing residence was featured, as illustrated in Figure 1.2, which used steel structures replacing the wooden structures, very common in the construction industry up to that time. In this way, in 1940, about *2500* houses were built in CFS, including furniture [8].

Figure 1.2: Prototype of a Light Steel Framing residence at the Chicago World's Fair, in 1933 [8].

Although there were standards for the design of hot-rolled steel (HRS) structures since the mid-1930s, until this time, there was no normative procedure for the design of CFS structures. At this scenario, the American Iron and Steel Institute (AISI) initiated a specific study for light steel structural elements. Thus, in 1946, the first edition of the AISI, Specification for the Design of Light Gage Steel Structural Members, was published. Later, with the advance of new studies in this area, other versions of the AISI standard have been published. Nowadays, the most recent one is named as North American Specification for the Design of Cold-Formed Steel Structural Members [5].

In 1946, with the disastrous fire at the *Winecoff Hotel*, in Atlanta, recorded in Figure 1.3, that killed *119* people, and with the increased use of CFS in civil construction, there was a strong interest in developing and studying structures submitted to fire conditions [8]. When dealing with fire safety, the main objectives are to minimize life risk and reduce patrimonial loss [9]. In order to consider a relatively safe structure in an exceptional fire condition, it must be able to resist loads under elevated temperatures as well as to prevent its collapse. Accordingly, there may be localized failures of structural members, but nothing that leads to a global collapse. In addition, after the fire occurrence, it is essential to carry out an inspection to evaluate the possible reuse of the building or the need for a structural reinforcement.

Figure 1.3: Fire at the *Winecoff Hotel*, in Atlanta, in 1946 [10].

In the 1960's, CFS structures started to have new and different applications, such as walls surrounding stair towers and elevator shafts of buildings, dispensing the need of scaffolding. Since then, the use of CFS in the construction of industrial, residential and commercial buildings has grown steadily, as shown in the examples presented in Figures 1.4 (a)-(b). Following this trend, investigating and analyzing the strength of CFS structures subjected to fire action gain a great importance for the execution of a safe and economical project.

| (a) | (b) |

Figure 1.4: CFS structures: (a) buildings and (b) structural systems [11].

1.2   Motivation

Given the strong trend for the increasing use of CFS members in civil construction, the need for further study conducted to analyze the resistance of these structures under fire conditions becomes very relevant. In addition, when it comes to the importance of providing a safe design, the investigation of the mechanical properties and the behavior of CFS structures is also essential, once experimental results accuse a significant loss of strength and stiffness for these structures.

In the last decades, some researchers [12]-[16] have performed several experimental tests with samples of CFS to evaluate the behavior of this type of steel at high temperatures. The variation of the constitutive relations (stress-strain-temperature curves) obtained for different uniform temperatures was used to define the mechanical properties of CFS. Besides the corresponding reduction factors indicate a clear distinction from the HRS ones, there are also significant differences between such values concerning distinct CFS models.

In parallel, related studies have been expanded and a series of experimental and numerical analyses based on distortional buckling resistance of CFS columns under elevated temperatures have been reported [4], [13], [17]-[23]. Generally, the works present a comparison between the codified Direct Strength Method (DSM) distortional design curves and the results obtained by the authors mentioned. Besides indicating some divergence, the failure load data obtained are still insufficient to evaluate the quality and safety of the existing DSM curves, when it comes to fire conditions.

Recently, facing this lack of CFS ultimate strength analyses, a numerical investigation on distortional buckling resistance at elevated temperatures was performed [17], providing strong evidence that the current DSM curves overestimate the failure loads in the low-to-moderate slenderness range. Moreover, the study detected important evidences that the ultimate load capacity was influenced by the temperature-dependent material model considered (namely stress-strain curve shape), particularly for stocky columns. Amid this scenario, it is also worth pointing that the application of some available design methods requires the extensive use of costly fireproofing materials, aimed at protecting the steel structures from an excessive heat increase due to fire hazards. This demand leads quite often to overly conservative and uneconomical structural designs.

Thus, in this context, the above findings provided the motivation for the present work, which continues the aforementioned numerical investigation on distortional

buckling resistance of CFS columns submitted to elevated temperatures. The expressive need to develop improved distortional design curves, which are able to incorporate the influence of the steel constitutive model (firstly, concerning the option of EC3-1.2 [24] model), leads to expand the numerical analyses with a view to reaching more accurate DSM distortional strength curves. Furthermore, the previously mentioned studies indicate the promising use/consideration of the different reduction factors associated to each stress-strain-temperature relationship.

1.3 Objective

In view of the above, the present work aims to investigate how the temperature dependence of CFS constitutive model influences the quality/safety of lipped channel columns' ultimate load estimates, provided by the current DSM distortional design curves. The failure load data obtained, concerning columns subjected to various uniform temperature distributions and taking into account the EC3-1.2 [24] stress-strain curve for CFS, are used (*i*) to assess the performance of the available DSM distortional strength curves and quantify the accuracy of the corresponding predictions and (*ii*) to appraise how such quality is influenced by the temperature-dependent steel constitutive model.

As part of the main objective, the following results are achieved: (*i*) evaluation of elastic-plastic post-buckling and ultimate strength, (*ii*) comparison and assessment of the results obtained from ANSYS' analyses and the DSM predictions. Finally, the findings about the applicability of the method are clarified, as well as the important need for its improvement. Therefore, some adjustments applied to the DSM distortional strength curves are proposed, reaching more efficient estimates for cases under elevated temperatures.

1.4 Scope and organization of the thesis

Initially, in Chapter 2, a bibliography review is presented summarizing previous works associated to buckling/post-buckling behavior and ultimate strength of CFS members, concerning conditions of room and elevated temperatures. The concept of structural stability is addressed just to begin all the theoretical context, that involves some relevant topics about equilibrium configuration. In the sequence, the main studies reported in the literature including numerical and experimental analyses about buckling and post-buckling behavior are presented, considering that there are few works in this

area dealing with high temperatures. The available design method intended to estimate the column failure loads submitted to distortional post-buckling behavior are described. In addition, this section presents and discusses about the state of art of temperature dependence, taking into account the available constitutive models prescribed in EC3-1.2 [24] and developed by some researchers, for CFS structures under elevated temperatures.

Next, Chapter 3 defines the column geometry selection procedure used in this work. At this point, some important/basic considerations are aligned: (*i*) column support conditions and lengths, (*ii*) cross-section shape and dimensions, (*iii*) distortional buckling mode specifications and (*iv*) the variation of elastic critical buckling loads with the length for high temperatures.

Chapter 4 starts presenting the mesh convergence tests performed to obtain the shell finite element dimensions that ensure a good computational efficiency and functionality for the analyses. The finite element analysis method is explicitly described, as well as the model geometry specifications, namely initial geometrical imperfections and application of support conditions. The final important topic addressed is the CFS material behavior adopted in the numerical analyses, which involves the EC3-1.2 [24] constitutive model for elevated temperatures. The corresponding stress-strain-temperature relationship is thoroughly clarified and graphically displayed.

Then, Chapter 5 covers all the distortional response of the selected lipped channel columns, describing the elastic-plastic post-buckling behavior at both room and elevated temperatures and also highlighting the corresponding remarkable observations. Moreover, this section approaches the ultimate strengths obtained in the shell finite element numerical analyses (SHELL181 − ANSYS nomenclature), presents the plots of the failure loads ratios according to each temperature considered (*T=20/100-200-300-400-500-600-700-800 ºC*) and details the comparison of the results.

In the sequence, Chapter 6 comprises the DSM distortional design and their main considerations for predicting the columns' ultimate strengths, when submitted to room/moderate and elevated temperatures. Aiming at developing more accurate and safe DSM distortional design curves (for pinned and fixed end columns), this chapter shows the existing formulation and elaborates new and modified curves, that achieve a noticeably improved performance. Additionally, statistical indicators are plotted graphically to clearly demonstrate the evolution of the method, taking into account the results obtained.

Finally, the main conclusions about the findings displayed in this thesis and some suggestions for future works aiming to continue the research are presented in Chapter 7.

2 Bibliography Review

The behavior of steel structures exposed to fire involves the reduction of strength and stiffness of the steel, while their temperature increases. Depending on the applied loads and the support conditions, a fire case may lead to possible deformation and failure. In addition, the steel also has a higher thermal conductivity than most other materials [25]. As already introduced, the deterioration of the mechanical properties is one of the main factors that affect the performance of steel structures at elevated temperatures.

The research activity devoted to CFS members under fire conditions is relatively recent. The small number of available publications on the subject attests that this concentration area is still in early development. Furthermore, only a small fraction of these studies directs and correlates the elevated temperatures conditions to an instability phenomenon that often governs the behavior and strength of CFS structures, like the occurrence of local, distortional or global (flexural and torsional) buckling. It is also worth noting that such existing researches do not take into account the particular case of stocky columns.

In this context, the literature survey begins by presenting the stability and equilibrium concepts and buckling modes, focusing on the main previous works and standard methods concerning specifically distortional buckling associated to fire conditions, post-buckling behavior and ultimate strength. In the sequence, the literature review presents the available temperature dependence of the mechanical properties of CFS members reported by some researchers and prescribed by EC3-1.2 [24], essential for their design under fire conditions.

2.1 Structural stability and equilibrium paths

Structural design of CFS members must attempt to the stability requirements, as well as to strength and safety requirements. It means that CFS structures can collapse either by insufficient material strength or structural instability. The former requires the use of equilibrium equations concerning the undeformed configuration of the structure, while the latter employs equilibrium equations according to the deformed configuration. In this context, it is important to present the concepts of stable or unstable equilibrium.

Considering a structure submitted to external forces and presenting a specific equilibrium configuration, the set stability is assessed through the structural behavior obtained after a slight perturbation caused by an external load. The equilibrium is defined as stable in case of the structure returns to its original position after the end of the perturbation and unstable in case of the structure does not return to its origin position [26]. Concerning the stability concept for column structures under compression, it is worth mentioning the classic problem called by "*Euler column*", which consists of the following conditions: (*i*) an elastic and perfectly straight column with (*ii*) length *L*, (*iii*) simple supported ends and (*iv*) submitted to an axial load *P*, as illustrated in Figure 2.1 (a).

The corresponding equilibrium path is presented in Figure 2.1 (b) (axial load *P* versus lateral displacement *δ* at mid-length). In this figure, the intersection point of the "fundamental path" (region where *δ=0*) and the "post-buckling path" (region where *δ≠0*) is designed as bifurcation load or *Euler critical load* (*P_E*), which is defined in Eq. 2.1. At this critical load point, there is a bifurcation in the equilibrium configuration – the column can remain straight or present some displacement, thus defining transition from stable (solid line) to unstable equilibrium (dashed line). Then, as the column structure is still subjected to the applied axial load, it leads to a deformed configuration corresponding to the post-buckling path (stable equilibrium). These figures represent a typical example of geometric nonlinearity behavior. The deflected shape is given by Eq. 2.2.
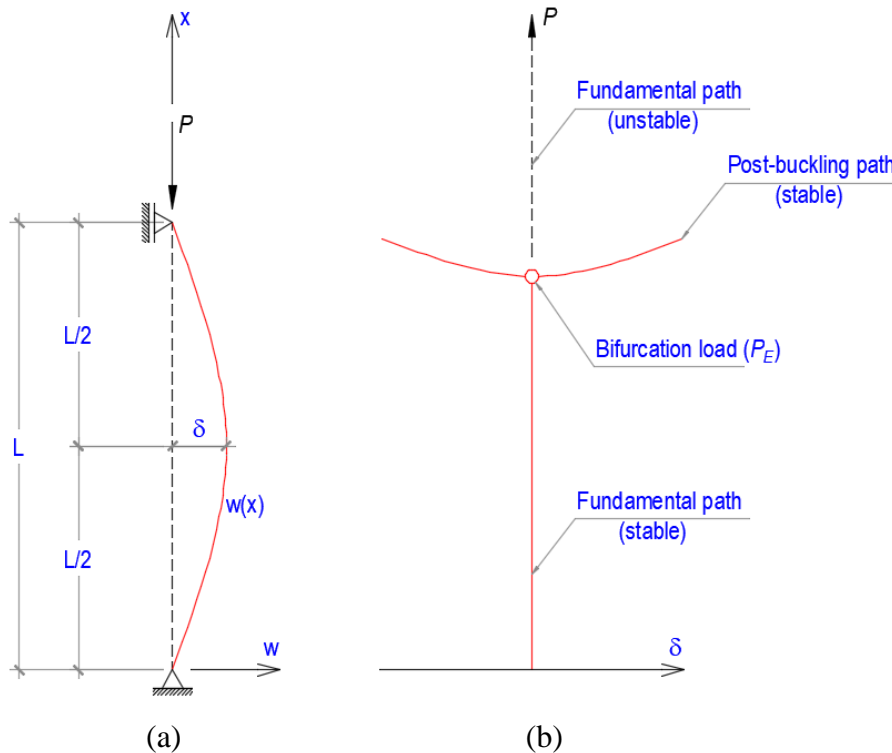
Figure 2.1: *Euler column*: (a) geometry and load and (b) equilibrium path [26].

$$P_E = \frac{\pi^2 EI}{L^2} \qquad \text{(Eq. 2.1)}$$

$$w(x) = \delta \cdot \sin\left(\frac{\pi x}{L}\right) \qquad \text{(Eq. 2.2)}$$

As observed in previous figures, the structural instability is defined from the point where the equilibrium bifurcation occurs. Therefore, this phenomenon can only be detected through numerical analyses capable of predicting (considering or even anticipating) the geometric nonlinearity behavior, namely the occurrence of these "displacements". This means employing equilibrium equations that concern the column deformed configuration and, thus, providing to cover several buckling and post-buckling analyses' cases.

At this stage, it is possible to introduce the definition of initial geometrical imperfections, used throughout this work. Figure 2.2 (a) shows the initial deformed configuration (with amplitude equal to δ_0) of a column subjected to an axial load. When this load reaches the yield point, the material enters the plastic zone and starts to deviate from the original elastic path, indicating loss of stiffness due to plasticity effects [26], as illustrated in Figure 2.2 (b). This zone is called elastic-plastic path and δ is the additional amplitude imperfection due to the applied load P. The plasticity effects intensify as the compression load and displacements increase, leading to the maximum force supported by the column (collapse), *i.e.*, the ultimate load P_u.
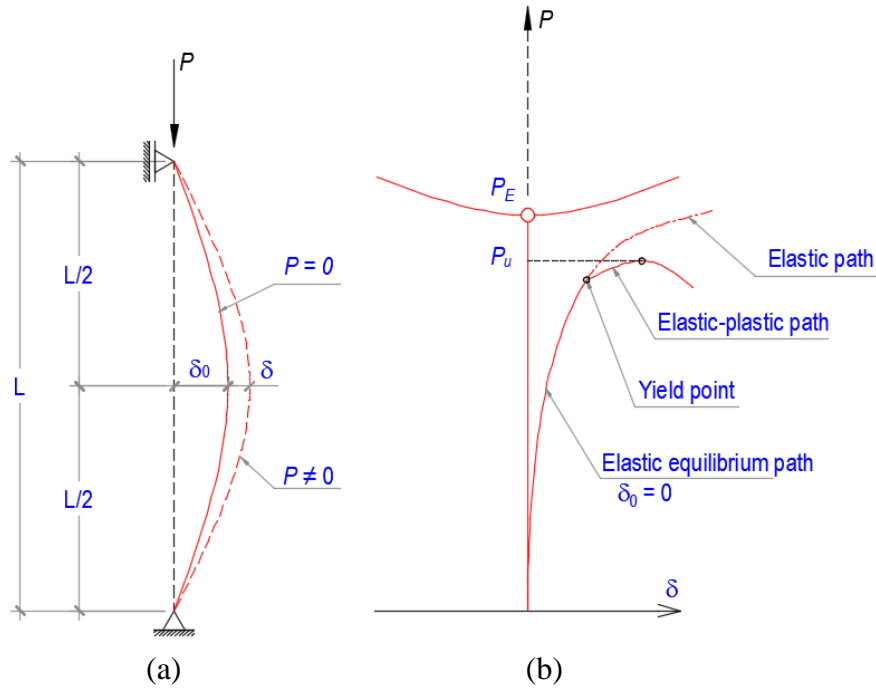
Figure 2.2: Column elastic-plastic behavior: (a) geometry and initial imperfection and (b) equilibrium path [26].

2.2 Buckling, post-buckling and ultimate strength

Buckling mode consists of the deformed configuration that the structure develops during the application of a progressive load, as it approaches the critical load. In practical terms, the buckling mode corresponds to the stage, for example, when a column structure under axial compression load loses its original shape and "buckles".

2.2.1 Buckling

According to the definition already introduced, buckling is the loss of the original shape of a member as a result of elastic or inelastic strain [27]. This change into a deformed configuration is classified in local, distortional or global (flexural or flexural-torsional) buckling, specifically for CFS structures. Depending on the structure's geometrical features, any of these buckling modes can be associated to the critical load.

Local buckling involves each plate (wall element) bending lonely without transverse deformation and the line junctions between elements remain straight. Distortional buckling involves changing in cross-sectional shape excluding local buckling [28]. In addition, it presents rotation at the web-flange junction in typical members [29]. Global buckling holds two buckling shapes: (*i*) flexural buckling results from a bending in compression members without changing the cross-sectional shape and (*ii*) flexural-torsional buckling (or torsional) involves bend and twist simultaneously without changing the cross-sectional shape as well. Figures 2.3 (a)-(b) illustrates the effects described earlier, aiming to better exemplify each of these buckling shapes.

(a)   (b)
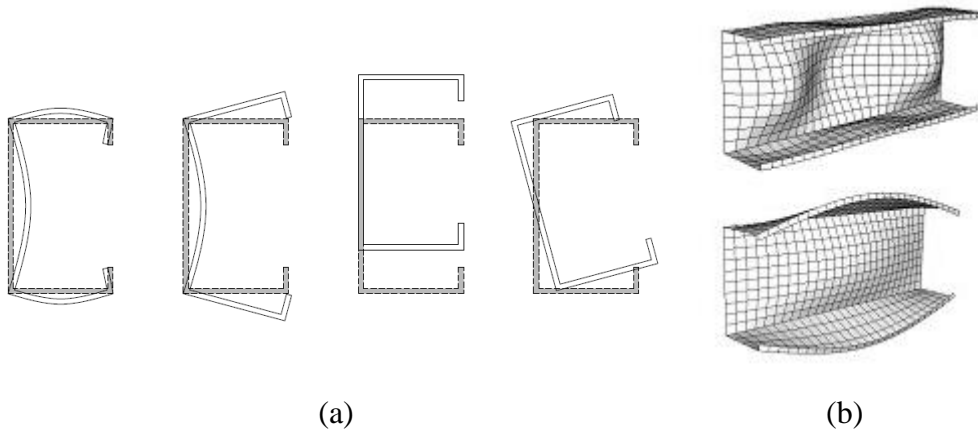
Figure 2.3: (a) Cross-section in-plane buckling shapes – local, distortional, flexural and torsional buckling, respectively, and (b) two isometric views of a shell finite element model under local and distortional buckling, concerning lipped channel column geometry.

11

The software GBTUL [30][31], based on the Generalized Beam Theory (GBT), works as an effective tool to perform elastic buckling analyses concerning isotropic material, requiring some mechanical properties and cross-section dimensions of the structure element as input data. This program provides, among other results, (*i*) in-plane deformation of buckling modes, (*ii*) signature curve and (*iii*) participation of each buckling mode related earlier. The cross-section analysis results in a set of deformation modes (as defined in Eq. 2.3), which represents the possible cross-section deformed configurations to be considered [31]. The relation established in this equation shows that the quantity of deformation modes (N_d) depends on the number of walls (*n*) and the number of intermediate nodes (*m*).

Aiming to illustrate this topic, Figure 2.4 (a) indicates natural and intermediate nodes as red and yellow marks, respectively, and the endpoints (both natural and intermediate nodes) as green marks. Figure 2.4 (b) shows the first *13* in-plane deformation modes for an arbitrary open and unbranched lipped channel section: (*i*) the first *4* are the rigid-body global modes – axial shortening (mode 1), major and minor axis bending (modes 2 and 3) and torsion (mode 4), (*ii*) modes 5 and 6 are distortional and (*iii*) the remaining ones are local-plate modes, which involve exclusively wall bending (note that the total number of local modes (*7*) is equal to the number of intermediate modes considered, *m*).

$$N_d = n + 1 + m \qquad \text{(Eq. 2.3)}$$

(a)   (b)
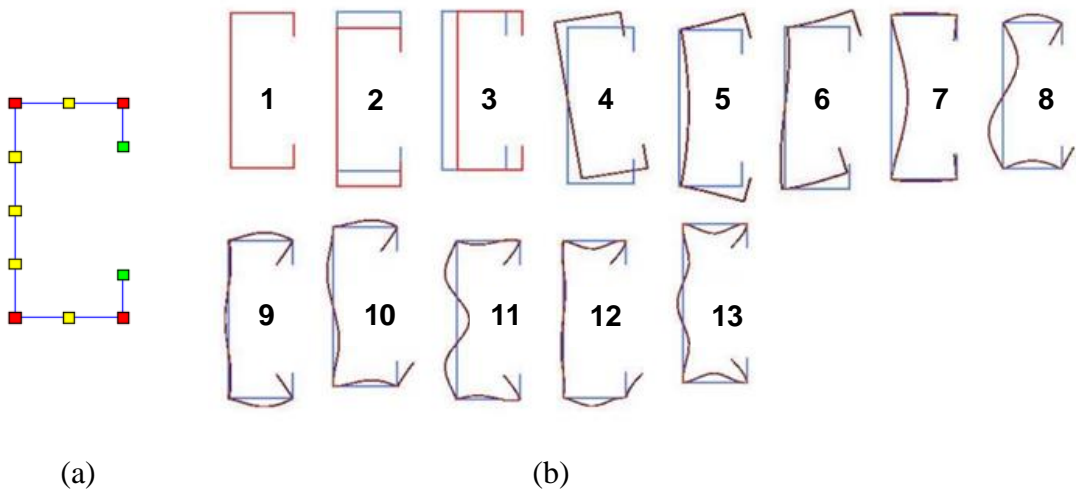
Figure 2.4: Cross-sections analyses in GBTUL, concerning a lipped channel column type (a) nodal discretization and (b) in-plane deformed configuration [31].

Depending on the geometry (cross-section dimensions and length) and support conditions, any of these buckling modes may be the critical one. It is also worth mentioning that only sections with at least *4* walls present distortional modes.

The signature curve, previously cited, is another result that GBTUL buckling analyses provide. This type of graphic relates the critical load versus member length and presents a characteristic tracing depending on the structure type/shape. For example, concerning pinned end columns, the minimum point at the signature curve corresponds to critical loads indicating local or distortional buckling. SCHAFER [32] presented a signature curve for lipped channel column and pointed out the buckling mode/shape for each critical load, as shown in Figure 2.5.
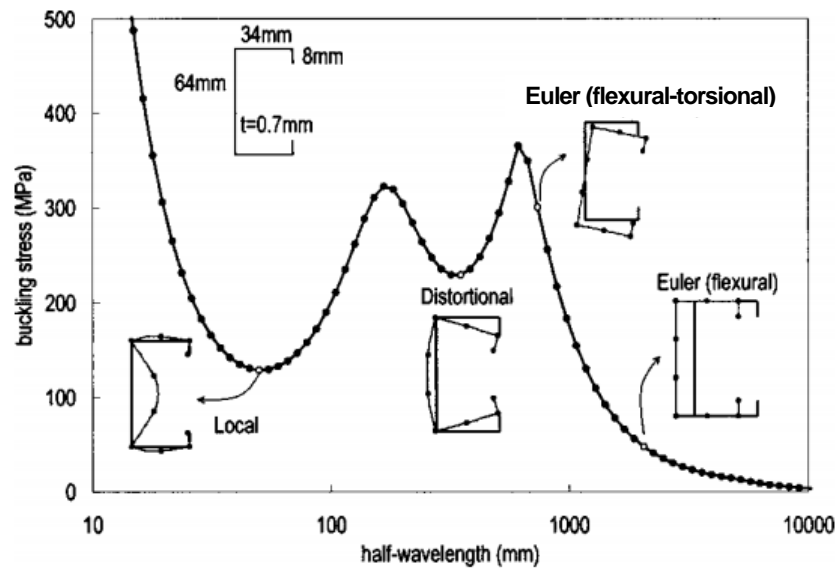
Figure 2.5: Example of signature curve for a pinned end lipped channel column [32].

In case of fixed end support conditions, there is not a clear minimum point at the signature curve that leads to determine the exact buckling mode, as it appears for pinned end columns, thus it is necessary to evaluate the modal participations. In fact, a real buckling shape consists of some buckling modes combination. It means that even if a column presents distortional buckling mode, it might have some participation of others buckling modes. Hence, to classify the buckling mode in local, distortional or global, the percentage of each buckling mode participation must be considered. Just for example, Figure 2.6 shows a case of GBT modal decomposition of a lipped channel subjected to distortional buckling.

13
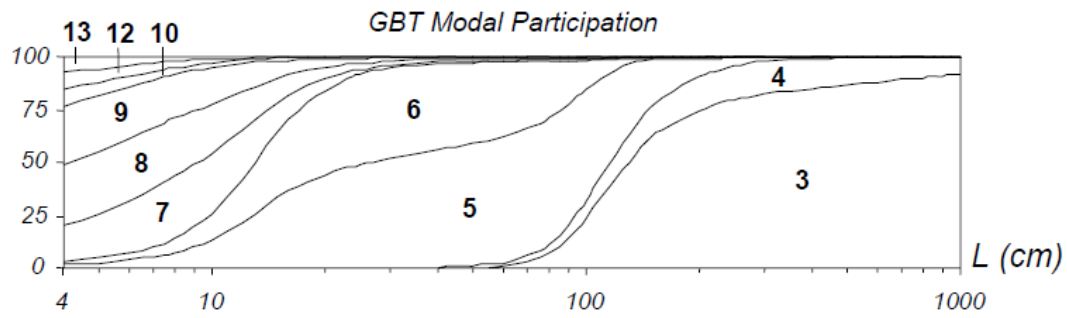
Figure 2.6: Example of GBT modal participation in case of distortional buckling mode prevailing for members with small-to-intermediate lengths (*10<L<90*) [33].

According to SCHAFER [29], the distortional mode is predominant in lipped channel columns when the flange width approaches the web height and the critical distortional load decreases while the critical local load increases. Thus, columns with "square shape" cross-sections tend to present larger distortional modal participations, whereas cross-sections with smaller flange widths (less than *1/6* of the web length) are usually controlled by local buckling mode [29].

Generally, one buckling mode is predominant, however, depending on the member features, some modal interactions can occur and more than one buckling mode can be relevant for the column buckling behavior. Although ANSYS proves to be effective when it comes to buckling and post-buckling analyses and also very accurate for critical load prediction (results obtained through GBTUL and ANSYS analyses are very similar), this software is not able to provide modal participations.

2.2.2 Post-buckling and ultimate strength

The issue already introduced about column structures, that start to buckle as they are subjected to axial compression load approaching the critical load value, is recalled in this item. Reported works demonstrate that the column's stiffness can either increase or decrease. Figures 2.7 (a)-(b) show elastic equilibrium paths where solid lines illustrate the behavior of perfect members and dashed lines indicate the theoretical behavior for the same member with some degree of initial imperfection (δ_0). If the applied load increases, after the beginning of buckling, with rising deformation behavior, as shown in Figure 2.7 (a), it is stated that the structure has a stable post-buckling. Differently, if the load decreases without reaching the critical load, as indicated in Figure 2.7 (b), it is noted that the column has an unstable post-buckling curve.

14
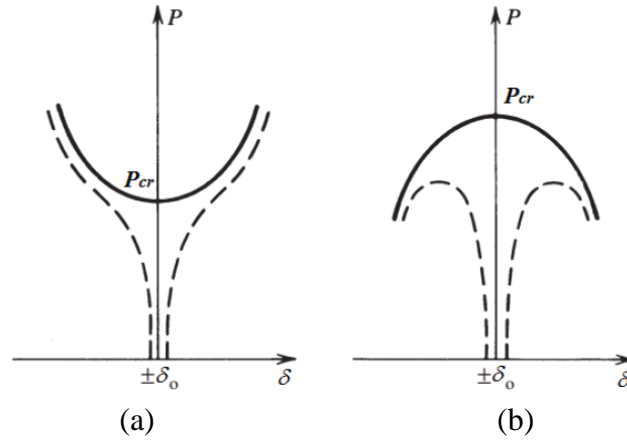
Figure 2.7: Elastic post-buckling equilibrium paths for columns with and without initial imperfection: (a) stable and (b) unstable post-buckling [27].

Similarly to this effect, SILVESTRE and CAMOTIM [34] developed numerical analyses considering both stiffened and plain lipped channel columns under compression load and concluded that the stiffened ones associated with an outward lip motion and the plain ones associated with an inward lip motion proved to be stiffer than their counterparts (more expressively in the plain columns associated with an outward lip motion cases), as plotted in the elastic distortional post-buckling equilibrium paths of Figure 2.8.
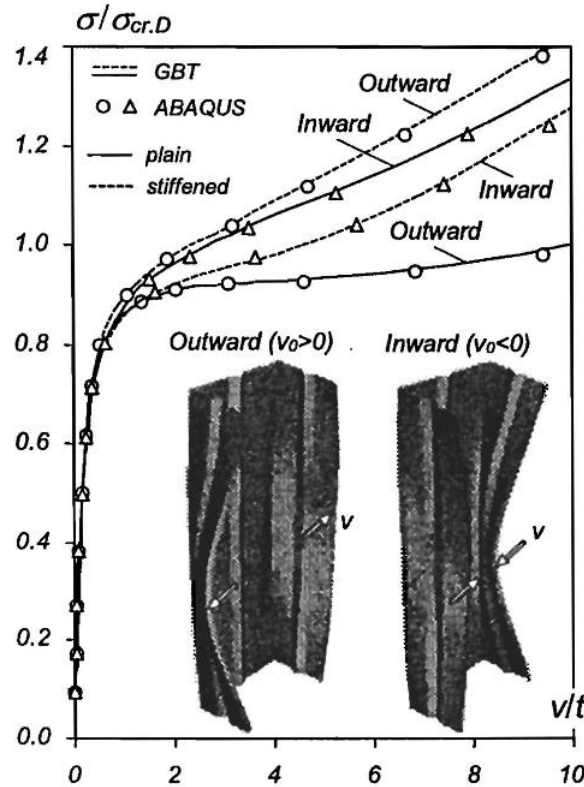
Figure 2.8: Distortional post-buckling equilibrium paths concerning both plain and stiffened lipped channel columns, associated with inward and outward lip motions [34].

15

In the same context, numerical analyses about the influence of the cross-section geometry and end support conditions on the post-buckling behavior of columns failing in distortional modes were conducted [35]. The columns analyzed exhibited fixed, pinned-fixed, pinned and fixed-free end support conditions and displayed lipped channel, hat-section, zed-section and rack-section. Among other results, the authors stated that the post-buckling strength decreases in the following sequence of column end support conditions: fixed, pinned-fixed, pinned and fixed-free. In addition, even though they expected rack-section to be always stiffer (they have more lips than the other three cross-section types), the obtained results showed that the extra stiffeners may have added distortional vulnerability to the column.

The curves presented in Figure 2.8 are examples of elastic equilibrium paths, so the ultimate load responsible for the collapse occurrence is not indicated. To determine the failure load of a real member, initial imperfections must be considered, in order to continue plotting the nonlinear load-deflection curve. The corresponding material and geometrical nonlinearities must be taken into account as well. In most cases, the collapse of steel structure occurs due to an interaction between instability and plasticity phenomenon, namely instability in elastic-plastic stage [26]. Hence, there is a need to assess the elastic-plastic post-buckling behavior.

Given a column under compression that loses the capacity to support increasing load and starts to present increasing deflection, it means that the ultimate load was already reached. This load is the top point of the elastic-plastic post-buckling equilibrium path. Figures 2.9 (a)-(b) show the curves for the applied load normalized ($P/P_{cr.D}$) against $|\delta|/t$, as an example of elastic-plastic equilibrium paths of both fixed and pinned columns, respectively. After the maximum point (white circles), the column is no more able to support increasing load. Instead, the load decreases while the deflection increases. This peak indicates the highest value of ratio $P/P_{cr.D}$ and, in this case, P is the ultimate load (P_u). As the $P_{cr.D}$ is easily obtained from the elastic buckling analysis, the evaluation of the ultimate load is straightforward. Naturally, it can be noted that ultimate strength is directly related to the yield stress (σ_y), which means that as σ_y increases, P_u increases as well.
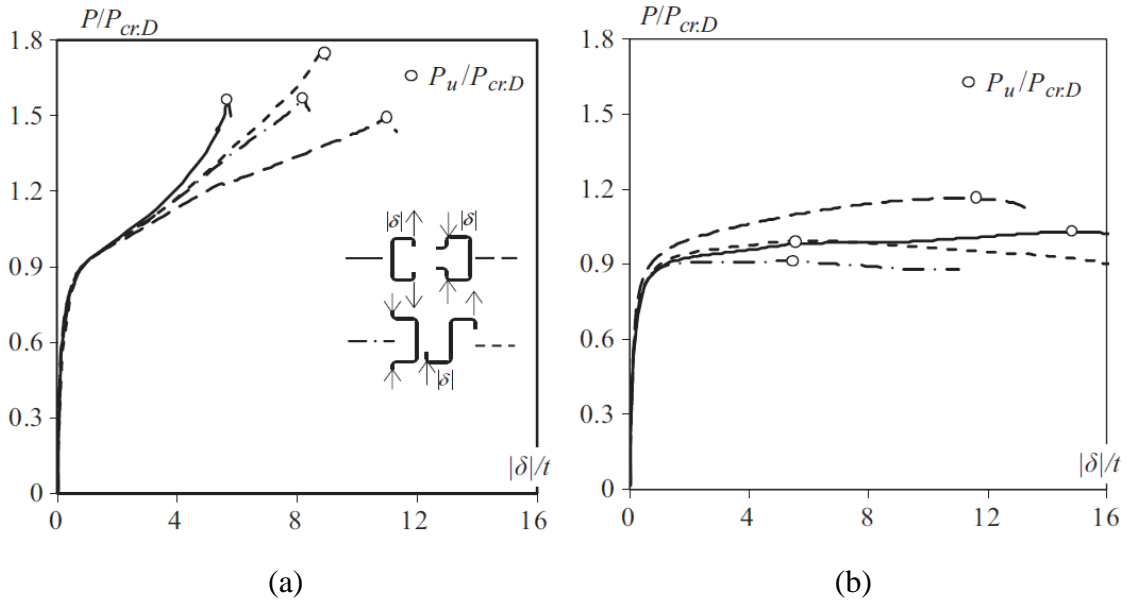
Figure 2.9: Elastic-plastic distortional equilibrium paths for columns with different cross-section shapes concerning (a) fixed and (b) pinned end support conditions [35].

2.3 Design methods

The next items present the design methods for ultimate strength predictions of CFS members, with special attention to the Design Strength Method (DSM). Concerning the Brazilian specification [7], three design methods are presented: the Effective Width Method, the Effective Section Method and the Direct Strength Method (DSM).

2.3.1 Effective Width Method (EWM)

The Effective Width Method was widely used until the end of the 20th century for the design of CFS structures. This method considers that only part of each element contributes to the member strength. The original idea was proposed by *Von Karman* and adopted for CFS members by *Winter* at Cornell University [36]. Indeed, it is worth mentioning that the EWM (*i*) ignores the inter-element (*e.g.* region between flange-web) equilibrium and compatibility when determining the elastic buckling behavior, (*ii*) does not provide a good evaluation/consideration of the possible buckling modes, such as distortional buckling case, (*iii*) requires laborious interactions to determine even a basic member strength and (*iv*) provides a very complicated way to define the effective section, as attempts to optimize the section are made (when the cross-section geometry becomes

more complex, for example adding intermediate stiffeners, the calculation of effective width becomes more difficult as well) [4].

As already stated, the EWM is not appropriate to account distortional buckling; it was attested by AISI specification in the 1990's, proving to be non-conservative for cases of channel sections made of high-strength steel. Thus, there was a need for alternative design methods which consider properly distortional buckling [37].

2.3.2 Effective Section Method (ESM)

The Effective Section Method [38] is an extension of the Effective Area Method (EAM), which was originally proposed for CFS columns. It is possible to assert that the advantages of EAM are similar to the DSM ones: (*i*) the local plate buckling is taken by considering the complete cross-section behavior, unlike the EWM prescriptions that consider isolated plate elements, (*ii*) there are strength curves for columns, including local-global buckling interaction and (*iii*) rules for design were formulated like in DSM (see next section). The extension of the EAM principles for CFS beams enabled the proposition of rules and equations for CFS members' design, resulting in the ESM, that can replace the EWM [38]. In short, the ESM, included in the ABNT/NBR 14762 [7], considers an effective area evaluation instead of taking each cross-section elements separately, presenting itself as a simpler method than the EWM.

2.3.3 Direct Strength Method (DSM)

The Direct Strength Method originated from researches carried out by HANCOCK *et al.* [37] and then developed by SCHAFER and PEKÖZ [39], aiming to avoid the complexity of the EWM and to determine the strength of CFS members more simply. It becomes possible since the DSM directly integrates the elastic buckling analysis, obtained through numerical solutions (indispensable use of software programs), into the process. Thereby, the DSM deals with a relatively easy formulation (more unified approach) to find the CFS structure failure load; it uses simple "Winter-type" equations that provide a "direct" estimate of the member ultimate strength. In addition, it enables to handle the wide variety of different shapes displayed for CFS structures, requiring only knowing the member yield stress and distortional buckling load.

Associated to the considerable advances in research works about CFS structural behavior, some current design specifications already included provisions dealing with the corresponding failure modes to which such members are usually susceptible. It is worth noting that the North-American (AISI [5]), Australian/New Zealand (AS/NZS [6]) and Brazilian (ABNT/NBR 14762 [7]) standards are the main ones that incorporated these proceedings, due to the efficiency achieved through this method. The existing codified DSM distortional design curve is described in Equation 2.4.

$$
P_{n.D.20} = \begin{cases} P_{y.20} & \text{for } \lambda_{D.20} \leq 0.561 \\ P_{y.20}\left[1 - 0.25\left(\dfrac{P_{cr.D.20}}{P_{y.20}}\right)^{0.6}\right]\left(\dfrac{P_{cr.D.20}}{P_{y.20}}\right)^{0.6} & \text{for } \lambda_{D.20} > 0.561 \end{cases},
\qquad \text{(Eq. 2.4)}
$$

where (*i*) $P_{cr.D.20}$ and $P_{y.20}$ are the column distortional critical buckling and yield/squash loads, respectively, and (*ii*) $\lambda_{D.20} = (P_{y.20}/P_{cr.D.20})^{0.5}$ is the column distortional slenderness.

Figure 2.10 presents the plots of the experimental results reported by SCHAFER [4] during the validation attempt of the DSM distortional (blue color) and local (red color) strength curves.
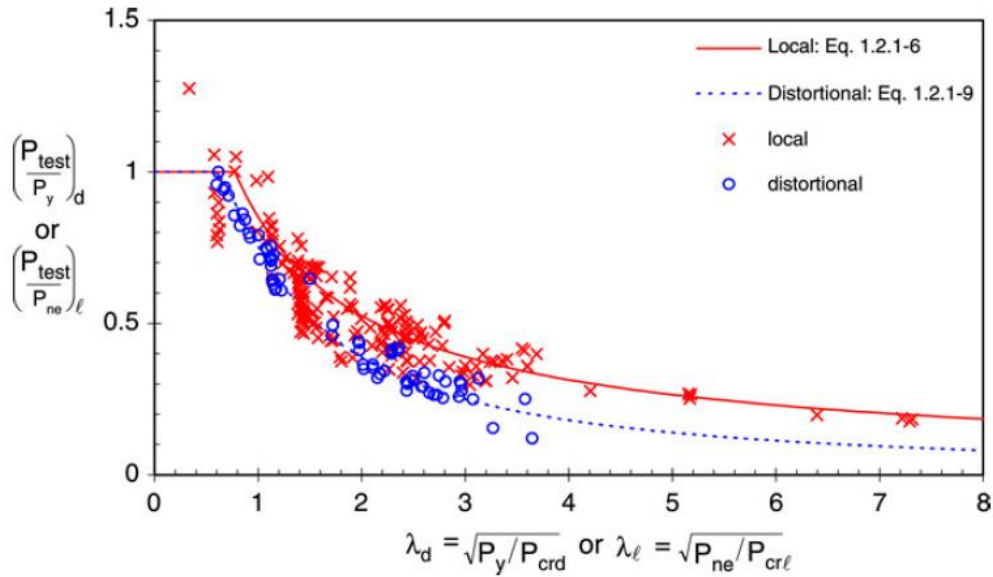
Figure 2.10: DSM design curves presented by SCHAFER [4].

However, such curves present a restricted applicability since they were developed and validated only for members at room temperature and it is still unknown whether they can also be adopted (with or without modifications) to estimate the ultimate strength of members under elevated temperatures, which alter considerably the steel constitutive model, namely its Young's modulus, yield strength and amount of non-linearity.

Furthermore, the DSM validation procedure [4] had a limited scope, because it involved columns with only fixed-end support conditions.

2.4 CFS constitutive models at elevated temperatures reported by researchers

The CFS constitutive model definition is fully associated with the mechanical properties, such as yield stress and Young's modulus. For example, it is worth mentioning the importance of the Young's modulus in the evaluation of the structural members' instability (determination of the critical buckling load and the flexural and axial compression stiffness). Besides that, the calculations involving material strength, such as flexural, axial and shear strength, depend directly on the material yield stress [40], indicating that the definition of these factors is essential for the study of CFS performance and design.

Therefore, the search for methodologies to ensure the fire safety design of CFS members must begin with a fairly accurate knowledge on the temperature dependence of the CFS thermal and mechanical properties, which is often very substantial. In addition, it is widely recognized that the reduction factors of mechanical properties applicable to HRS grades do not apply to the CFS ones. As stated by SIDEY and TEAGUE [41], there are some different metallurgical composition and molecular surface effects that make the strength reduction in CFS at elevated temperatures be about *10-20%* higher than that occurring in HRS. Furthermore, KANKANANGE and MAHENDRAN [42] found that CFS under elevated temperatures are likely to loose the additional strength acquired during the cold-working process at room temperature. In addition, the high section factor of CFS structures contributes to accelerate the degradation process of their resistance under fire conditions. Hence, to concern such differences, EC3-1.2 [24] treats CFS members similarly to slender thin-walled (*i.e.*, Class 4) hot-rolled and welded ones.

Researches conducted by LEE *et al.* [12], CHEN and YOUNG [43], RANAWAKA and MAHENDRAN [14], WEI and JIHONG [16] and LANDESMANN *et al.* [15] demonstrate that the deterioration of the steel mechanical properties (yield stress and elastic modulus) is more pronounced in case of CFS than in HRS. These authors performed large experimental programs based on CFS coupon tensile tests, concerning steady state method, to (*i*) assess the reduction of mechanical properties and (*ii*) propose constitutive relationships (stress-strain-temperature curves) based on the experimental results obtained.

It is important to emphasize the use of steady state test method to conduct the analyses in this work. Actually, there are two types of tensile test when it comes to CFS

experimental program: steady state and transient state tests. The first consists of heating a coupon sample up to a certain temperature. After reaching the pre-selected temperature and keeping it uniform/stable, the load is applied until the failure of the specimen. Differently, on the transient state method, the load is applied and kept uniform while temperature rises until failure. Indeed, the transient state is more representative of a real fire situation, because the temperatures increase over time and the load is usually stable. On the other hand, the steady state is more easily controlled in experimental tests and it provides the stress-strain curve directly. Moreover, in the transient state, the results lead to temperature curves varying in function of deformation and it is necessary to convert these results to obtain the usual stress-strain curve − more complex and imprecise methodology. Thus, against the above, only steady state tests from the reported researchers are adopted and considered in this work.

LEE *et al.* [12] performed an extensive experimental program involving *189* tensile coupon steady state tests with the following specifications: (*i*) *3* steel grades (nominal yield stress of *550*, *500* and *300* MPa), (*ii*) *4* nominal thicknesses (*0.4-0.6-1.0-1.2* mm), and (*iii*) *9* different uniform temperatures (*20-100-200-300-400-500-600-700-800* ºC). The authors studied the deterioration of mechanical properties for cold-formed steel under elevated temperatures to derive accurate empirical equations for the yield stress (k_y) and elastic modulus (k_E) reduction factors (see Table 2.1). The stress-strain-temperature curves proposed by the authors (*LMM* and, in the sequence, *RM*, *WJ* and *LSB*) are originally based on the RAMBERG and OSGOOD [44] equation for elevated temperatures as shown in Eq. 2.5:

$$\varepsilon_T = \frac{\sigma_T}{E_T} + \beta \left(\frac{\sigma_{y.T}}{E_T} \right) \left(\frac{\sigma_T}{\sigma_{y.T}} \right)^{\eta_T} \qquad \text{(Eq. 2.5)}$$

where σ_T and ε_T are the applied stress and ensuing strain at temperature *T*, the coefficients β and η_T determine the stress values in the plastic region. All the related parameters and their dependence with temperature *T* are listed in Table 2.1.

The experimental program executed by RANAWAKA and MAHENDRAN [14] to investigate the deterioration of mechanical properties of cold-formed steel members considered tensile coupons with (*i*) *3* nominal thicknesses (*0.6-0.8-0.95* mm), (*ii*) made of G550 and G250 steel grades and (*iii*) subjected to *8* uniform temperatures (*20/100-200-350-500-600-650-800* ºC). Similarly, a detailed experimental investigation was reported by WEI and JIHONG [16] comprising a series of steady and transient state tests

with *1* mm thickness tensile coupons made of G550 steel grade at different temperatures (up to *600* ºC). LANDESMANN *et al.* [15] also developed an experimental characterization of cold-formed steel at high temperatures and determined the reduction factors for the corresponding mechanical properties. The research included coupon tensile test specimens with *2.7* mm thickness, nominal yield stress of *345* MPa and different uniform temperatures (*20/100-200-300-400-500-600* ºC). All the corresponding parameters and analytical expressions developed are listed in Table 2.1.

Table 2.1: Parameters and analytical expressions proposed by some researchers
(*LMM* [12], *RM* [14], *WJ* [16] and *LSB* [15]).

k_y	LMM	$1.0065 - 0.0004T + 2 \times 10^{-6}T^2 - 10^{-8}T^3 + 7.9 \times 10^{-12}T^4$ for $20^oC \leq T \leq 800^oC$
	RM	$1.8476 \times 10^{-11}T^{3.98} - 1.91 \times 10^{-8}T^3 + 3.625 \times 10^{-6}T^{1.997} - 10^{-4}T + 0.99$ for $20^oC \leq T \leq 800^oC$
	WJ	$-4.551 \times 10^{-7}(T + 140)^2 + 1.103 \qquad$ for $0^oC \leq T \leq 300^oC$ $-2.297 \times 10^{-9}(T + 164.5)^3 + 1.156 \qquad$ for $300^oC < T \leq 525^oC$ $1.404 \times 10^4(T - 491)^{-3} + 4.58 \times 10^{-2} \qquad$ for $525^oC < T \leq 600^oC$
	LSB	$1.0 \qquad\qquad$ for $20^oC \leq T < 300^oC$ $2 \times 10^{-9}T^3 - 6 \times 10^{-6}T^2 + 0.0019T + 0.916 \qquad$ for $300^oC \leq T \leq 600^oC$
k_E	LMM	$1.0 \qquad\qquad$ for $20^oC \leq T \leq 100^oC$ $1 - 0.014(T - 100) \qquad$ for $100^oC < T \leq 500^oC$ $\dfrac{1 - T/1200}{0.00122T + 0.3} - 0.203 \qquad$ for $500^oC < T \leq 800^oC$
	RM	$1.0 \qquad\qquad$ for $20^oC \leq T \leq 100^oC$ $-0.0013T + 1.1297 \qquad$ for $100^oC < T \leq 800^oC$
	WJ	$-3.298 \times 10^{-9}(T - 21)^3 + 1 \qquad$ for $30^oC \leq T \leq 450^oC$ $-3.057 \times 10^{-3}T + 2.115 \qquad$ for $450^oC < T \leq 600^oC$
	LSB	$-0.0009T + 1.018 \qquad$ for $20^oC \leq T < 500^oC$ $-0.002T + 1.568 \qquad$ for $500^oC \leq T \leq 600^oC$
β	LMM	3.5(20-300ºC), 0.8(400ºC), 0.45(500ºC), 0.1(600ºC), 0.02(700ºC), 0.001(800ºC)
	RM	0.86
	WJ	$0.002 / \left(\dfrac{\sigma_{y.T}}{E_T}\right)$
	LSB	0.86
η_T	LMM	15
	RM	$-3.05 \times 10^{-7}T^3 + 0.0005T^2 - 0.2615T + 62.653 \qquad$ for $20^oC \leq T \leq 800^oC$
	WJ	$2.823 \times 10^{-4}T^2 - 1.071 \times 10^{-1}T + 26.02 \qquad$ for $0^oC \leq T \leq 300^oC$ $3.466 \times 10^{-4}T^2 - 3.195 \times 10^{-1}T + 83.97 \qquad$ for $300^oC < T \leq 527^oC$ $1.485 \times 10^{-3}T^2 - 1.497T + 388.4 \qquad$ for $527^oC < T \leq 600^oC$
	LSB	$-1 \times 10^{-8}T^4 + 9.061 \times 10^{-6}T^3 - 0.0025881T^2 + 0.2105597T + 14.753 \qquad$ for $20^oC \leq T < 400^oC$ $-0.000925T^2 + 1.1675T - 307.5 \qquad$ for $400^oC \leq T \leq 600^oC$

Comparing the experimental results and the constitutive relationships proposed by the researchers above cited, a clear distinction is observed in the shapes of the stress-strain-temperature curves obtained, as revealed by Figure 2.11. Indeed, different interpretations of the steel constitutive models are displayed, therefore it is worth understanding the normative prescriptions related to this subject.

2.5 Eurocode 3 Part 1.2 - Steel Constitutive Model

According to a study performed by KIRBY and PRESTON [45], based on HRS grades, EC3-1.2 [24] provides analytical expressions to define the steel constitutive law at elevated temperatures. As expected, such expressions (summarized in Eq. 2.6) may not describe accurately the temperature dependence of the CFS stress-strain curve.

$$\sigma_T = \begin{cases} \varepsilon \cdot E_T & \text{for } \varepsilon \leq \varepsilon_{p.T} \\ \sigma_{p.T} - c + (b/a)\left[a^2 - \left(\varepsilon_{y.T} - \varepsilon\right)^2\right]^{0.5} & \text{for } \varepsilon_{p.T} < \varepsilon < \varepsilon_{y.T} \\ \sigma_{y.T} & \text{for } \varepsilon_{y.T} \leq \varepsilon \leq \varepsilon_{u.T} \end{cases} \quad \text{(Eq. 2.6)}$$

$$\varepsilon_{p.T} = \sigma_{p.T}/E_T, \quad \varepsilon_{y.T} = 0.02,$$

$$a^2 = \left(\varepsilon_{y.T} - \varepsilon_{p.T}\right)\left(\varepsilon_{y.T} - \varepsilon_{p.T} + c/E_T\right), \quad b^2 = c\left(\varepsilon_{y.T} - \varepsilon_{p.T}\right)E_T + c^2,$$

$$c = \frac{\left(\sigma_{y.T} - \sigma_{p.T}\right)^2}{\left(\varepsilon_{y.T} - \varepsilon_{p.T}\right)E_T - 2\left(\sigma_{y.T} - \sigma_{p.T}\right)}$$

The set of equations is divided into three different regions, associated with distinct strain ranges. Note that (*i*) the effective yield stress $\sigma_{y.T}$ corresponds directly to the yield strain $\varepsilon_{y.T}$ value (*2%* absolute) and that (*ii*) the stress-strain curve shape is strongly influenced by the temperature, namely via the proportional limit strain ($\varepsilon_{p.T} = \sigma_{p.T}/E_T$). As shown in Figure 2.11, for elevated temperatures, the initial part of the well-defined yield plateau exhibited by the *T=20* °C curve is replaced by a strain-hardening region that becomes more pronounced as the temperature increases. The stress-strain curve (*i*) is linear elastic, with slope E_T, up to the proportional limit $\sigma_{p.T}$, then (*ii*) becomes elliptic in the transition between the elastic and plastic ranges, up to $\sigma_{y.T}$ (effective yield stress), and (*iii*) ends with a yield plateau up to the limit strain $\varepsilon_{u.T} = 0.15$.
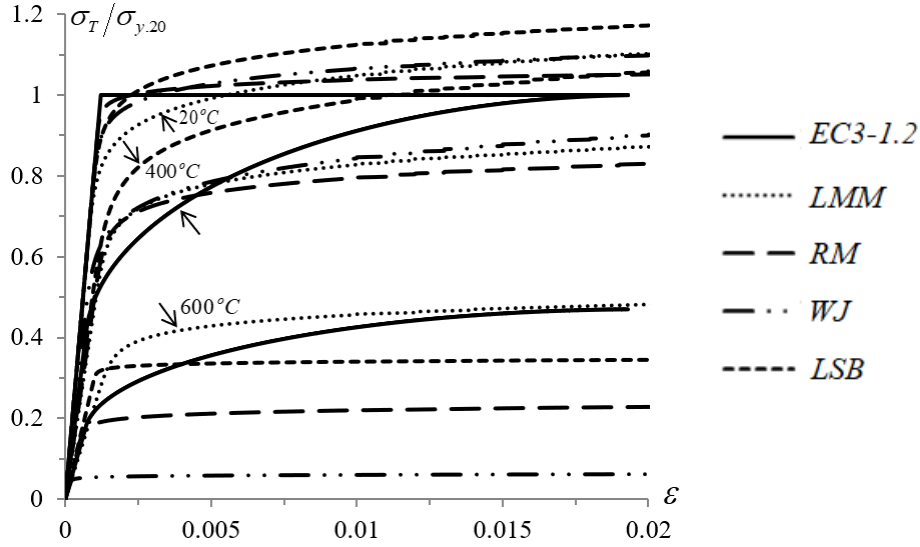
Figure 2.11: Temperature dependence of stress-strain curves, for $T = 20\text{-}400\text{-}600\,°C$, according to the following constitutive models: EC3-1.2, LMM, RM, WJ and LSB.

The temperature dependence is taken into account through reduction factors applied to the steel Young's modulus, yield stress and proportional limit stress. Firstly, EC3-1.2 [24] prescribes such reduction factors for mechanical properties applicable to HRS members (at elevated temperatures). Indeed, it is well known that these reduction factors do not remain valid for CFS. Thus, to concern such differences, EC3-1.2 treats CFS members similarly to slender thin-walled (*i.e.*, Class 4) hot-rolled and welded ones. The only differences, with respect to the remaining (Class 1, 2, 3) hot-rolled and welded members, involve (*i*) the design yield strength, which should be taken as the *0.2%* proof strength and (ii) the corresponding reduction factors, which are given in Table 2.2.

Table 2.2: Reduction factors according to EC3-1.2 [24].

$T\;(^oC)$	k_y (HRS)	k_y (CFS)	k_p	k_E
20	1.000	1.000	1.000	1.000
100	1.000	1.000	1.000	1.000
200	1.000	0.890	0.807	0.900
300	1.000	0.780	0.613	0.800
400	1.000	0.650	0.420	0.700
500	0.780	0.530	0.360	0.600
600	0.470	0.300	0.180	0.310
700	0.230	0.130	0.075	0.130
800	0.110	0.070	0.050	0.090

Figures 2.12 makes it possible to compare the temperature dependence of the reduction factors k_y prescribed [24] for both HRS and CFS. Note that the HRS ones are higher than the CFS ones for all the considered temperature range. This generates a relevant impact on the column buckling, post-buckling and ultimate strength behaviors.
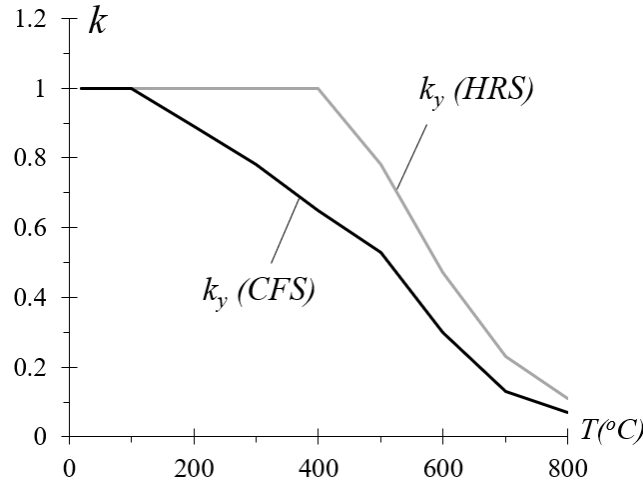
Figure 2.12: Variation of the reduction factors k_y with the temperature T, according to HRS and CFS models [24].

2.6 Available investigations on distortional buckling resistance of CFS columns concerning the effect of temperature dependence

Recent research activities [46]-[60] have taken the first steps towards establishing the fire resistance of CFS structures, including temperature dependence of steel (mechanical properties) behavior. The growing use of CFS systems in the construction industry has attracted efforts for the development of studies focused on CFS performance under fire conditions [61]. According to the approach already discussed in Section 2.4, they are more vulnerable to elevated temperature effects, suffering a rapid loss of strength and stiffness. Indeed, CFS members, as conventionally employed in thin-walled structural systems, have some singular features: they are efficient in terms of strength-to- weight, otherwise significantly more complex than typical HRS members, due to their cold-working process and also their trend to exhibit instability modes (buckling behavior).

Initially, FENG *et al.* [18] performed a detailed experimental campaign destined to study the axial strength of CFS channel section members submitted to room and elevated temperatures. A total of *52* tests were carried out on lipped channels with and without service holes. The results showed that short columns with holes, dominated by

local buckling for $T < 400$ ºC, fail in distortional buckling for higher temperature cases. Further, columns without holes, dominated by distortional mode for $T < 400$ ºC, exhibit local-distortional-global interaction at higher temperatures. As expected, the experimental data confirmed that the axial capacity of columns reduces as the temperatures rise. Then, numerical investigations [19] (based on shell finite element analyses) were developed to simulate the same CFS members under compression at uniform and elevated temperatures, in order to obtain the collapse capacity and to allow comparison of corresponding results.

RANAWAKA and MAHENDRAN [20][21] reported experimental and numerical results concerning fixed-ended lipped channel and rack-section of CFS columns to investigate their distortional buckling behaviors at room and elevated temperatures. Figures 2.13 (a)-(b) illustrate a case of the experimental study that involved more than *150* axial compression tests with *3* nominal thicknesses, *6* different temperatures (*20-200-350-500-650-800* ºC) and both low (G250) and high (G550) strength steels. The numerical analyses displayed finite element models of the tested compression members, concerning the reduction of mechanical properties according to the increasing temperatures. The aim of the researches consisted in (*i*) understanding the pure distortional buckling behavior at uniform elevated temperatures and (*ii*) comparing the ultimate load results with available distortional buckling strength equations based on DSM. The authors addressed the importance of adopting accurate mechanical properties in case of high temperatures, so that it ensures reliable strength data.

In the course of such scientific studies, an extensive database of numerical results was presented [23] involving CFS members subjected to different boundary and loading conditions, under uniform and non-uniform temperatures. The research work concluded that, for uniform elevated temperatures and low-to-moderate slenderness range, the DSM distortional design curves reproduced non-conservative predictions.

As already introduced in Section 2.3.3, SCHAFER [4] collected a large data of experimental failure loads, concerning CFS columns with various cross-section shapes (lipped channels, hats, zeds and racks) failing in local, distortional and global modes. After determining the corresponding critical buckling loads of all the columns involved, with computational effort support, he proceeded to select the strength curves to be included in the DSM design expressions. Nevertheless, the limited scope of concerning columns with only fixed-end support conditions under room temperature compromises the accuracy of the method when it comes to elevated temperature cases.
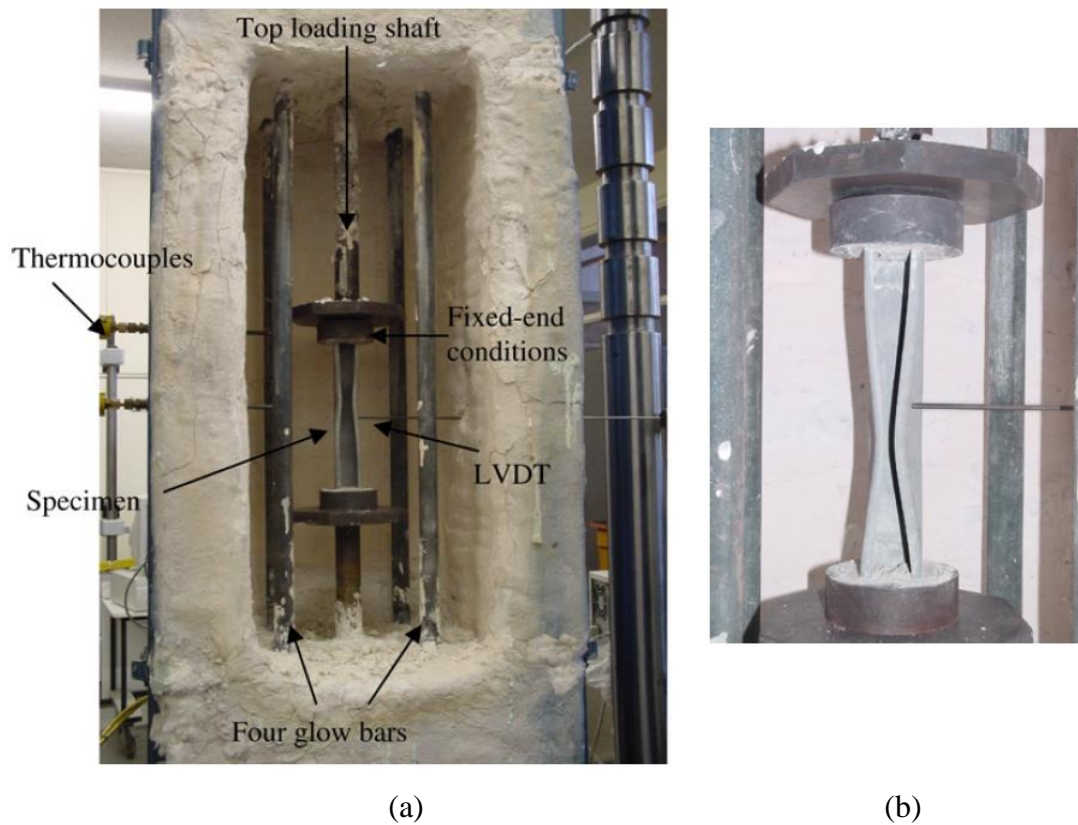
Figure 2.13: Test set-up performed by RANAWAKA and MAHENDRAN [20] for elevated temperatures experimental tests: (a) overall view and (b) specimen at $650\,^{\circ}C$.

Furthermore, the recent finding [17], that confirms the overestimation of failure loads by existing DSM distortional curves considering CFS columns in the low-to-moderate slenderness range, signals the real need to improve visibly the quality of the failure load prediction. In addition, other researchers also studied the temperature effects for the design under fire conditions and had different interpretations of the steel constitutive models prescribed by EC3-1.2 [24]. Consequently, they obtained divergent buckling strength values. In fact, the available results of numerical and experimental buckling analyses are still insufficient to assess the quality and safety of the current DSM curves, concerning fire conditions.

3   Column Geometry Selection and Buckling Behavior

The first stage of the work consisted of defining the geometry of the columns to be analyzed. As previously mentioned, the use of different wall width proportions, namely web-to-flange width ratios, is a way to enable assessing whether such relations have a significant influence on the behavior and distortional post-critical strength of the columns. Furthermore, the adoption of different support conditions and various cross-section shapes are also useful requirements to be considered in the column selection.

In a recent work [17], four cross-section types were analyzed (lipped channel, zed-section, hat-section and rack-section) and the main difference detected in the results was more associated with the wall width proportions variation than the diverse cross-section shapes. It was noted that such varied cross-sections exhibit practically identical distortional and local buckling (bifurcation) loads. Besides, concerning two different support conditions, *i.e.*, "fixed-ended" (F) and "pinned-ended" (P) columns, resulted in distinct distortional failure loads. Obviously, the F columns group presented higher ultimate strength values, when compared the same cross-section shapes and dimensions.

Taking into account the above findings, the column geometry selection covered all the important variations, which involve: two different end support conditions (F and P), lipped channel (C) cross-section shape and three web-to-flange width ratios ($b_w/b_f > 1$, $b_w/b_f = 1$ and $b_w/b_f < 1$). The F support condition concerns the end sections globally (major and minor axis) and locally fixed, with warping prevented, while the P support condition deals with free global and local rotations, as well as the warping displacements. In both cases (F and P), the torsional rotations are prevented.

As done in previous studies [17][22][56]-[58], the buckling analyses required to identify the column geometries were carried out in the code GBTUL, developed by BEBIANO *et al.* [30][31] and based on Generalized Beam Theory (GBT). The adopted method worked by means of a "trial-and-error" buckling analyses, aiming to satisfy the following conditions:

(i)   Columns buckling in "pure" distortional modes, as much as possible, and exhibiting distortional collapses. This goal is achieved by ensuring that the

critical buckling load is clearly distortional and falls considerably below the lowest local and global bifurcation loads.

(ii)   Cross-section dimensions associated with "pure" distortional failures. This requirement is not essential, but it makes the performance of the parametric study easier.

(iii)   Column lengths associated with single half-wave distortional buckling modes.

(iv)   Cross-section dimensions involving different wall width proportions, namely web-to-flange width ratios, as already mentioned.

Trying to fulfill most of above requirements, the selection procedure resulted in three cross-section dimensions (b_w, b_f, *lip*, t − web-flange-lip widths and wall thickness) given in Table 3.1 (see also the figure below). The web-to-flange width ratios (b_w/b_f) are approximately equal to *1.44*, *1.00* and *0.71*. These cross-section dimensions make it possible to select column lengths (L_D) ensuring, as much as possible, pure distortional critical (half-wave) buckling mode. Table 3.2, in turn, provides, for each lipped channel column, the corresponding two sets (P and F columns) of (*i*) lengths associated with distortional buckling (L_D), (*ii*) corresponding buckling loads at room temperature ($P_{cr.D.20}$) and (*iii*) their ratios with respect to the lowest local ($P_{L.20}$) and global ($P_{G.20}$) buckling loads − all buckling loads were calculated for $E_{20}=205$ GPa (steel Young's modulus at room temperature) and $v=0.3$ (Poisson's ratio, assumed independent of the temperature). It is observed that the first "non-distortional" buckling load always corresponds to local buckling, with $P_{L.20}/P_{cr.D.20}$ ratio varying between *1.46* and *2.44* (for P columns) and *1.25* and *1.54* (for F columns). Moreover, the first global (flexural-torsional or flexural) buckling load is invariably much higher, with the $P_{G.20}/P_{cr.D.20}$ ratio varying from *28.52* to *44.10* (for P columns) and from *32.18* to *77.00* (for F columns).

Table 3.1: Cross-section dimensions and areas of the selected columns.

Lipped channel columns	b_w (mm)	b_f (mm)	b_w/b_f (mm)	lip (mm)	t (mm)	Area (cm²)
C200x140	197.4	137.4	1.437	13.7	2.6	12.99
C200x200	197.4	197.4	1.000	13.7	2.6	16.11
C200x280	197.4	277.4	0.712	13.7	2.6	20.27
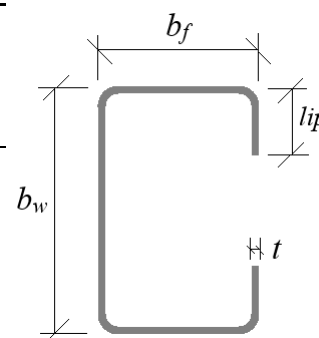
Table 3.2: Lengths, critical buckling loads and bifurcation-to-critical load ratios of the lipped channel columns.

Lipped channel columns	Pinned (P)				Fixed (F)			
	L_D (cm)	$P_{cr.D.20}$ (kN)	$\dfrac{P_{L.20}}{P_{cr.D.20}}$	$\dfrac{P_{G.20}}{P_{cr.D.20}}$	L_D (cm)	$P_{cr.D.20}$ (kN)	$\dfrac{P_{L.20}}{P_{cr.D.20}}$	$\dfrac{P_{G.20}}{P_{cr.D.20}}$
C200x140	70	149.7	1.46	28.52	110	214.8	1.25	32.18
C200x200	90	99.2	2.23	34.51	120	151.8	1.50	50.72
C200x280	110	65.7	2.44	44.10	130	107.7	1.54	77.00

3.1   Signature curves - variation of elastic critical buckling loads

For illustrative purposes, the curves depicted in Figures 3.1 (a)-(b) provide the variation of $P_{cr.T}$ (elastic critical buckling loads for different temperatures) with the length L (logarithmic scale) and temperature T for P and F columns with the lipped channel cross-section dimensions selected (C200x140, C200x200 and C200x280). Four temperatures are considered (room/moderate temperature *20/100 °C*, *400 °C*, *600 °C* and *800 °C*) and the EC3-1.2 [24] constitutive model for CFS is adopted. Also shown are the critical (distortional) buckling mode shapes of P columns, with *L_D=70-90-110cm*, and F columns, with *L_D=110-120-130cm*, concerning C200x140, C200x200 and C200x280, respectively. Note that (*i*) any given buckling curve can be obtained through a "vertical translation" of the top one, with a magnitude that depends exclusively on the Young's modulus erosion (application of reduction factors) due to the rising temperature, and that (*ii*) the critical distortional load $P_{cr.D.T}$ corresponds to the same length (L_D) for each temperature value.
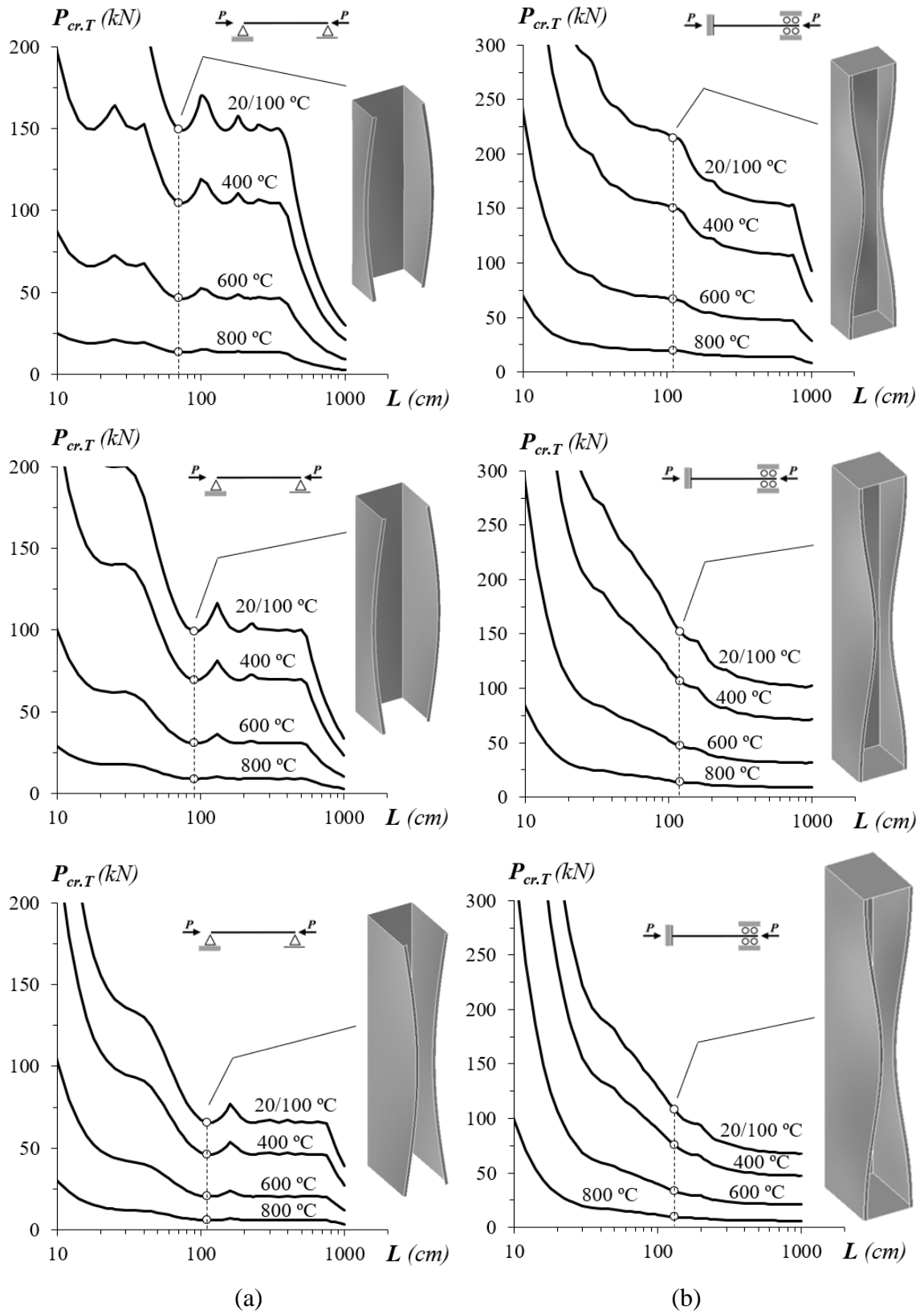
Figure 3.1: Variation of $P_{cr.T}$ with L and T for (a) P and (b) F lipped channel columns (C200x140, C200x200 and C200x280, respectively), concerning EC3-1.2 model.

4   Numerical Model – Finite Element Analysis

The column distortional post-buckling analyses were carried out in the code ANSYS [62], employing a shell finite element model, which was based on previous validated studies [22][56][57]. The analyses involve column discretizations into fine SHELL181 (ANSYS nomenclature) element meshes – *4*-node shear deformable thin-shell elements with six degrees of freedom per node and full integration, as schematically specified in Figure 4.1. According to the convergence studies performed [22][56][57], *5mm × 5mm* meshes provide accurate results, while involving a reasonable computational effort. Both the residual stresses and corner effects were neglected since their combined influence on the column strength has been shown to be negligible by several authors (*e.g.*, ELLOBODY and YOUNG [63]).
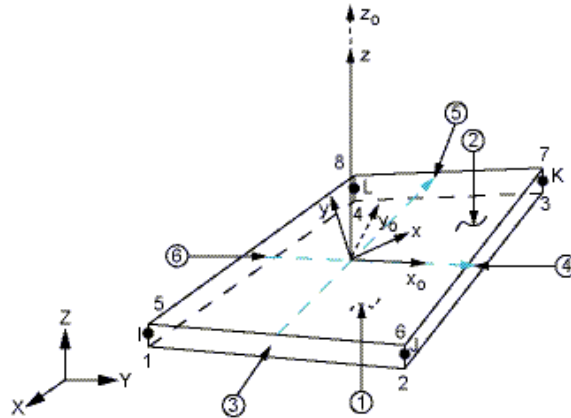
Figure 4.1: Typical SHELL181 (ANSYS nomenclature) element [62].

4.1   Mesh convergence test

Aiming to streamline the analyses processing without compromising the quality of results, a new convergence study was developed to estimate the most efficient element size/dimension for the finite element analyses (FEA) of the present work. Three element sizes were considered: *5mm × 5mm*, *7.5mm × 7.5mm* and *10mm × 10mm* meshes, as presented in Figure 4.2 (a, b and c, respectively). For each mesh discretization type and support condition (P and F), the distortional post-buckling analyses were carried out concerning three distortional slenderness values ($\lambda_{D.20}$) at room temperature: *0.5*, *1.6* and

2.5. The $P_u/P_{u.0.5}$ failure loads ratio values are listed in Table 4.1; note that the case with *10mm × 10mm* mesh provides sufficiently accurate results, once its highest variation is in the range of *0.4%* (negligible) when compared to the option already validated [22][56][57], *i.e.*, *5mm × 5mm* meshes.

(a)

(b)

(c)
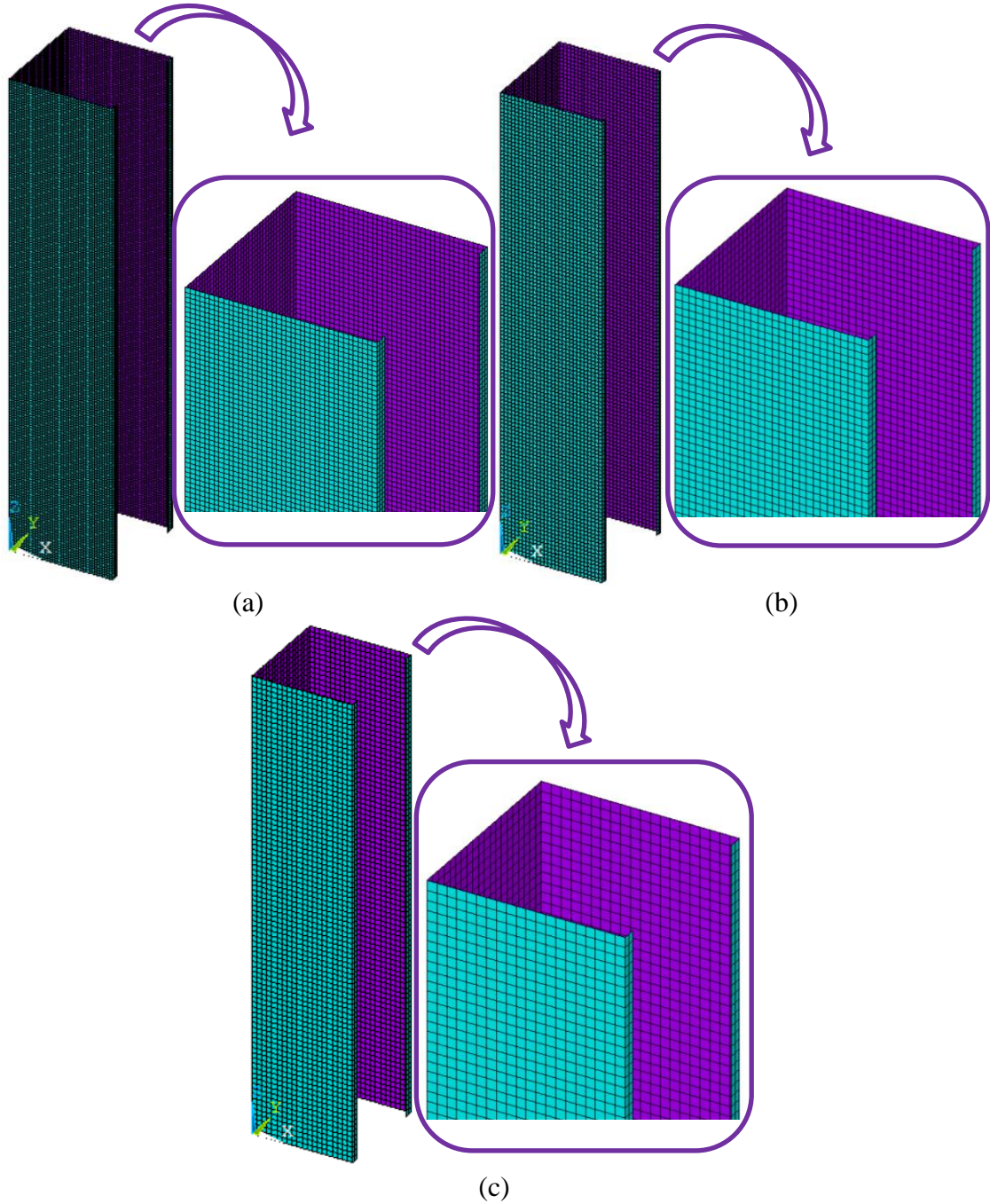
Figure 4.2: Element sizes/dimensions considered in the mesh convergence tests for the P column C200x200: (a) *5mm×5mm*, (b) *7.5mm×7.5mm* and (c) *10mm×10mm* meshes.

Thereby, taking into account the convergence analysis, the computational efficiency and the functionality of mesh generation, the shell finite element dimensions (SHELL181 − ANSYS nomenclature) were finally defined with the *10mm × 10mm* mesh configuration. This discretization option led to faster processing and, thus, allowed to evaluate a significant quantity of columns.

Table 4.1: $P_u/P_{u.0.5}$ ratios for each element mesh, considering C200x200 column.

Distortional Slenderness ($\lambda_{D.20}$)	Shell finite element mesh (mm × mm)					
	P column			F column		
	5×5	7.5×7.5	10×10	5×5	7.5×7.5	10×10
0.5	1.000	1.001	1.000	1.000	1.000	1.000
1.6	1.000	1.138	1.003	1.000	0.999	0.999
2.5	1.000	1.197	1.004	1.000	1.000	1.001

4.2   Analysis method and geometry specifications

The FEA were performed by means of an incremental-iterative technique combining Newton-Raphson's method with an arc-length control strategy. This process allowed to simulate the response of columns subjected to an uniform temperature distribution (*i.e.*, they are deemed engulfed in flames and, thus, share the surrounding air temperature [64]) and subsequently axially compressed up to failure. It is important to emphasize that only steady state analyses were used to provide failure loads.

The columns analyzed contained initial geometrical imperfections with a critical-mode (distortional) shape and amplitude equal to *10%* of the wall thickness *t*. Due to the column distortional post-buckling asymmetry, these initial imperfections involve both outward (in case of P columns) and inward (in case of F columns) flange-lip motions. These choice depends on the configuration that leads to lower post-buckling strengths, as already attested [65][66]. Each critical buckling mode shape was determined by means of an ANSYS buckling analysis, performed with exactly the same shell finite element mesh employed to carry out the subsequent non-linear (post-buckling) analysis − this procedure makes it very easy to "transform" the buckling analysis output into a non-linear analysis input.

As mentioned earlier, the lipped channel columns used in the present work exhibit two end support conditions: "pinned-ended" (P) and "fixed-ended" (F). In the pinned support, the membrane and bending transverse displacements (X and Y axis) of all end section nodes were prevented, while keeping the axial (warping) displacements and all the rotations free, as shown in Figures 4.3 (a)-(b). On the other hand, the fixed support was modelled by means of rigid end-plates attached to the end cross-section centroids, precluding the occurrence of local and global displacements (X and Y axis) and rotations (X, Y and Z axis), as well as warping (see Figures 4.4 (a)-(b). In both cases (P and F), the rigid-body axial translation was free at the end sections to enable the load application. Finally, the axial compression was applied by means of a set of concentrated forces acting on the end nodes, for P columns, and as a concentrated force applied on the rigid end-plate points corresponding to the cross-section centroids. Such forces are applied in small increments, by means of the ANSYS automatic load stepping procedure.

(a)   (b)
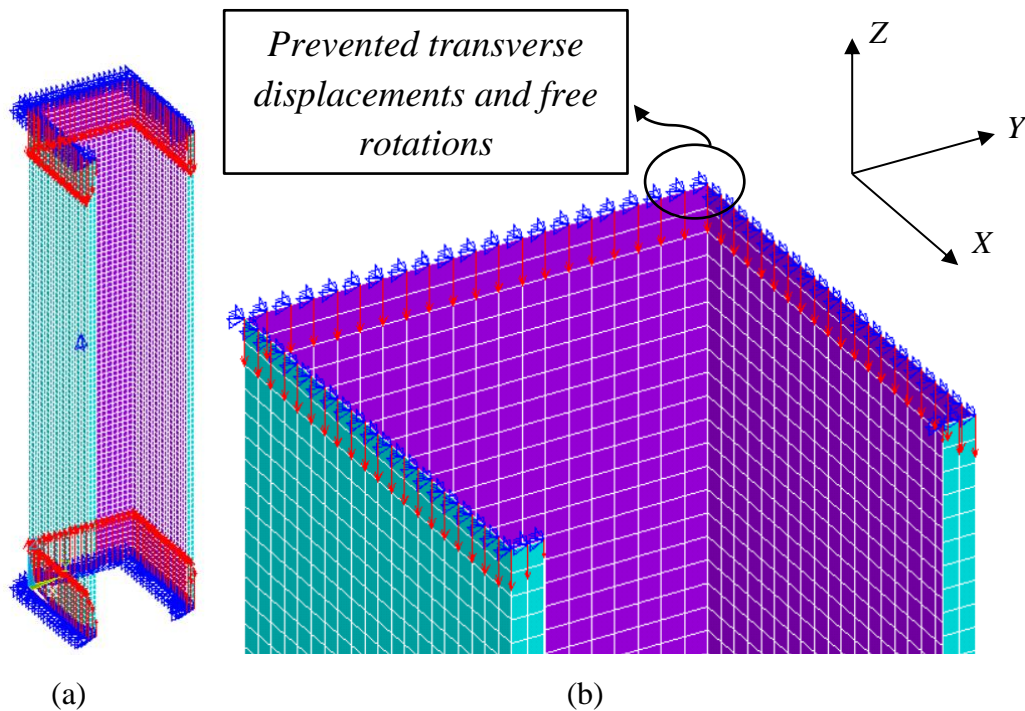
Figure 4.3: Pinned end support conditions represented by (a) isometric view of full geometric model and (b) detail view of the applied compression load.
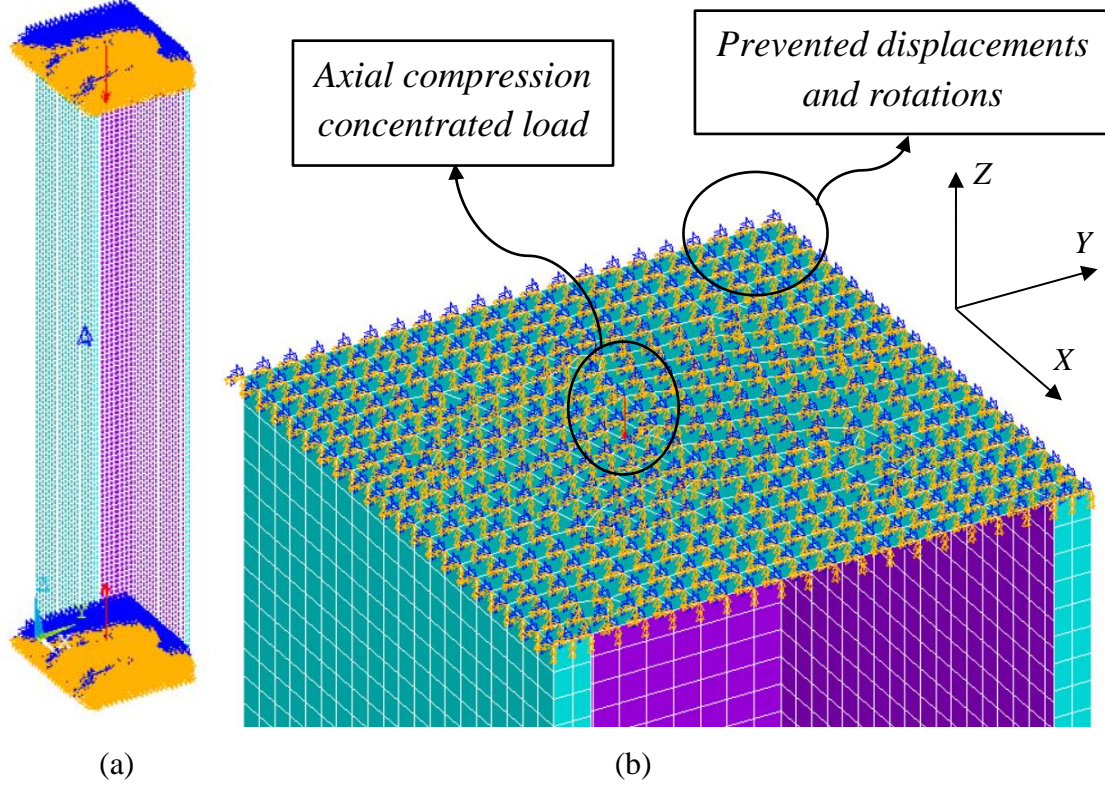
Figure 4.4: Fixed end support conditions represented by (a) isometric view of full geometric model and (b) detail view of rigid end-plate with the applied compression load.

4.3 Steel material behavior

The multi-linear isotropic hardening plasticity stress-strain curve available in ANSYS was adopted to model the steel material behavior corresponding to several yield stresses. Employing such multi-linear model, the program allows to define up to *100* points for composing the stress-strain curve, ensuring, as much as possible, a very well-defined tracing. In order to take full advantage of the ANSYS' capacity and precisely simulate the CFS material behavior, the maximum value of *100* points were specified and used to define all the constitutive relationships considered in the shell FEA (different room yield stress values covering distortional slenderness range from *0.1* to *3.5*). This action contributes significantly to the reduction of convergence problems, often common in such robust non-linear analyzes.

The CFS constitutive law at elevated temperatures adopted in this work is defined by the analytical expressions prescribed in Part 1.2 of Eurocode 3 (EC3-1.2 [24]), as presented earlier in Section 2.5. The standard formulation considers the temperature dependence effect by applying reduction factors to the cold-formed steel Young's modulus ($k_E = E_T/E_{20}$), the nominal yield stress ($k_y = \sigma_{y.T}/\sigma_{y.20}$, concerning *0.2%* proof strength) and the proportional limit stress ($k_p = \sigma_{p.T}/\sigma_{y.20}$), as listed in Table 4.2 and also represented in Figure 4.5 (a).

Table 4.2: Reduction factors for elevated temperatures (EC3-1.2 model [24]).

Reduction factors	Temperatures T (^{o}C)							
	20/100	200	300	400	500	600	700	800
k_y	1.000	0.890	0.780	0.650	0.530	0.300	0.130	0.070
k_E	1.000	0.900	0.800	0.700	0.600	0.310	0.130	0.090
k_p	1.000	0.807	0.613	0.420	0.360	0.180	0.075	0.050

As for Figure 4.5 (b), it illustrates the qualitative differences between the stress-strain curves prescribed [24] for $T=20/100$°C (room/moderate temperature) -200-300-400-500-600-700-800°C, $\sigma_T/\sigma_{y.20}$ vs. ε, where the applied stress at a given temperature (σ_T) is normalized with respect to the room temperature yield stress $\sigma_{y.20}$. Its first branch models the linear elastic range, up to the proportional limit stress and with a slope equal to Young's modulus. The following branches stand for the inelastic range, which accounts for (kinematic) strain-hardening, as described by the constitutive model introduced in Section 2.5. Note that the stress-strain curve (*i*) non-linearity increases largely with the temperature (for $T=20/100$ °C, the constitutive law is bi-linear − elastic-perfectly plastic material) and (*ii*) proportionality limit strain ($\varepsilon_{p.T}=\sigma_{p.T}/E_T$) and non-linear shape are considerably influenced by the temperature. It is also worth mentioning that, although the EC3-1.2 model further extends the stress-strain relationship to include strain-hardening, for temperatures below *400* °C (since the strain-hardening influence is negligible for temperatures higher than *400* °C), this effect was not considered in this work, for the reason that EC3-1.2 standard only specifies an increasing steel strength for cases with deformation levels above *2%*.
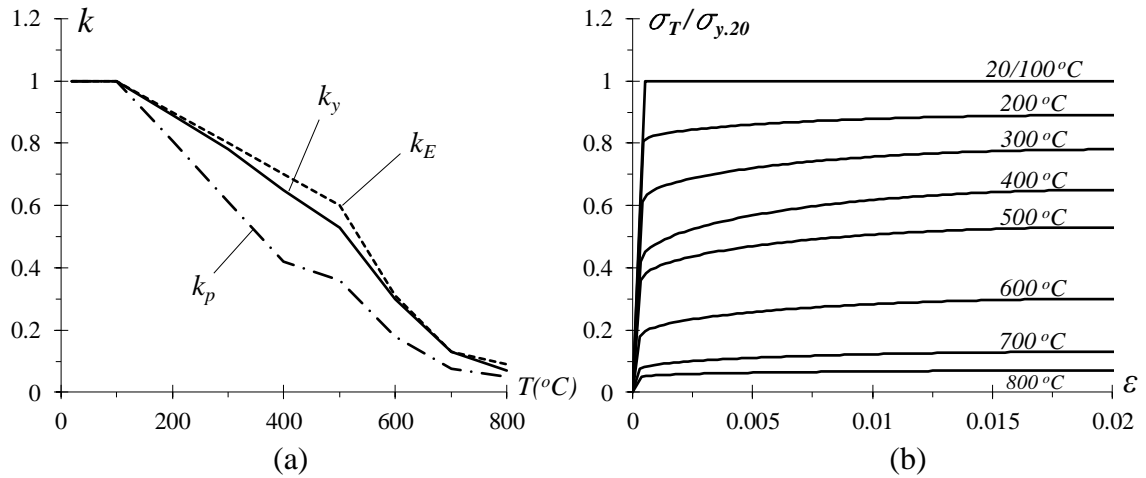
Figure 4.5: (a) Variation of the reduction factors k_y, k_E and k_p with the temperature T and (b) CFS stress-strain-temperature curves $\sigma_T/\sigma_{y.20}$ vs. ε ($\varepsilon \leq 2\%$), for *T=20/100-200-300-400-500-600-700-800 °C*, according to EC3-1.2 [24] model.

5 Distortional Response and Post-Buckling Behavior

5.1 Elastic post-buckling behavior

The elastic post-buckling equilibrium paths show the variation of the $P/P_{cr.D.20}$ ratio with respect to $|\delta|/t$, where $|\delta|$ is the maximum absolute vertical displacement occurring along the flange-stiffener longitudinal edges and t is the wall thickness. Figures 5.1 (a)-(b) exhibit such relation for the P and F lipped channel columns, defined in Section 3 (geometries in Tables 3.1 and 3.2). These figures also include illustrative examples of the shell finite element meshes adopted to analyze the initially imperfect C200x200 P and F columns (in the image, the initial geometrical imperfection is amplified for better viewing). The observation of these six distortional post-buckling equilibrium paths prompts the following remarks:

(i)   As naturally expected, the higher stiffness and strength typical of F columns set are readily confirmed by comparing Figs. 5.1 (a) and 5.1 (b). There is also a clear difference between the shapes of the P and F column equilibrium paths: while the former exhibits a pronounced convexity, associated with a progressive stiffness degradation that leads to elastic limit points, the latter displays a concavity, originated from the stiffness increase provided by the end support warping fixity and precluding the occurrence of elastic limit points (at least for not too high $|\delta|$ values). It is worth pointing that, for both the P and F columns, the equilibrium paths practically coincide up to $|\delta|/t \approx 4$ and $|\delta|/t \approx 2$, respectively.

(ii)   Regarding the influence of the cross-section dimensions on the column post-critical stiffness and strength, there is a visible trend in the F columns: they increase as the web-to-flange width ratio (b_w/b_f) decreases. On the other hand, the opposite order of web-to-flange width ratio (b_w/b_f) values was detected for P columns: the post-critical stiffness and strength increase slightly with b_w/b_f ratios.

(iii)   In view of the above remarks, this study makes it possible to conclude that the column elastic distortional post-buckling stiffness and strength are influenced by both end support condition and web-to-flange width ratio (b_w/b_f). This influence may have non-negligible implications on the column elastic-plastic ultimate strength and, therefore, also on its prediction by design methods.
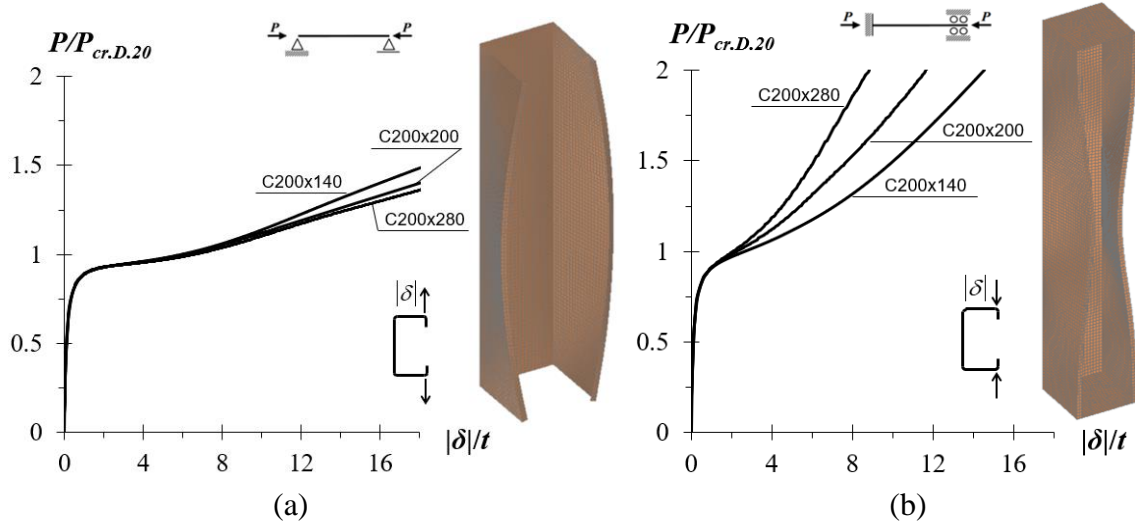
Figure 5.1: Elastic equilibrium paths $P/P_{cr.D.20}$ vs. $|\delta|/t$ concerning (a) P and (b) F lipped channel columns.

5.2 Elastic-plastic post-buckling behavior – room/moderate temperature

At this stage of the work, the ANSYS shell finite element models are used to obtain the elastic-plastic post-buckling behavior of P and F columns buckling and failing under distortional modes at room/moderate temperature. In addition, the ultimate strength values gathered in this FEA enable further evaluation of the performance of currently codified DSM design curves in predicting distortional failure loads.

The numerical results processed in this campaign concern a total of *102* columns, combining (*i*) the *3* columns geometries defined in Tables 3.1 and 3.2, (*ii*) the *2* end support conditions (P and F) and (*iii*) *17* room temperature yield stresses, selected to permit covering wide distortional slenderness ranges for each column set: $\lambda_{D.20}$ varies between *0.10* and *3.50* for both P and F columns – note that $\lambda_{D.20}=(P_{y.20}/P_{cr.D.20})^{0.5}$, where $P_{y.20} = A \times \sigma_{y.20}$ and *A* is the cross-section area (given in Table 3.1). Tables A1 and A9, included in Annex A, provide the distortional slenderness $\lambda_{D.20}$, squash load $P_{y.20}$ and numerical failure load $P_{u.20}$, for each column analyzed.

Figures 5.2 (a)-(b) display a sample of P and F column non-linear equilibrium paths $P/P_{cr.D.20}$ vs. $|\delta|/t$, determined to obtain the failure loads $P_{u.20}$ (identified by white circles) – note that vertical scales differ for the P and F columns. These equilibrium paths concern the *3* columns geometries (C200x140, C200x200 and C200x280) with distortional slenderness $\lambda_{D.20}=0.5$-*0.9*-*1.6*-*2.5*-*3.5* – the elastic paths, already shown in Figures 5.1 (a)-(b), are displayed again for comparison purposes. Figures 5.4 (a)-(b), presented in the next item (in advance, concerning elevated temperatures), depict the

39

deformed configurations and von Mises stress ($\sigma_{v.M}$) contours, at the peak load, of the P and F C200x200 columns (just for instance) with $\lambda_{D.20}=1.6$ – the distortional nature of the column collapse is clearly visible (given that the deformed configuration for moderate temperature is qualitatively similar to *200* ºC case). The observation of the results prematurely addressed in the above figures and the data provided in Tables A1 and A9 leads to the following conclusions:

(a)   (b)
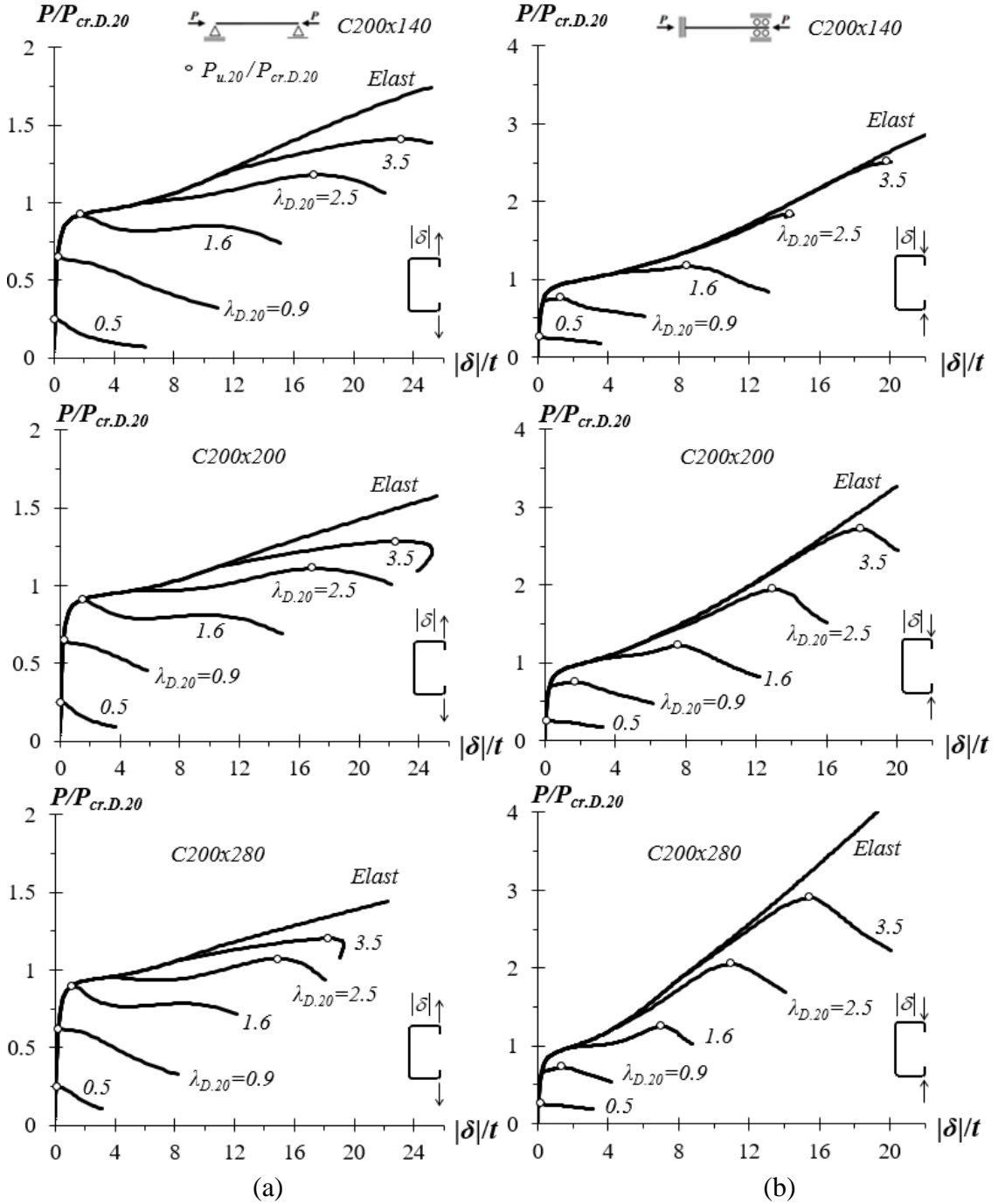
Figure 5.2: Room/moderate temperature elastic-plastic distortional equilibrium paths ($P/P_{cr.D.20}$ vs. $|\delta|/t$) concerning (a) P and (b) F columns with $\lambda_{D.20}=0.5$-0.9-1.6-2.5-3.5.

(i)   The P column elastic-plastic post-buckling behavior and strength are different from their F column counterparts, both qualitatively and quantitatively – note that the F column values only exceed their P column counterparts for very high $\lambda_{D.20}$ values (*i.e.*, very high yield stresses $\sigma_{y.20}$).

(ii)   As expected, the failure load ratio $P_{u.20}/P_{cr.D.20}$ increases with $\lambda_{D.20}$ for all columns, regardless of their end support conditions (P or F).

(iii)   Both P and F columns exhibit similar single half-wave distortional buckling and collapse modes. The latter is associated with the full yielding of the mid-height web-flange corner region, leading to the formation of an "X-shaped distortional plastic hinge", which means that plasticity also spreads throughout the mid-height flange and lip regions.

5.3   Elastic-plastic post-buckling behavior – elevated temperatures

In this section, the distortional elastic-plastic post-buckling behavior of P and F lipped channel columns is examined concerning the influence of elevated temperatures. The steel constitutive model used to simulate the temperature dependence follows the prescription of EC3-1.2 [24]. Figures 5.3 (a)-(b) show the non-linear equilibrium paths ($P/P_{cr.D.20}$ vs. $|\delta|/t$) of P and F columns with $\lambda_{D.20}$=1.6 under temperatures *T=20/100-200-300-400-500-600-700-800* ºC. The white circles identify the failure loads ($P_{u.T}$) normalized with respect to the buckling loads at room temperature ($P_{cr.D.20}$). The graphics also present the room/moderate temperature elastic curves (displayed again for comparative purposes) and the elastic-plastic curves concerning high temperatures. At this point of the research, it is interesting to observe and evaluate the deformed configurations and von Mises stress contours displayed in Figures 5.4 (a)-(b). Both effects were registered exactly at the collapse moment, when $P=P_{u.T}$, for those columns submitted to temperatures *T=200-400-600-800* ºC, and contributed to the following findings:

(i)   Naturally, the various column equilibrium paths "move down" as the temperature rises, which implies that the failure load decreases.
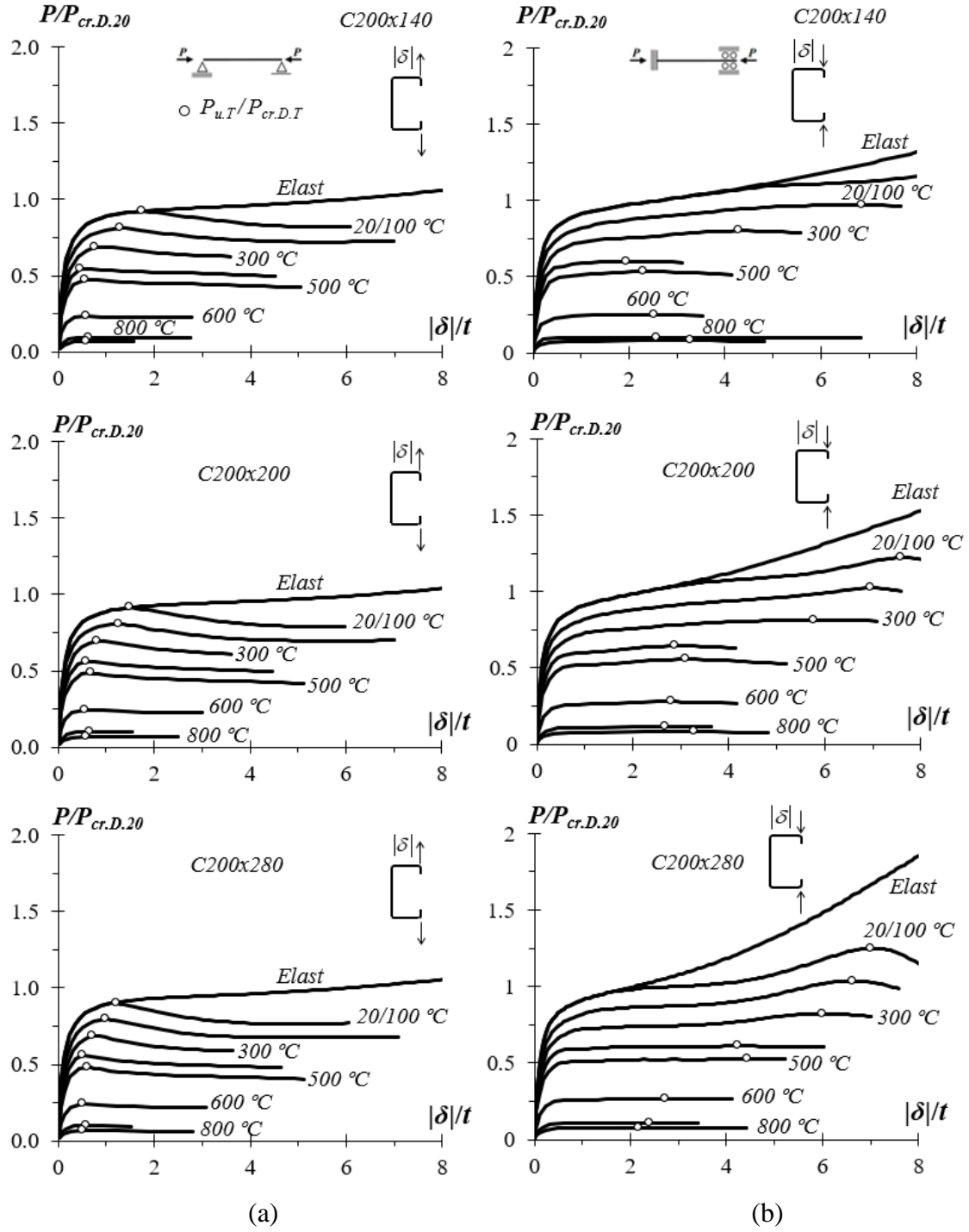
Figure 5.3: Distortional post-buckling equilibrium paths for $\lambda_{D.20}=1.6$ and temperatures $T=20/100\text{-}200\text{-}300\text{-}400\text{-}500\text{-}600\text{-}700\text{-}800\,^{\circ}C$, considering (a) P and (b) F columns.

(ii)   Since the thermal action effects are negligible (uniform temperature and free-to-deform columns), the distortional failure modes do not depend on the temperature and, therefore, reveal very similar configurations in all the *48* columns analyzed, as shown in Figures 5.4 (a)-(b). However, such identification

does not extend to the corresponding von Mises stress contours, which are qualitatively resembling amongst themselves, but, as expected, quantitatively different, also with respect to the room temperature cases. Indeed, the stresses obviously decrease as the temperature rises and continuously erodes the steel material behavior. In addition, the spread of plasticity in the flange, associated with the formation of the "distortional plastic hinge", becomes gradually less pronounced as T rises. This stems directly from the temperature dependence of the stress-strain curve shape, remembering that k_p=0.807-0.42-0.18-0.05 for T=200-400-600-800 °C (the reduction factors of the proportional limit stress are higher for lower temperatures and decrease as temperatures rise).

(iii)   The $T \geq 600$ °C curves are clearly below their $T \leq 500$ °C counterparts (such assertion can be checked in Figures 5.3 (a)-(b) plots). This reflects the heavy degradation of the steel material behavior between *500* °C and *600* °C, as well as manifested via the decay of proportional limit strain, which is related to the transition point from the elastic to plastic ranges on the stress-strain-temperature curves. It is worth pointing that the application of reduction factors has a significant impact in this stage of the research findings. According to Section 4.3, the evolution of k_p (and also k_y and k_E) indicates a substantial decrease at this temperature zone.
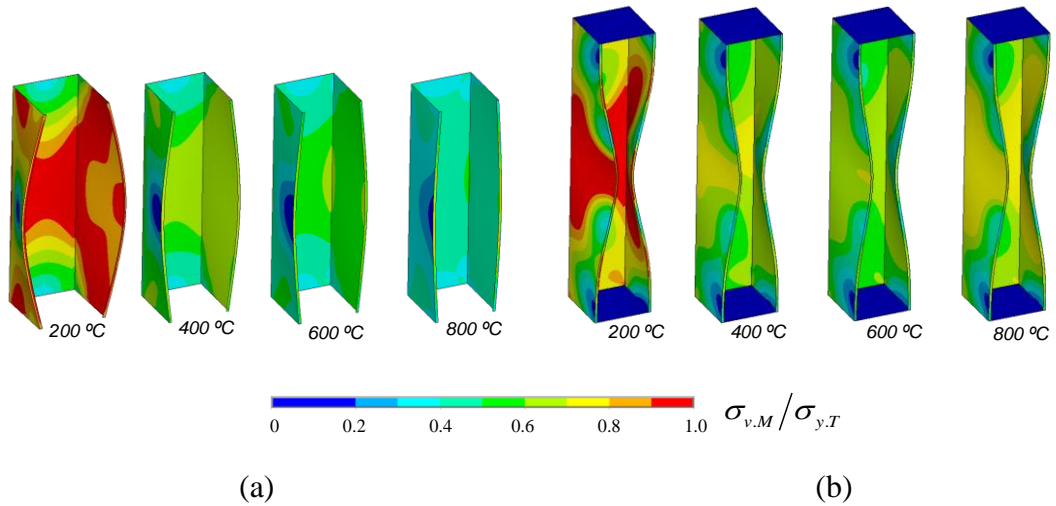
Figure 5.4: Deformed configuration and von Mises stress contours at collapse, for $\lambda_{D.20}$=1.6 and temperatures T=200-400-600-800 °C, concerning (a) P and (b) F C200x200 columns.

5.4 Ultimate strength – room/moderate temperature

Attention now is devoted to the results of the parametric study carried out to gather failure load data that will enable the assessment of the DSM estimates (main topic of next chapter), concerning room/moderate temperature.

First of all, Figures 5.5 (a)-(b), presented in the sequence, should be carefully analyzed. They plot, respectively, the P and F lipped channel column failure load ratios $P_{u.20}/P_{cr.D.20}$ against $\lambda_{D.20}$. In order to provide a sufficiently satisfactory observation of the symbols used in the graphics, so that it is possible to note the differences among the results of each column set, the $P_{u.T}/P_{cr.D.20}$ values are represented by (*i*) white, gray and black circles for P columns with $b_w/b_f > 1$, $b_w/b_f = 1$ and $b_w/b_f < 1$, respectively (*i.e.*, C200x140, C200x200 and C200x280, in this order), and (*ii*) white, gray and black triangles for F columns with $b_w/b_f > 1$, $b_w/b_f = 1$ and $b_w/b_f < 1$, also in this order. Such distinction favors the study of the influence of web-to-flange width ratio b_w/b_f on the failure load data. The results shown in these figures and given in Tables A1 and A9 (for room/moderate temperatures) make it possible to conclude that:

(*i*)   Naturally, the failure load ratios $P_{u.20}/P_{cr.D.20}$ of all columns analyzed increase with the distortional slenderness $\lambda_{D.20}$, regardless of the cross-section dimensions and end support conditions.

(*ii*)   All columns failing below the critical axial load level (*i.e.*, $P_{u.20}/P_{cr.D.20} < 1$) exhibit a rather small elastic-plastic strength reserve and very little ductility prior to failure. Moreover, there are no visible qualitative differences between the values concerning the P and F columns. This assertion does not remain valid when $P_{u.20}/P_{cr.D.20} > 1$: while the P columns collapse almost immediately after the onset of yielding, the F columns exhibit a considerable elastic-plastic strength reserve, which is a direct consequence of the elastic post-buckling differences addressed earlier.

(*iii*)   The F-column plot $P_{u.20}/P_{cr.D.20}$ vs $\lambda_{D.20}$ is practically linear. For $\lambda_{D.20} \leq 1.3$, all the $P_{u.20}/P_{cr.D.20}$ values align along the same line. This is no longer true for $\lambda_{D.20} > 1.3$, as the $P_{u.20}/P_{cr.D.20}$ values exhibit a small amount of scatter. Indeed, it seems possible to establish a correlation between the slope of the $P_{u.20}/P_{cr.D.20}$ vs. $\lambda_{D.20}$ plot and the value of the width ratio b_w/b_f: the slope decreases when b_w/b_f grows − in particular, note that the values concerning the columns with $b_w/b_f > 1$

are visibly below the remaining ones. On the other hand, it is also clear that there is no influence of the b_w/b_f ratio on the $P_{u.20}/P_{cr.D.20}$ vs. $\lambda_{D.20}$ plot for the P columns with $\lambda_{D.20} \leq 2.2$ – this plot exhibits a well defined bi-linear shape, with the change (drop) in slope occurring for $\lambda_{D.20} \approx 1$. However, in fact, for P columns with $\lambda_{D.20} > 2.2$, the effect detected corresponding to the web-to-flange width ratio b_w/b_f also occurs, but in the opposite order: the slope increases as b_w/b_f grows.
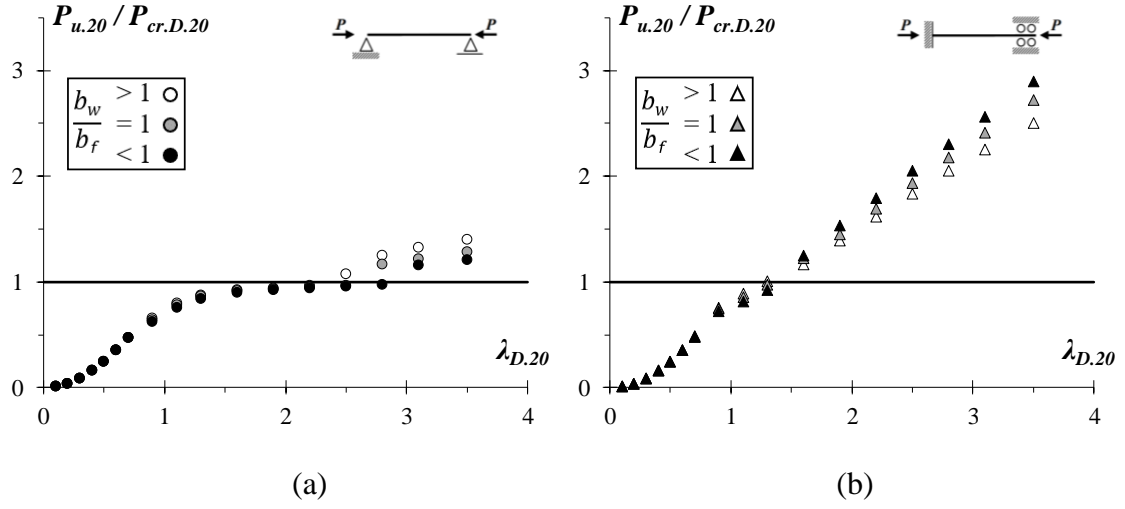
Figure 5.5: Numerical $P_{u.20}/P_{cr.D.20}$ values plotted against $\lambda_{D.20}$, concerning (a) P and (b) F lipped channel column failure loads obtained in this work.

In the sequence, Figures 5.6 (a)-(b) plot the failure load ratios $P_{u.20}/P_{y.20}$ against the $\lambda_{D.20}$ for the *102* P and F columns failure loads obtained in this work and also the fairly large set of experimental values reported by SANTOS [67] and SCHAFER [4][29], concerning P and F columns, respectively. The observation of these results leads to the following remarks:

(i) Although both $P_{u.20}/P_{y.20}$ vs. $\lambda_{D.20}$ "clouds" clearly align along "Winter-type" strength/design curves, a sizeable $P_{u.20}/P_{y.20}$ "vertical dispersion" occurs in the F columns – such dispersion practically does not exist in the P column $P_{u.20}/P_{y.20}$ values (obtained in this work and reported by SANTOS [67]).

(ii) Like the $P_{u.20}/P_{cr.D.20}$ ratio, the $P_{u.20}/P_{y.20}$ is also clearly influenced by b_w/b_f, as far as the F columns are concerned – see the vertical dispersion of the failure loads obtained in this work in Figure 5.6 (b) and note that $P_{u.20}/P_{y.20}$ increases as

b_w/b_f decreases. On the other hand, the above influence is again undetected in the P columns.

(iii) The experimental F column failure loads reported in [4][29], which involve mostly columns with $b_w/b_f > 1$, also align along a "Winter-type" curve and "mingle" reasonably well with the results obtained in this work, even if they exhibit a significant vertical dispersion. Similarly, the experimental P column failure loads reported in [67] interflow with the results obtained in this work as well.
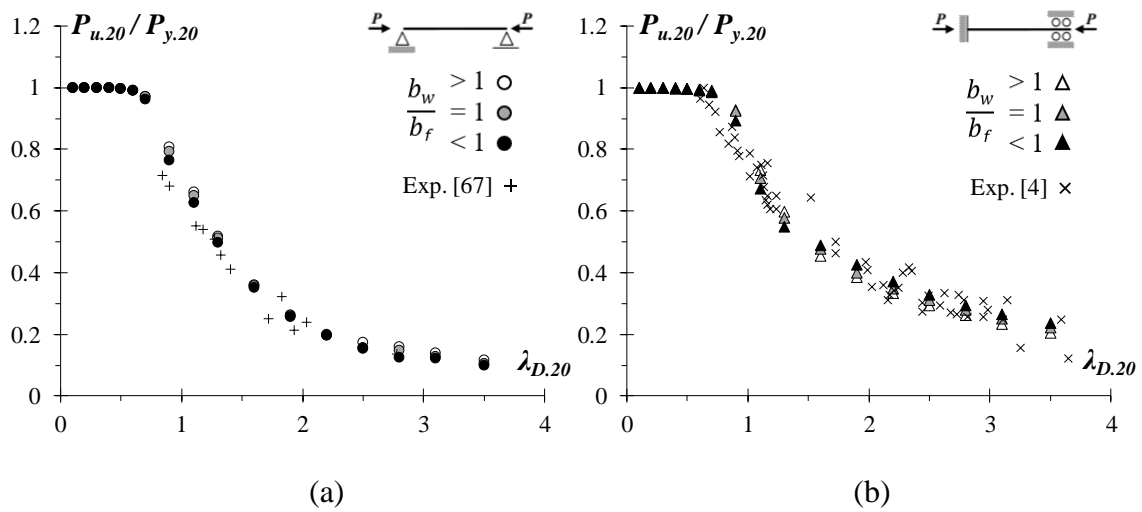
Figure 5.6: Numerical $P_{u.20}/P_{y.20}$ values plotted against $\lambda_{D.20}$, concerning (a) P and (b) F lipped channel column failure loads obtained in this work and reported by SANTOS [67] and SCHAFER [4] for P and F columns, respectively.

5.5 Ultimate strength – elevated temperatures

This section presents the output of the parametric study developed to obtain failure loads considering elevated temperatures. These column distortional failures are essential for examining the merits of DSM design approaches under such special conditions. A total of *816* columns are analyzed, corresponding to all possible combinations of (*i*) the *3* geometries defined in Tables 3.1 and 3.2, (*ii*) the P and F end support conditions, (*iii*) *8* uniform temperatures (*T=20/100-200-300-400-500-600-700-800 ℃*)[1] and (*iv*) *17* room

---

[1] The room/moderate temperature failure loads obtained in this work, already presented in Section 5.4, are displayed again for comparative purposes.

temperature yield stresses, which enable covering wide distortional slenderness ranges: $\lambda_{D.T}$ varies from *0.1* to *3.5*. The numerical failure loads obtained in this work are provided in sixteen tables included in Annex A: Tables A2 to A8 (for P columns) and A10 to A16 (for F columns) – each table groups the *3* column geometries related to a given elevated temperature. The tables provide the values of the distortional slenderness $\lambda_{D.T}$, squash load $P_{y.T}$ and failure load $P_{u.T}$. Figures 5.7 and 5.8, concerning P and F columns, respectively, plot the failure load ratios $P_{u.T}/P_{y.T}$ against $\lambda_{D.T}$ for each temperature value. The joint analysis of these results prompts the following conclusions:

(i)   Regardless of the temperature, the $P_{u.T}/P_{y.T}$ vs. $\lambda_{D.T}$ "clouds" follow the trend of "Winter-type" strength curves and exhibit a small amount of "vertical dispersion" along the slenderness range considered, which reflects the influence of the web-to-flange width proportions and geometry of the lipped channel columns on the distortional post-critical strength. Qualitatively speaking, the temperature rise does not alter the traits detected in Figures 5.6 (a)-(b), for room temperature.

(ii)   Indeed, the $P_{u.T}/P_{y.T}$ values are considerably lower for the P columns in comparison to the F columns. In addition, there is a minute influence of the width ratio b_w/b_f on $P_{u.T}/P_{y.T}$ distribution. Both P and F columns manifested a similar vertical dispersion among the b_w/b_f sets, for low slenderness ($\lambda_{D.T} < 1$) submitted to high temperatures ($T \geq 300$ ºC), and also in the same order: for a given $\lambda_{D.T}$ value, $P_{u.T}/P_{y.T}$ increases as b_w/b_f grows. On the order hand, for moderate-to-high slenderness ($\lambda_{D.T} > 1$), P and F columns demonstrated different behaviors: while the vertical dispersion of $P_{u.T}/P_{y.T}$ values corresponding to P columns seems to be negligible under room and elevated temperatures, it indicates some variation in case of F columns ($P_{u.T}/P_{y.T}$ increases as b_w/b_f decreases, unlike the event detected for $\lambda_{D.T} < 1$).

(iii) As expected, all $P_{u.T}/P_{y.T}$ values concerning P and F columns at elevated temperatures ($T>100$ºC) are below those concerning these columns at moderate temperatures ($T \leq 100$ºC). Moreover, the "size" (maximum $\lambda_{D.T}$ value) of the $P_{u.T}/P_{y.T}$ vs. $\lambda_{D.T}$ plot well defined plateaus varies with the temperature and end support conditions. The above plateaus are followed by descending curve branches that, unexpectedly, are not ordered in the "logical" temperature

47

sequence – indeed, the curves are ordered in the sequence *T=20/100-200-300-800-500-400-600-700* ℃. This order stems directly from the model prescribed in EC3-1.2 [24] to describe the temperature dependence of the CFS constitutive model. In particular, the reduction factor ratio k_p/k_y does not decrease monotonically with the temperature – k_p/k_y=1-0.907-0.786-0.646-<u>0.679</u>-0.6-0.577-<u>0.714</u> for *T=20/100-200-300-400-500-600-700-800* ℃ (the "out of order" values are underlined).

(iv)   The above results provide promising indications about the possibility of developing an efficient (safe and reliable) DSM approach to estimate the distortional failure loads of P and F columns subjected to elevated temperatures. Nevertheless, such results also show very clearly that the distortional failure load predictions for columns at room and elevated temperatures must be handled separately in all over the slenderness range (at least when adopting the EC3-1.2 temperature dependence model) – the DSM design of P and F columns failing in distortional modes at elevated temperatures is addressed next.
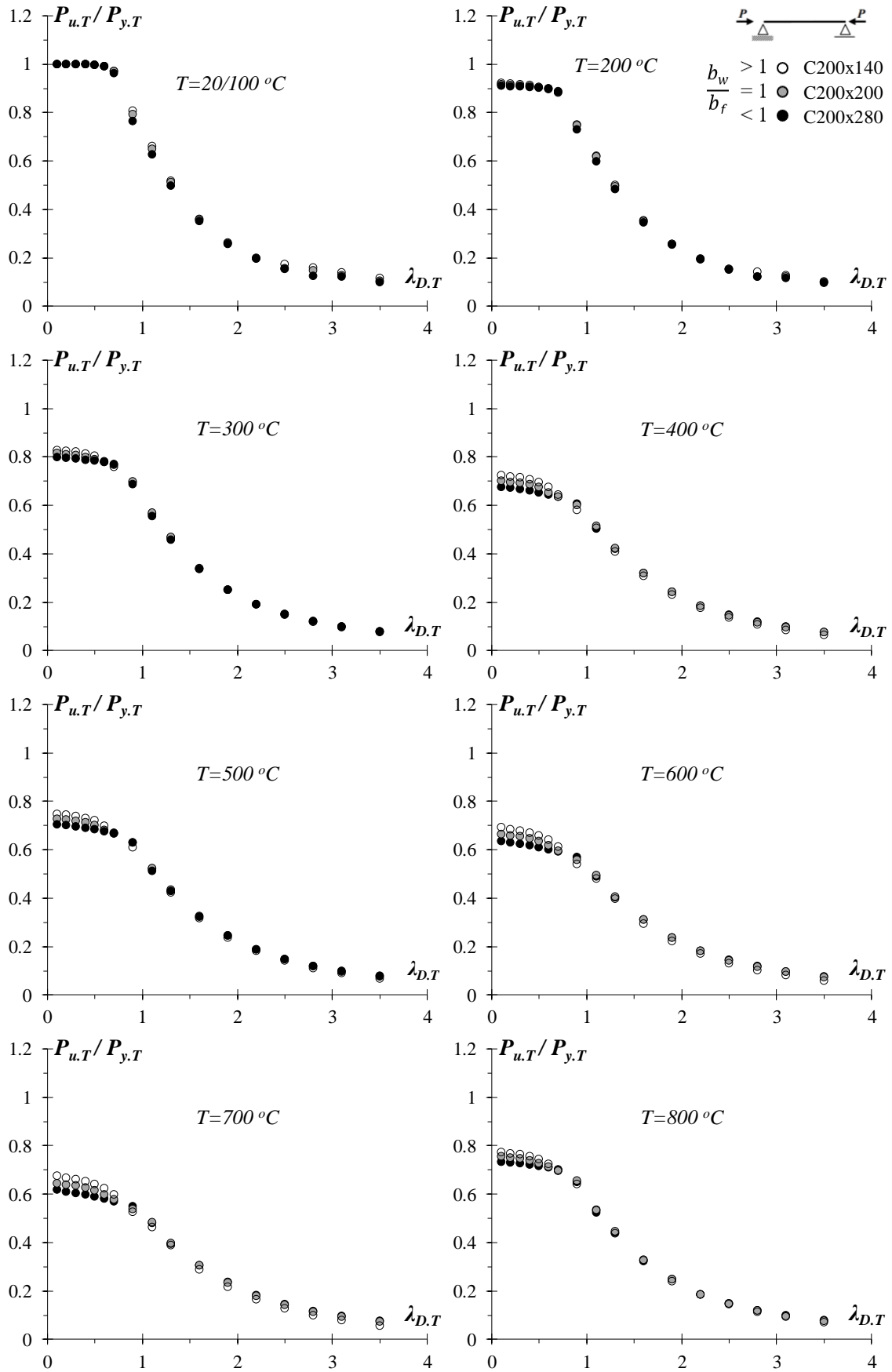
Figure 5.7: Numerical $P_{u.T}/P_{y.T}$ values plotted against $\lambda_{D.T}$, for P columns, under $T=20/100\text{-}200\text{-}300\text{-}400\text{-}500\text{-}600\text{-}700\text{-}800$ °C.
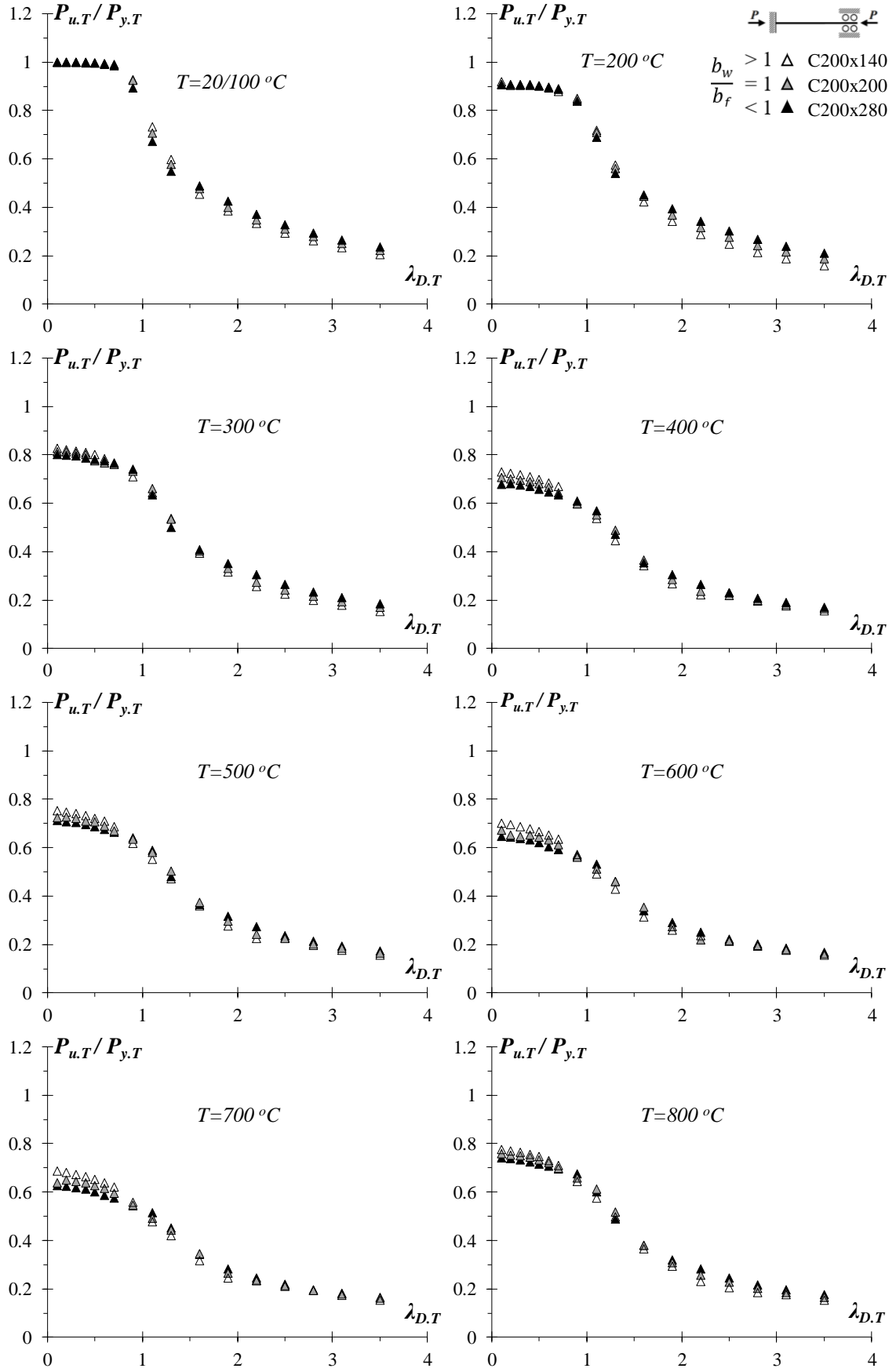
Figure 5.8: Numerical $P_{u.T}/P_{y.T}$ values plotted against $\lambda_{D.T}$, for F columns, under
$T=20/100\text{-}200\text{-}300\text{-}400\text{-}500\text{-}600\text{-}700\text{-}800$ °C.

6 DSM - Design Considerations

This chapter addresses the adequacy of the available Direct Strength Method (DSM) distortional design curve (AISI [5]) to predict the ultimate strength of the CFS lipped channel columns analyzed numerically in this work, concerning conditions of room and elevated temperatures. In particular, it is intended to assess how the quality of the DSM ultimate load estimates is affected by the temperature dependence.

6.1   DSM design – room/moderate temperature

The nominal ultimate load of CFS columns failing in distortional modes ($P_{n.D.20}$), according to the currently codified DSM design curve [5], as already presented in Section 2.3.3, is given again by the expression below (just to visually facilitate the approach of such theme at this point of the thesis):

$$P_{n.D.20} = \begin{cases} P_{y.20} & \text{for } \lambda_{D.20} \leq 0.561 \\ P_{y.20}\left[1 - 0.25\left(\dfrac{P_{cr.D.20}}{P_{y.20}}\right)^{0.6}\right]\left(\dfrac{P_{cr.D.20}}{P_{y.20}}\right)^{0.6} & \text{for } \lambda_{D.20} > 0.561 \end{cases} \qquad \text{(Eq. 6.1)}$$

where (*i*) $P_{cr.D.20}$ and $P_{y.20}$ are the column distortional critical buckling and squash loads, respectively, and (*ii*) $\lambda_{D.20} = (P_{y.20}/P_{cr.D.20})^{0.5}$ is the column distortional slenderness.

Figures 6.1 (a)-(b) compare the above design curve with the numerical and distortional column failure load ratios displayed in Figures 5.6 (a)-(b). In the sequence, Figures 6.2 (a)-(b) show the ratios $P_{u.20}/P_{n.D.20}$ against $\lambda_{D.20}$; such normalized values plotted with respect to the slenderness axis provide better view in other to assess the accuracy and safety of the currently codified DSM distortional strength curve. Thus, the analysis of these figures induces the next comments:

(i)   Naturally, the DSM design curve provides accurate and mostly safe predictions of the F column experimental distortional failure loads reported by SCHAFER [4][29], since they were part of those used in its development and calibration – this assertion can be confirmed by looking at the corresponding $P_{u.20}/P_{n.D.20}$ values in Figure 6.2 (b) (their average, standard deviation, maximum and minimum values are *1.03-0.13-1.32-0.61*, respectively).
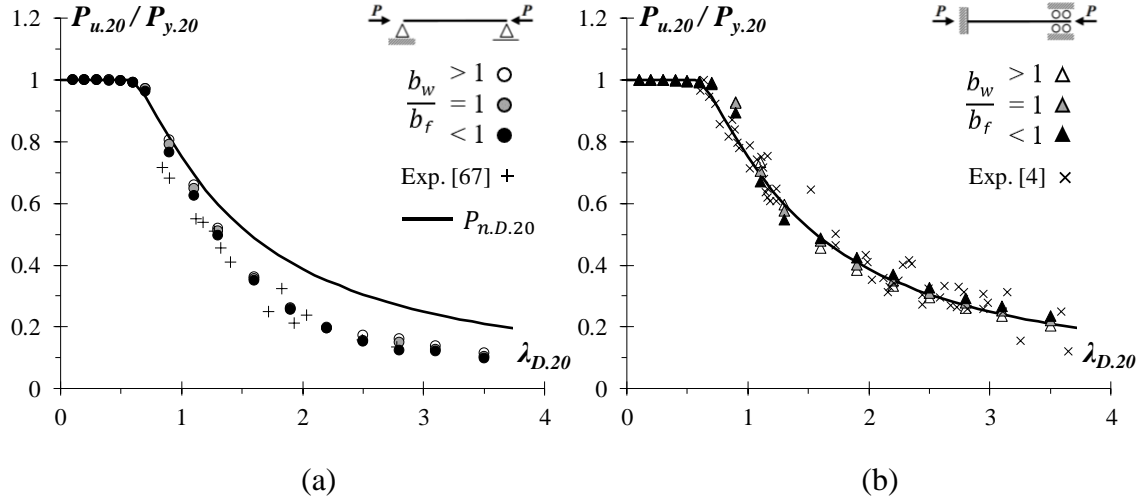
Figure 6.1: Comparison of the (a) P and (b) F column failure load ratios $P_{u.20}/P_{y.20}$ with their predictions, according to the currently codified DSM distortional design curve.
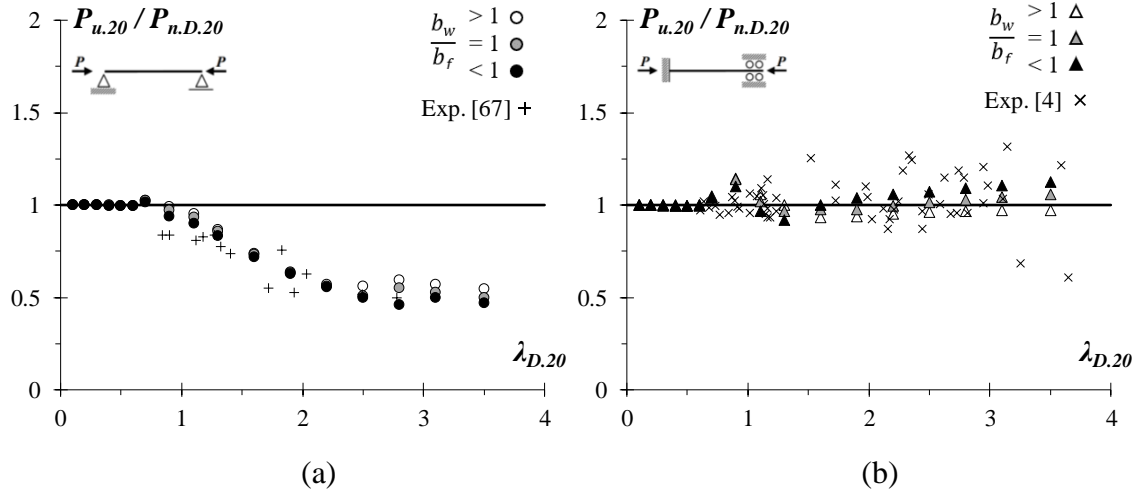
Figure 6.2: Plots $P_{u.20}/P_{n.D.20}$ vs. $\lambda_{D.20}$ for (a) P and (b) F column experimental and numerical failure loads.

(ii) Concerning the F column numerical failure loads obtained in this work (under room/moderate temperature), it is observed that their DSM estimates indicate a reasonable accuracy as well, although they become discreetly less precise as $\lambda_{D.20}$ increases − the $P_{u.20}/P_{n.D.20}$ statistical indicators read *1.01-0.05-1.14-0.92*.

(iii) Concerning the P numerical failure loads, it is observed that, for non-stocky columns ($\lambda_{D.20}>1$), they are overestimated by the DSM design curve − the $P_{u.20}/P_{n.D.20}$ average, standard deviation, maximum and minimum values are *0.81-0.21-1.03-0.46*, respectively. Accurate predictions only occur for stocky columns ($\lambda_{D.20}<1$). Similar findings [35] exposed significant differences between

52

the F and P column distortional post-critical strengths and indicated that such estimates for columns at room and elevated temperatures must be handled separately. Moreover, based on the failure load data gathered [35], an alternative DSM design curve was preliminarily proposed for P columns, as represented by the following expressions:

$$P_{n.D.20(P)} = \begin{cases} P_{y.20} & \text{for } \lambda_{D.20} \leq 0.561 \\[2em] P_{y.20}\left[1-0.25\left(\dfrac{P_{cr.D.20}}{P_{y.20}}\right)^{0.6}\right]\left(\dfrac{P_{cr.D.20}}{P_{y.20}}\right)^{0.6} & \text{for } 0.561 < \lambda_{D.20} \leq 1.133 \qquad \text{(Eq. 6.2)} \\[2em] P_{y.20}\left[0.65+0.2\left(\dfrac{P_{cr.D.20}}{P_{y.20}}\right)^{0.75}\right]\left(\dfrac{P_{cr.D.20}}{P_{y.20}}\right)^{0.75} & \text{for } \lambda_{D.20} > 1.133 \end{cases}$$

They only differ from the current design curve for $\lambda_{D.20} > 1.133$. Figure 6.3 (a) makes it possible to compare the two design curves (solid and dashed lines) between themselves and with the P column experimental and numerical failure loads − the $P_{u.20}/P_{n.D.20(P)}$ values are plotted against $\lambda_{D.20}$ in Figure 6.3 (b). One readily observes that the prediction quality of the proposed curve is substantially higher, as attested by the numerical $P_{u.20}/P_{n.D.20(P)}$ average, standard deviation, maximum and minimum values: *0.98-0.05-1.10-0.84*.
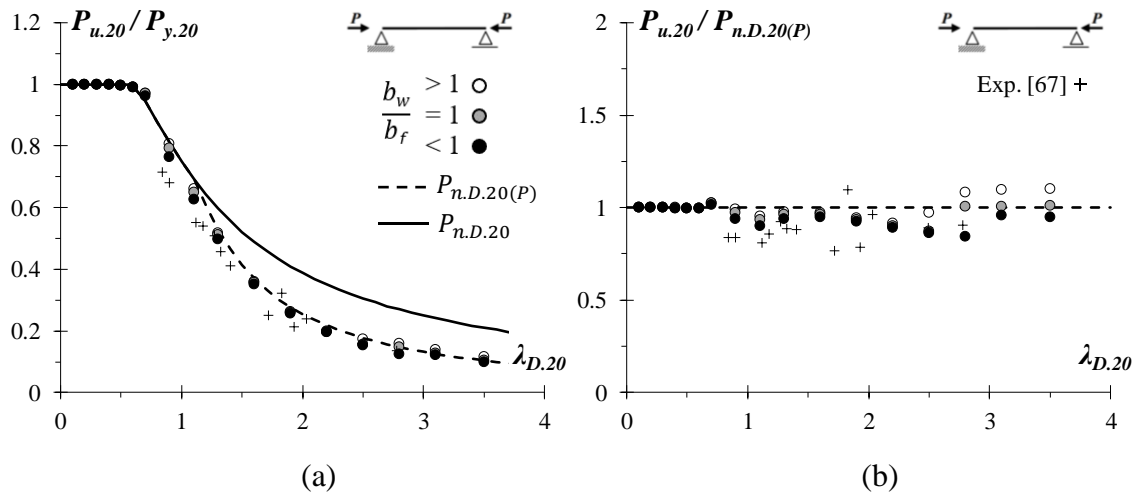
Figure 6.3: Comparison of the (a) currently codified and preliminary DSM distortional design curves with the P column failure load ratios $P_{u.20}/P_{y.20}$ and (b) the corresponding $P_{u.20}/P_{n.D.20(P)}$ values plotted against $\lambda_{D.20}$.

(iv)   In view of the above results, it is decided to adopt in this work the currently codified (related to $P_{n.D.20}$) and preliminarily proposed (related to $P_{n.D.20(P)}$) DSM design/strength curves to predict the F and P column failure loads at room/moderate temperature.

6.2 DSM design – elevated temperatures

As just mentioned, this section addresses the DSM-based prediction of the column failure loads admitting distortional collapses and elevated temperatures. The failure load data gathered and presented in Section 5.5 are used to evaluate and discuss such method, as well as analyzing how the quality of the ultimate load estimates is affected by the temperature dependence.

It is worth emphasizing that the DSM (*i*) has been continuously improved, mostly due to Schafer's efforts [4] and (*ii*) has already been included in the current versions of the North American [5], Australian/New Zealand [6] and Brazilian [7] specifications for CFS structures, but always for room temperature only. Naturally, following an approach already explored by other researchers [17][20][22][56][57][68], the strength curves, already presented in Section 6.1, are modified to reflect the temperature effects by incorporating the temperature dependence of the critical distortional buckling and squash loads, according to the constitutive model prescribed in EC3-1.2 [24]. In this context, the nominal ultimate loads of CFS columns failing in distortional modes at elevated temperatures are given by the expressions below, for P and F columns, respectively:

$$P_{n.D.T(P)} = \begin{cases} P_{y.T} & \text{for } \lambda_{D.T} \leq 0.561 \\ P_{y.T}\left[1-0.25\left(\dfrac{P_{cr.D.T}}{P_{y.T}}\right)^{0.6}\right]\left(\dfrac{P_{cr.D.T}}{P_{y.T}}\right)^{0.6} & \text{for } 0.561 < \lambda_{D.T} \leq 1.133 \\ P_{y.T}\left[0.65+0.2\left(\dfrac{P_{cr.D.T}}{P_{y.T}}\right)^{0.75}\right]\left(\dfrac{P_{cr.D.T}}{P_{y.T}}\right)^{0.75} & \text{for } \lambda_{D.T} > 1.133 \end{cases} \quad \text{(Eq. 6.3)}$$

$$P_{n.D.T(F)} = \begin{cases} P_{y.T} & \text{for } \lambda_{D.T} \leq 0.561 \\ P_{y.T}\left[1-0.25\left(\dfrac{P_{cr.D.T}}{P_{y.T}}\right)^{0.6}\right]\left(\dfrac{P_{cr.D.T}}{P_{y.T}}\right)^{0.6} & \text{for } \lambda_{D.T} > 0.561 \end{cases} \quad \text{(Eq. 6.4)}$$

where (*i*) $P_{cr.D.T}$ and $P_{y.T}$ are the column distortional critical buckling and yield loads, and (*ii*) the column distortional slenderness is defined by $\lambda_{D.T}=(P_{y.T}/P_{cr.D.T})^{0.5}$.

This dependence is felt through the Young's modulus and yield stress values, which are progressively eroded as the temperature (caused by fire conditions) increases. In other words, $P_{cr.D.20}$ and $P_{y.20}$ (or $\sigma_{y.20}$), defined in Eqs. 6.1 and 6.2, are replaced by $P_{cr.D.T}$ and $P_{y.T}$ (or $\sigma_{y.T}$) in Eqs. 6.3 and 6.4 – note that this approach automatically implies that $\lambda_{D.T}$ also varies with *T*.

The graphics shown in Figures 6.4 (P columns) and 6.5 (F columns) make it possible to compare the $P_{u.T}/P_{y.T}$ values with the available DSM distortional strength curves, including temperature effects (dashed and solid black lines, respectively for P and F columns), for temperatures $T=20/100\text{-}200\text{-}300\text{-}400\text{-}500\text{-}600\text{-}700\text{-}800\,°C$. Moreover, Tables A1 to A16, included in Annex A, supply the failure load ratios $P_{u.T}/P_{n.D.T(P)}$ and $P_{u.T}/P_{n.D.T(F)}$. As for Figures 6.6 and 6.7, they provide $P_{u.T}/P_{n.D.T(P)}$ and $P_{u.T}/P_{n.D.T(F)}$ vs. $\lambda_{D.T}$ plots that enable a quick assessment of the quality (accuracy and safety) of the DSM strength curve predictions (the $P_{u.T}/P_{n.D.T(P)}$ and $P_{u.T}/P_{n.D.T(F)}$ averages, standard deviations, maximum and minimum values are also given). The observation of the results, concerning columns at elevated temperatures, conduces to the following remarks:

(i)   The predictions provided by the available DSM strength curves for the failure loads of columns subjected to elevated temperatures are reasonably accurate only for room/moderate temperature. When it comes to high temperatures, they become clearly unsafe. Such effect is remarkably expressed, through the overestimated failure loads, in cases of low slenderness ($\lambda_{D.T}\leq 1$) and continues as $\lambda_{D.T}$ values increase, regardless of the temperature (*i.e.*, for $T\geq 200\,°C$). The $P_{u.T}/P_{n.D.T(P)}$ and $P_{u.T}/P_{n.D.T(F)}$ values confirm the above assertions: their averages and standard deviations vary from: *0.69* to *0.91* and *0.03* to *0.08* (for P columns) and *0.68* to *0.92* and *0.05* to *0.13* (for F columns), considering $T\geq 200\,°C$. In contrast, for room/moderate temperature conditions, such averages and standard deviations are *0.98* and *0.05* (for P columns) and *1.01* and *0.05* (for F columns).

(ii)   The vast majority of distortional failure loads of columns with low-to-moderate slenderness values, at elevated temperatures, are overestimated by the available DSM design curves. This amount of overestimation, which is more pronounced for $T\geq 300\,°C$, seems to be influenced by the b_w/b_f width ratio in both P and F columns. For a given $\lambda_{D.T}$ value, $P_{u.T}/P_{y.T}$ increases as b_w/b_f grows. On the other hand, in the moderate-to-high slenderness range, $P_{u.T}/P_{y.T}$ increases as b_w/b_f decreases.

(iii)   In view of the findings presented in the above items, it is clear that the available DSM strength curves are unable to predict adequately distortional failure loads, at elevated temperatures, of columns with low-to-moderate slenderness range (notably) and also with high slenderness values – indeed, most of such failure loads are heavily overestimated. Therefore, it is necessary to modify the above DSM strength curves in order to improve the quality of the failure load prediction.
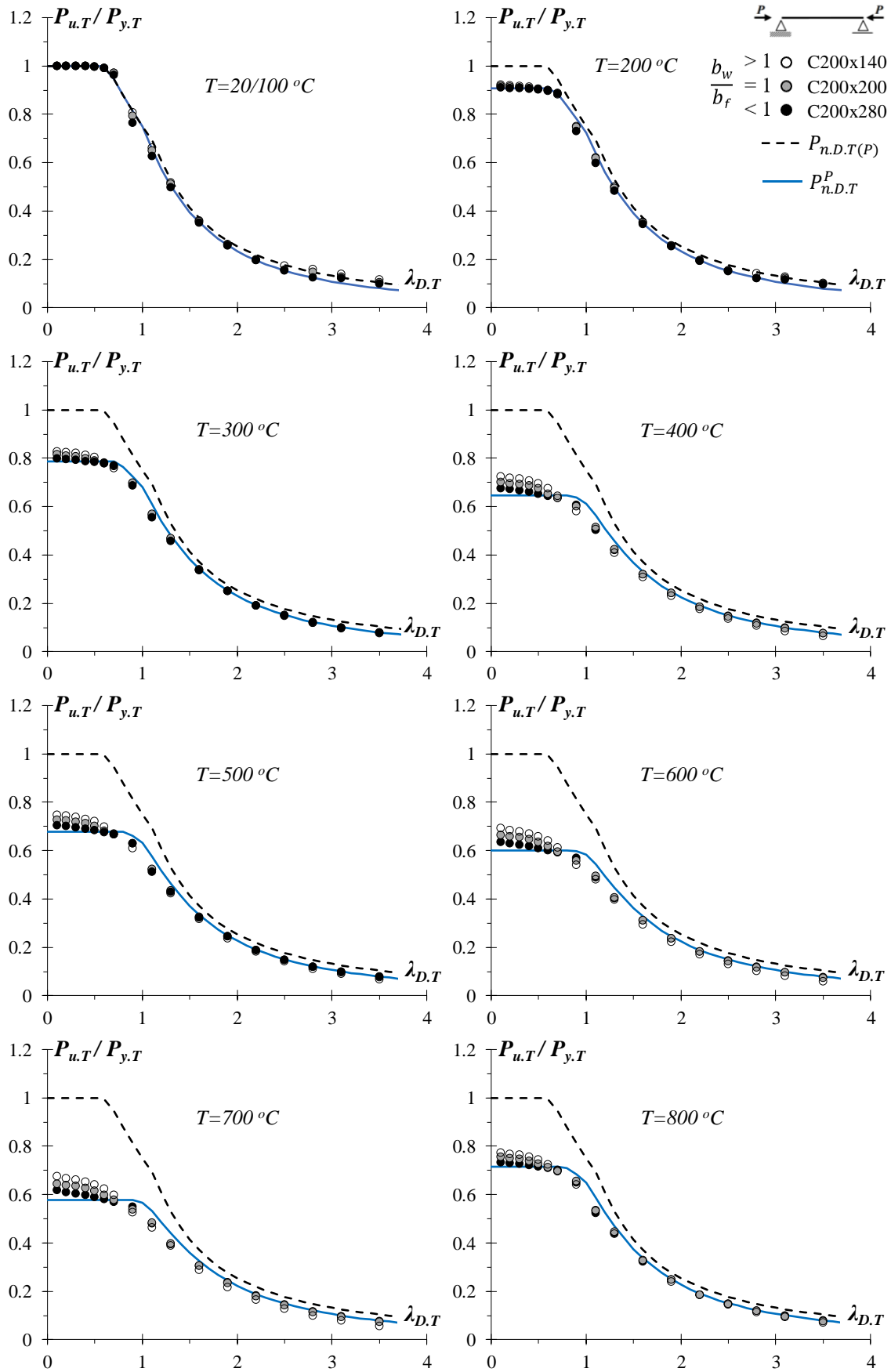
Figure 6.4: Comparison of the P column failure load ratios with the available and modified DSM distortional design curves (T=20/100-200-300-400-500-600-700-800 ºC).
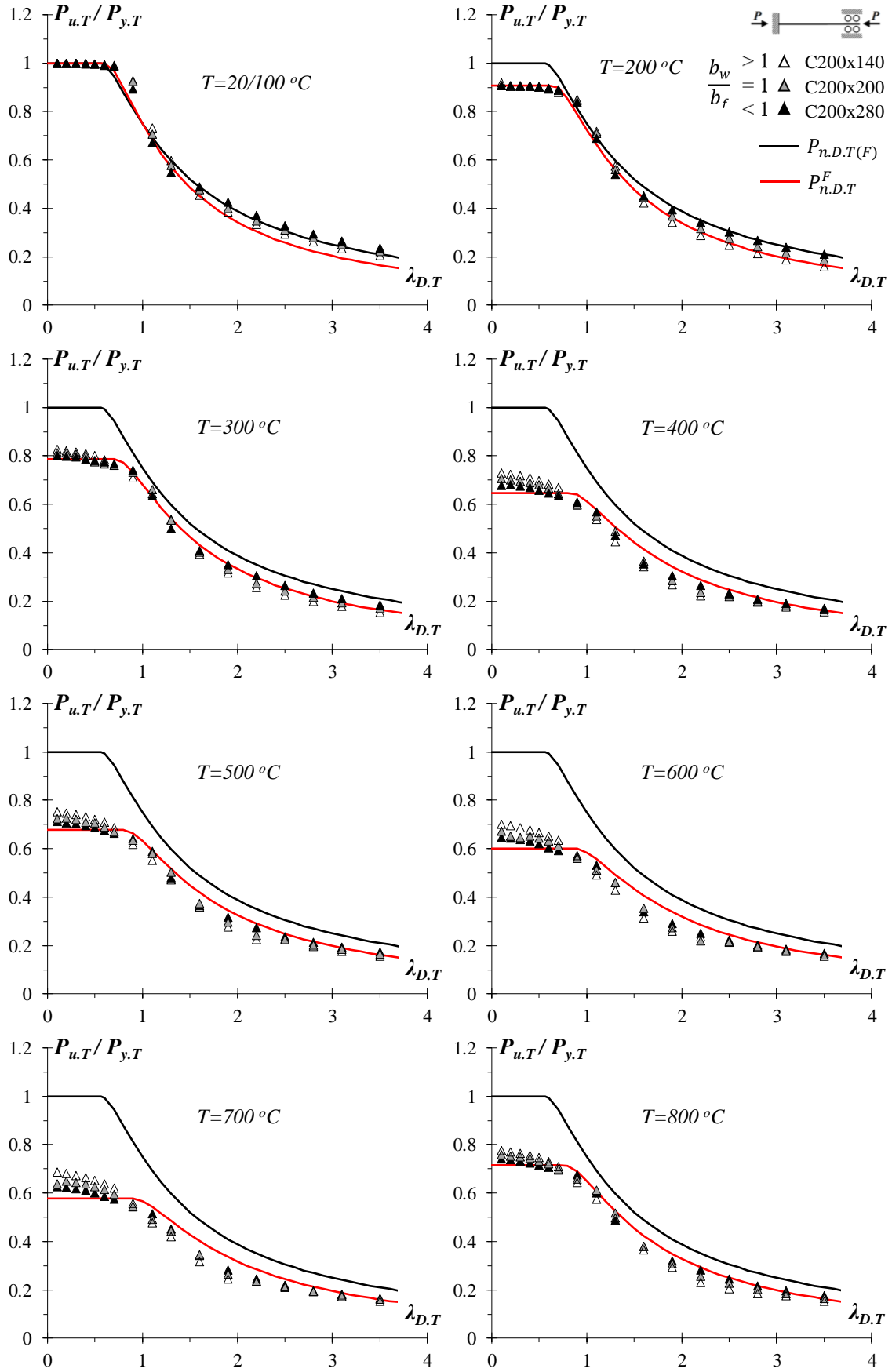
Figure 6.5: Comparison of the F column failure load ratios with the available and modified DSM distortional design curves (*T=20/100-200-300-400-500-600-700-800* ºC).
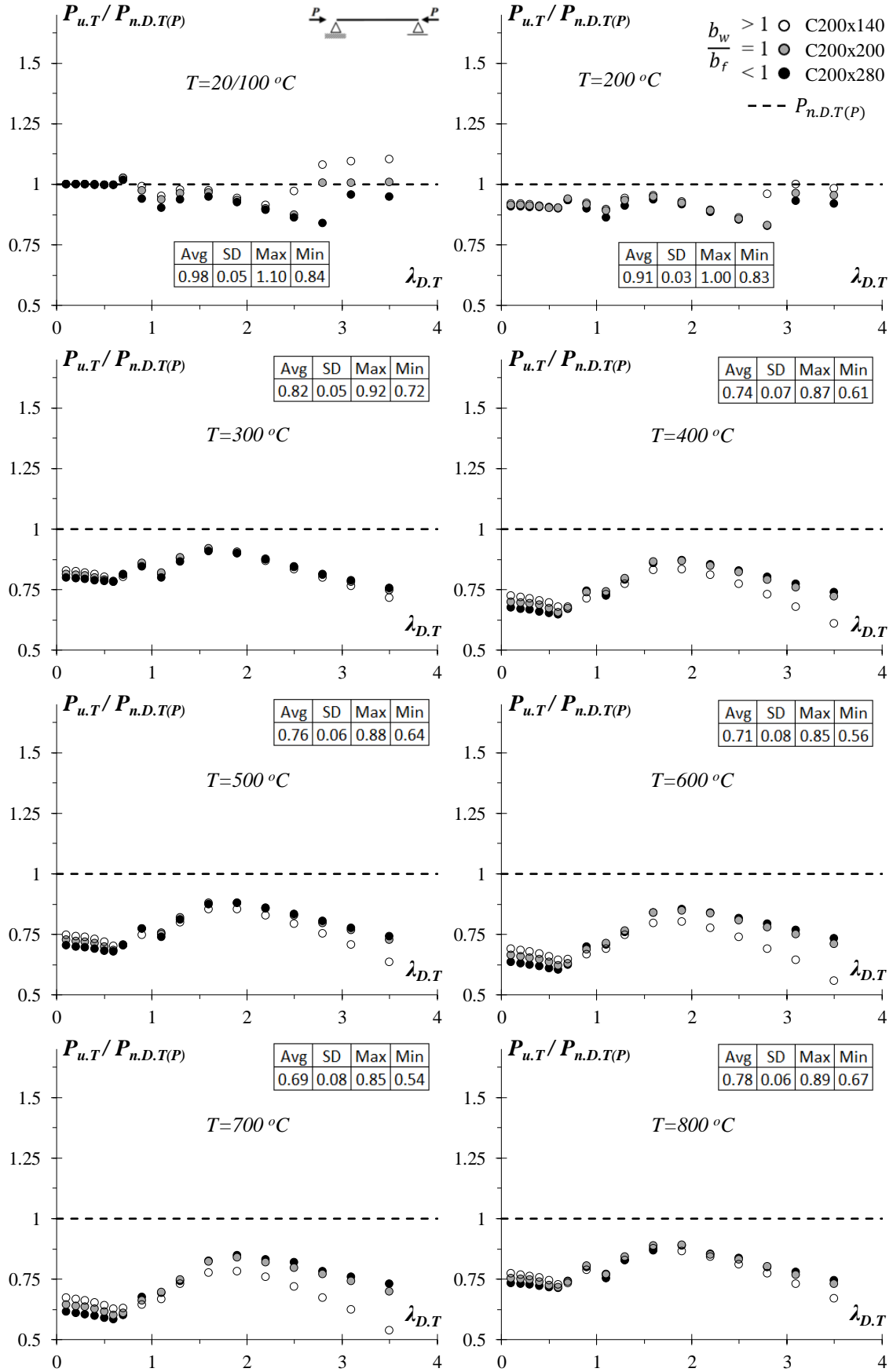
Figure 6.6: $P_{u.T}/P_{n.D.T(P)}$ vs. $\lambda_{D.T}$ plots of the P columns, concerning temperatures

$T=20/100\text{-}200\text{-}300\text{-}400\text{-}500\text{-}600\text{-}700\text{-}800$ ºC.
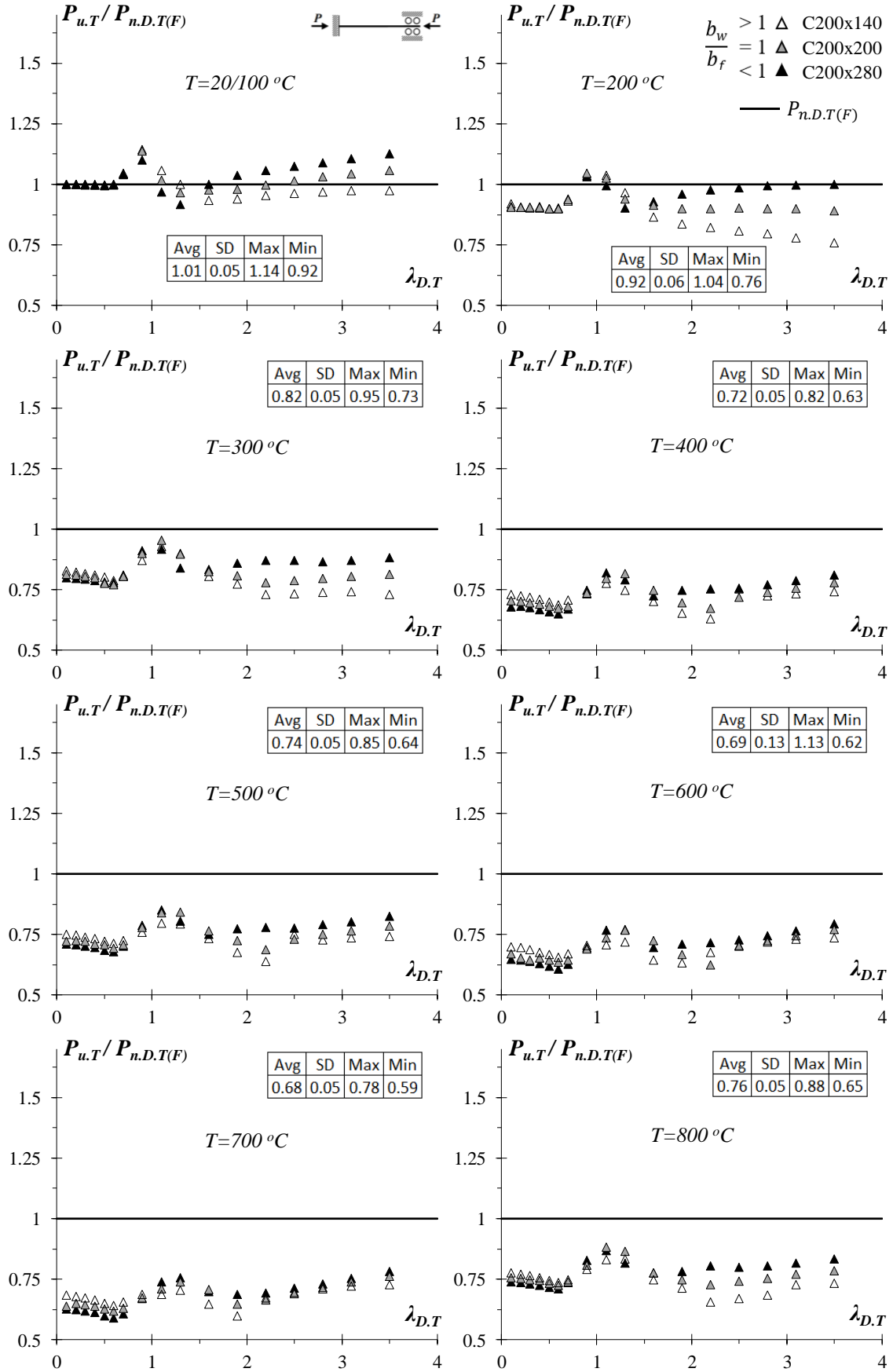
Figure 6.7: $P_{u.T}/P_{n.D.T(F)}$ vs. $\lambda_{D.T}$ plots of the F columns, concerning temperatures $T=20/100\text{-}200\text{-}300\text{-}400\text{-}500\text{-}600\text{-}700\text{-}800\ ^oC$.

59

6.3 Modified DSM design – room/moderate and elevated temperatures

On the basis of the numerical failure load results obtained in this work, the challenge now is to find modified DSM design curves able to provide adequate (safe and reliable) predictions for the ultimate strength of P and F columns collapsing in distortional modes at elevated temperatures ($T>100$ °C). The main idea behind this attempt is the incorporation of the reduction factor ratio k_p/k_y (shown earlier to play a key role in the steel constitutive model temperature dependence prescribed by the EC3-1.2 [24] (as approached in Sections 4.3 and 5.5) into the expressions defining the DSM-based strength curves. In this context, "trial-and-error" curve fitting procedures were carried out and their outputs are the modified DSM strength curves defined by the following expressions, for P and F columns, respectively:

$$P_{n.D.T}^{P} = \begin{cases} P_{y.20} \cdot k_p & \text{for } \lambda_{D.T} \leq \eta \\[2em] P_{y.T}\left[1-\dfrac{0.25}{\left(\dfrac{k_p}{k_y}\right)}\left(\dfrac{P_{cr.D.T}}{P_{y.T}}\right)^{0.6}\right]\left(\dfrac{P_{cr.D.T}}{P_{y.T}}\right)^{0.6} & \text{for } \eta<\lambda_{D.T} \leq 1 \\[2em] P_{y.T}\left[1-\dfrac{0.25}{\left(\dfrac{k_p}{k_y}\right)}\left(\dfrac{P_{cr.D.T}}{P_{y.T}}\right)\right]\left(\dfrac{P_{cr.D.T}}{P_{y.T}}\right) & \text{for } \lambda_{D.T} >1 \end{cases}$$

(Eq. 6.5)

$$\text{with} \quad \eta = 0.9284\left(\frac{k_p}{k_y}\right)^2 - 2.2244\left(\frac{k_p}{k_y}\right)+1.8570$$

$$P_{n.D.T}^{F} = \begin{cases} P_{y.20} \cdot k_p & \text{for } \lambda_{D.T} \leq \dfrac{0.561}{\left(\dfrac{k_p}{k_y}\right)} \\[2em] P_{y.T}\left[1-\dfrac{0.25}{\left(\dfrac{k_p}{k_y}\right)}\left(\dfrac{P_{cr.D.T}}{P_{y.T}}\right)^{0.7}\right]\left(\dfrac{P_{cr.D.T}}{P_{y.T}}\right)^{0.7} & \text{for } \lambda_{D.T} > \dfrac{0.561}{\left(\dfrac{k_p}{k_y}\right)} \end{cases}$$

(Eq. 6.6)

These design equations differ from the available ones (Eqs. 6.3 and 6.4) in the fact that (*i*) the squash load $P_{y.T}$ is replaced by $P_{y.20} \cdot k_p$ ($k_p=\sigma_{p.T}/\sigma_{y.20}$ defines the proportional limit stress $\sigma_{p.T}$), (*ii*) the distortional slenderness transition value *0.561* is replaced by $\eta=$ *0.9284 (k_p/k_y)² - 2.2244 (k_p/k_y) + 1.8570* (for P columns) and *0.561 /(k_p/k_y)* (for F columns), (*iii*) the coefficient *0.25* is replaced by *0.25/(k_p/k_y)*, (*iv*) the P-column expressions valid for intermediate and slender column now differ only in the exponents (*0.6* vs. *1.0*), thus leading to a distortional slenderness transition value equal to *1.0* (instead of *1.133*) and (*v*) the F-column expressions differ in the exponents (*0.6* vs. *0.7*).

The DSM-based distortional design curves provided by Eqs. 6.5 and 6.6 (for P and F columns) are displayed in Figures 6.8 (a)-(b), respectively. From the observation of these design curves, it is readily concluded that:

(i) The design curves concerning conditions of room/moderate temperature exhibit minute changes for both P and F columns.

(ii) Although the design curves for P and F columns at elevated temperatures are modified, these modifications are much more significant for slenderness values below around *1.5*. Therefore, the failure load predictions concerning slender ($\lambda_{D.T} \geq 1.5$) P and F columns received only a slight adjustment.

(iii) Since the modification of the available design curves consists essentially of incorporating k_p/k_y into the column squash load and distortional slenderness transition values, it is just logical to expect that the temperature dependence of this ratio will be directly reflected in the design curve variation with the temperature. Indeed, this is the case: as clearly illustrated in Figures 6.8 (a)-(b), for both P and F columns, the modified design curves are ordered like the k_p/k_y values, *i.e.*, in the sequence *T=20/100-200-300-800-500-400-600-700°C*.
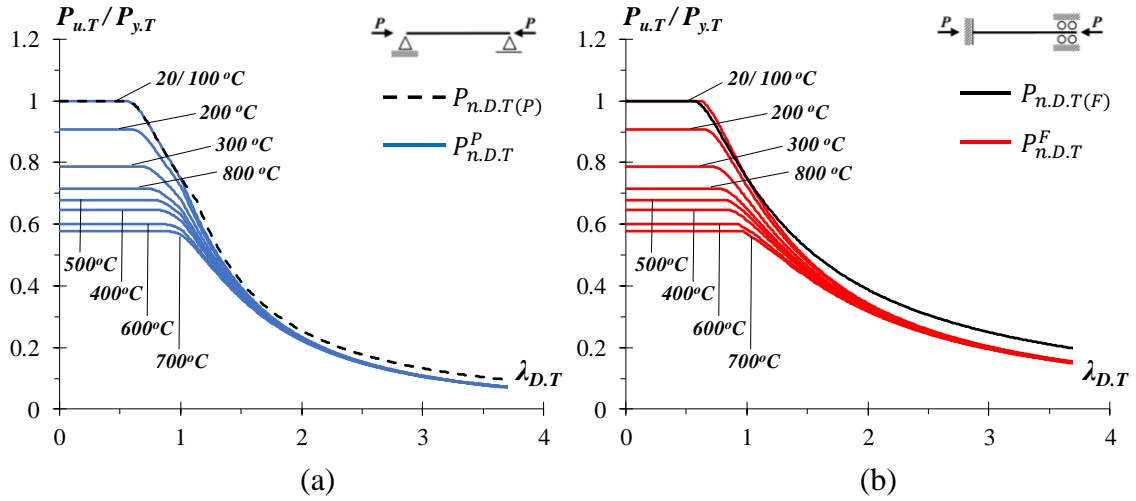
Figure 6.8: Comparison between the available and modified DSM distortional design curves for (a) P and (b) F columns at temperatures *T=20/100-200-300-400-500-600-700-800 °C*.

In order to assess the quality of the failure load predictions provided by the modified DSM-based design curves, Figures 6.9 and 6.10 plot the $P_{u.T}/P_{n.D.T}^P$ and $P_{u.T}/P_{n.D.T}^F$ values against $\lambda_{D.T}$ and include also the associated statistical indicators (averages, standard deviations, maximum and minimum values), that enable a quick quantitative assessment of the accuracy and safety of the new curves. The corresponding $P_{u.T}/P_{n.D.T}^P$ and $P_{u.T}/P_{n.D.T}^F$ are

given in Tables A1 to A16 (for P and F columns, at room and elevated temperatures), presented in Annex A. The observation and analysis of the results (failure load predictions) exhibited in these figures and tables prompt the following conclusions:

(i)   Despite the simplicity of the modifications, the failure load estimates yielded by the modified proposed DSM distortional strength curves, for P and F columns at elevated temperatures, outperform those provided by their available counterparts.

(ii)   Concerning the P columns, the $P_{u.T}/P^P_{n.D.T}$ statistical indicators are reasonably good for all the temperatures considered. Indeed, especially when $T{\geq}200\,°$C the average varies between *0.98* and *1.02*, the standard deviation varies between *0.03* and *0.10*, the maximum value varies between *1.05* and *1.28*, and the minimum value varies between *0.71* and *0.94*. Although the amount of insecure predictions has reduced and the remaining overestimated values are much closer to the new/modified curves, it should be noted that the numbers of unsafe estimates are still considerably high, most of them concerning columns of intermediate-to-high slenderness. Further studies are required in order to develop and propose a DSM-based design curve that ensures a better quality of the P-column failure load prediction – obviously, the new features to be included in such design curve must focus on the intermediate-to-high slenderness range.

(iii)   Concerning the F columns, the $P_{u.T}/P^F_{n.D.T}$ statistical indicators are again fairly similar and good for all the temperatures considered. Indeed, the variations of the average, standard deviation and maximum/minimum value are now from *0.97* to *1.03*, *0.05* to *0.12*, *1.09* to *1.27* and *0.73* to *0.95*, respectively. Just like for the P columns, the numbers of unsafe predictions are reasonably high, for columns of intermediate slenderness in this case.

(iv)   The good performance of the above modifications, in the sense that they improve visibly the quality of the failure load prediction (comparing to the old/previous estimates), provides encouragement to proceed with this approach in the search for an efficient (safe and reliable) DSM-based design methodology for columns failing in distortional modes at elevated temperatures. It is worth noting that, given the scarcity of column experimental distortional failure load data at elevated temperatures, there is an important need to develop experimental tests involving lipped channel (and also other cross-section shapes) columns at both room and elevated temperatures.

62
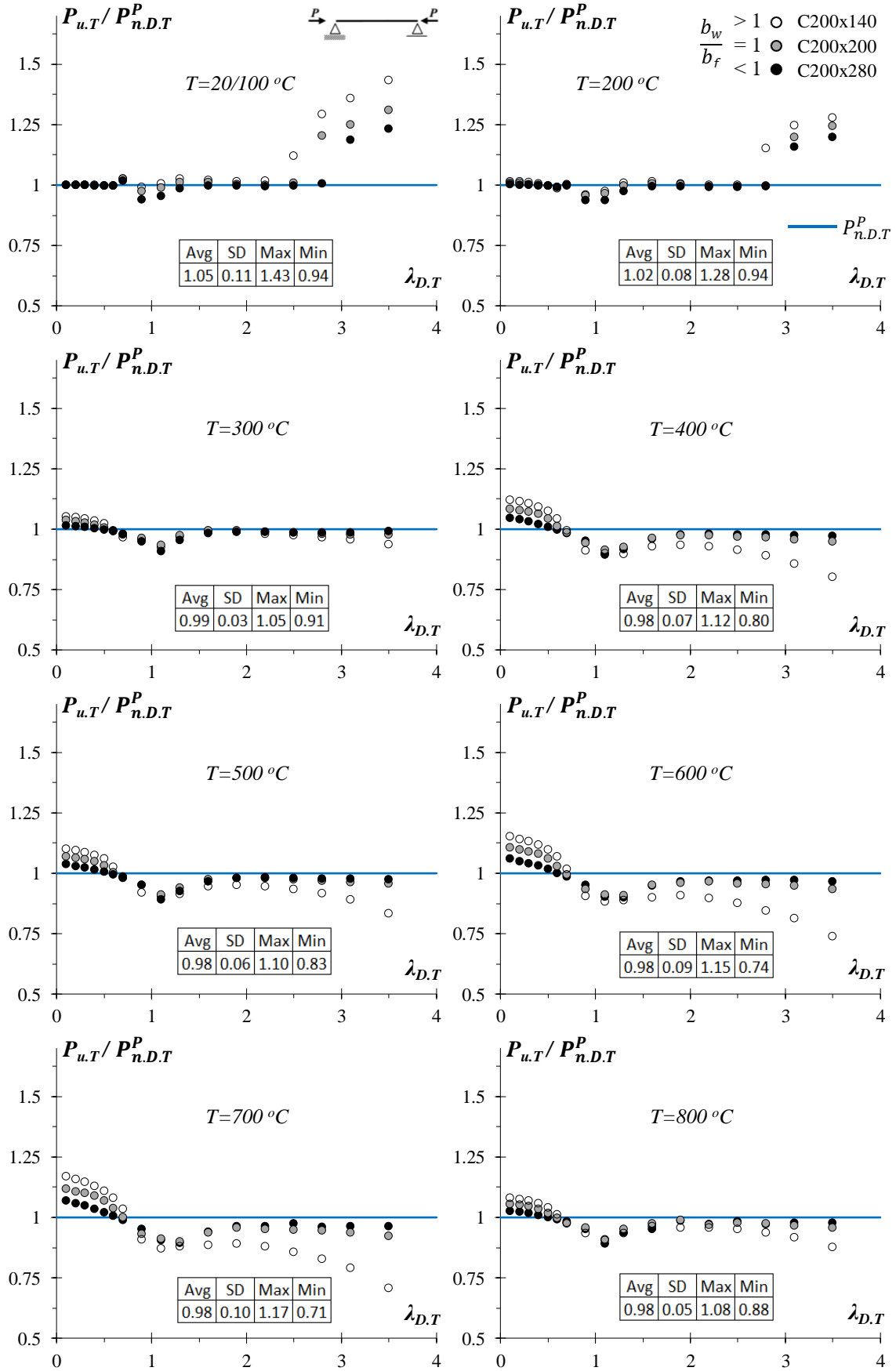
Figure 6.9: $P_{u.T}/P^P_{n.D.T}$ ratios plotted against the distortional slenderness $\lambda_{D.T}$ concerning P columns at temperatures $T=20/100$-200-300-400-500-600-700-800 °C.
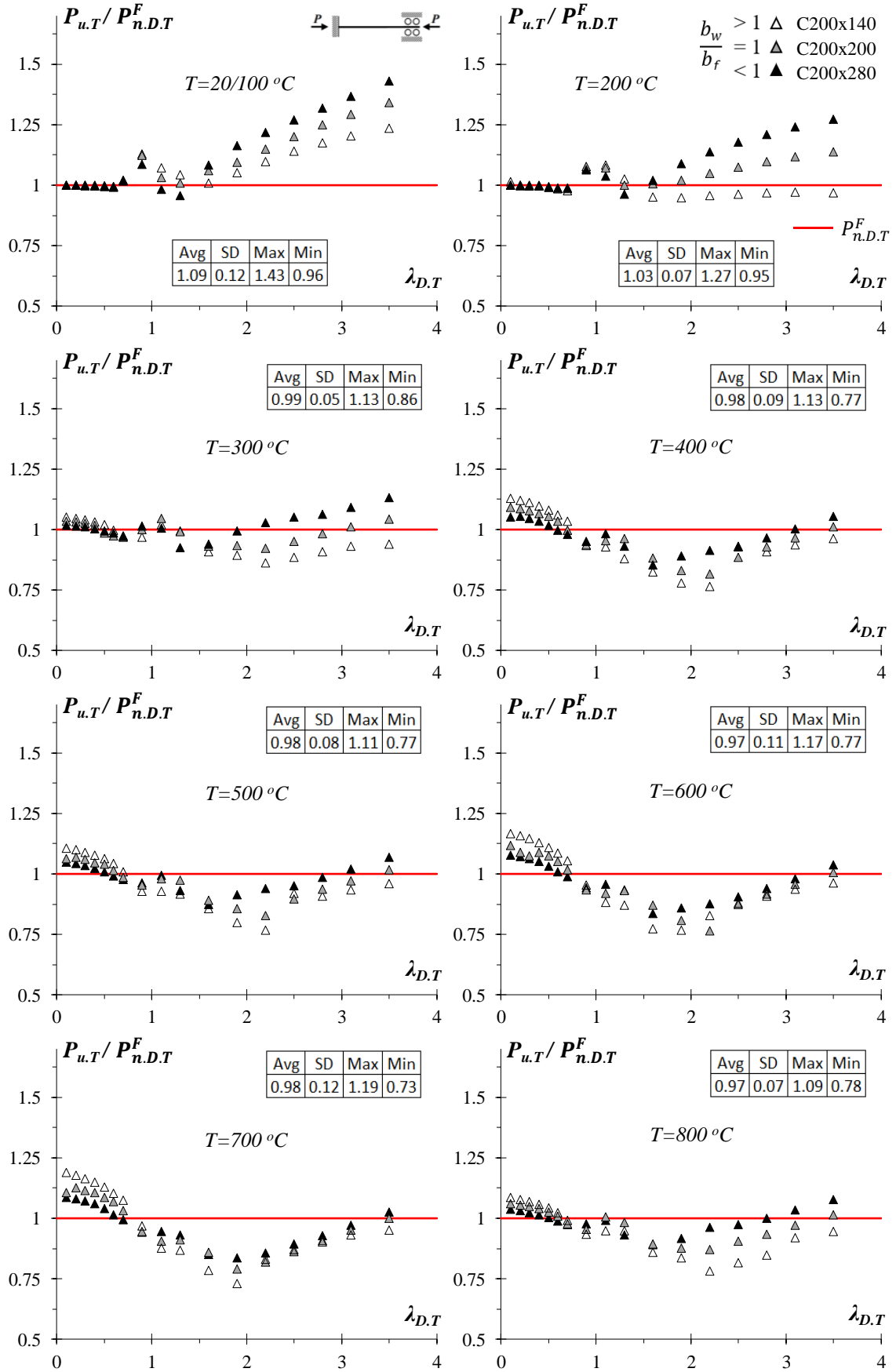
Figure 6.10: $P_{u.T}/P_{n.D.T}^F$ ratios plotted against the distortional slenderness $\lambda_{D.T}$ concerning F columns at temperatures $T=20/100$-200-300-400-500-600-700-800 ^oC.

7 Conclusions

This research work presented an extensive numerical investigation, developed by means of ANSYS shell FEA, that involved lipped channels CFS columns failing in distortional modes and submitted to different uniform elevated temperatures. Among the main findings, some topics were extensively discussed such as the elastic-plastic post-buckling behavior and ultimate strength of the selected columns. All the CFS members were analyzed concerning the constitutive relationship prescribed by EC3-1.2 [24] for high temperature conditions. The corresponding results were used to assess the influence of the constitutive model temperature dependence on the quality of ultimate load predictions, provided by the current DSM distortional design curves.

In this context, the numerical analyses considered a total of *816* lipped channel CFS columns that exhibit (*i*) *3* column geometries, namely C200x140, C200x200 and C200x280, with lengths selected to ensure pure distortional buckling and failure modes, (*ii*) *2* end support conditions (F and P), (*iii*) temperature-dependent material properties as prescribed by the EC3-1.2 model for CFS, (*iv*) *17* room temperature yield stresses, chosen to cover wide distortional slenderness ranges ($\lambda_{D.T}$ varying from *0.1* to *3.5*) and (*v*) *8* uniform temperatures (up to *800 °C*).

The sets of elastic and elastic-plastic distortional post-buckling equilibrium paths, under room/moderate and elevated temperatures, were displayed in order to acquire in-depth knowledge about the influence of the (*i*) end support conditions, (*ii*) cross-section dimensions and (*iii*) temperature level on the distortional structural response and load-carrying capacity of CFS columns.

Finally, the distortional failure loads obtained were evaluated and used to propose modified/improved DSM distortional curves, with the aim of contributing towards the development of a more efficient (accurate and safe) DSM-based design approach, for columns failing in distortional modes at elevated temperatures.

Out of the various findings reported throughout the thesis, the following ones deserve to be specially mentioned:

(*i*) Regardless of the temperature, the $P_{u.T}/P_{y.T}$ vs. $\lambda_{D.T}$ "clouds" follow the trend of "Winter-type" strength curves and exhibit a small amount of "vertical dispersion" (more visible in the F columns). Moreover, the $P_{u.T}/P_{y.T}$ values are

much smaller in the P columns than in their F counterparts, due to the considerably lower post-critical strength of the former – this justifies the need for two different DSM distortional design curves. Finally, there is a visible influence of the width ratio b_w/b_f on the $P_{u.T}/P_{y.T}$ values (for both P and F columns), particularly in the low slenderness range for high temperatures. On the order hand, concerning the moderate-to-high slenderness, such influence is smoothed and indicates the opposite order of variation.

(ii) As expected, all the $P_{u.T}/P_{y.T}$ values concerning P and F columns at elevated temperatures ($T > 100$ ºC) are below those concerning these columns at room/moderate temperatures ($T \leq 100$ ºC). Moreover, the "size" (maximum $\lambda_{D.T}$ value) of the $P_{u.T}/P_{y.T}$ vs. $\lambda_{D.T}$ plot well defined plateaus varies with the temperature and end support conditions. Those plateaus are followed by descending curve branches that are ordered in the sequence *T=20/100-200-300-800-500-400-600-700 ºC*, which is the same of the temperature-dependent reduction factor ratio k_p/k_y associated with the model prescribed in EC3-1.2 [24] to quantify the variation of the steel constitutive model with the temperature.

(iii) The available DSM design curves, developed in the context of P and F columns failing in distortional modes at room temperature, were employed to predict failure loads at elevated temperatures. These estimates concern critical distortional buckling and squash loads calculated with the (temperature-dependent) reduced Young's modulus and yield stress values prescribed in EC3-1.2 [24]. It was found that such failure load predictions are mostly unsafe for both P and F columns along practically all the slenderness range, thus meaning that some modification was required.

(iv) A modification of the current DSM distortional design curves, which involved the incorporation of the reduction factor ratio k_p/k_y (reduction factors prescribed in EC3-1.2 [24]), was proposed. It led to a set of temperature-dependent "lowered" strength curves that differ from the available ones, mainly and more expressively, for slenderness values below around *2.0*. In spite of the inherent simplicity of the above modification, the ensuing DSM distortional design curves were shown to improve visibly the quality of the failure load prediction. The amount of insecure predictions has reduced and the remaining overestimated values are much closer to the new/modified strength curves. These findings encourage

to proceed with this approach in the pursuit of an efficient DSM-based design methodology for columns failing in distortional modes at elevated temperatures.

7.1 Suggestions for future work

Experimental tests often result in important and advanced contributions for the knowledge of CFS structures submitted to fire conditions. In this context, an experimental investigation directed to assess the elastic-plastic post-buckling behavior and to obtain the ultimate strength of CFS columns under compression load at both room and elevated temperatures should be planned. The results of the testing campaign would allow to compare the numerical values presented in this work with their corresponding experimental analyses.

In addition, concerning different cross-section shapes of CFS columns, namely hat-sections, zed-sections and rack-sections, is also an interesting scope that provides covering a wide range of structural cases with varied technical features. The appraisal of such diverse responses obtained through numerical and experimental analyses can lead to generate new distortional strength curves, considering the DSM design and high temperatures.

As attested throughout this work, the temperature dependence of the constitutive model adopted has a significant effect on the mechanical properties and induces the CFS structures to lose strength and stiffness under increasing temperatures. Thus, there is a need for further studies focused on concerning and evaluating different constitutive models, namely stress-strain-temperature curves, and different steel grades. These mechanical properties can also be used to compose coupon tests (CFS columns with different cross-section shapes and dimensions) in order to conduct numerical and experimental buckling (and post-buckling) analyses at fire conditions.

Although the focus of the present research is on capacity, another relevant topic is related to the thermal properties that govern heat transfer and thermal deformations. This research area is still less studied than mechanical properties by the structural engineering community. Future works should include material testing to assess the thermal conductivity and to determine thermal expansion coefficients of CFS members subjected to elevated temperatures. It is worth noting that understanding how such magnitudes influence the material behavior and, consequently, the structure performance is essential for the development of a more complete study, aiming to achieve as close as possible real conditions for structural analyses.

8 Bibliography

[1]   SANTIAGO, A. K., FREITAS, A. M. S., CRASTO, R. C. M., 2012, *Steel Framing: Arquitetura, Manual de Construção em Aço*. Rio de Janeiro, Instituto Aço Brasil - Centro Brasileiro da Construção em Aço.

[2]   IMN - Industrial Machinery News. http://industrial-machinery-news.com/. Accessed on January 26, 2018.

[3]   MECALUX - Soluções de Armazenagem. https://www.mecalux.com.br/cargas-paletizadas/porta-pallets. Accessed on January 26, 2018.

[4]   SCHAFER, B.W., 2008, "Review: the Direct Strength Method of cold-formed steel member design", *Journal of Constructional Steel Research*, 64(7-8), pp. 766-788.

[5]   AISI - American Iron and Steel Institute, *North American Specification for the Design of Cold-Formed Steel Structural Members* – NAS: AISI-S100-16, Washington (DC), 2016.

[6]   AS/NZS - Standards of Australia and Standards of New Zealand (SA-SNZ), *Australian/New Zealand Standard on Cold-Formed Steel Structures*, AS/NZS 4600. 2nd ed., Sydney-Wellington, 2005.

[7]   ABNT NBR 14762 - Brazilian Standards Association - *Brazilian Standard on Design of Cold-Formed Steel Structures*, NBR 14762:2010, Rio de Janeiro-RJ, 2010 (Portuguese).

[8]   DON ALLEN, P.E.; "History of Cold Formed Steel". *Structure Magazine*, Archives.   http://www.structuremag.org/wp-content/uploads/2014/09/C-BB-History-AllenLowndes-Nov061.pdf. Accessed on February 03, 2018.

[9]   VARGAS, M.R.; SILVA, V.P., 2005, *Resistência ao Fogo das Estruturas de Aço, Manual de Construção em Aço*. Rio de Janeiro, Instituto Brasileiro de Siderurgia – Centro Brasileiro da Construção em Aço.

[10]   GSU – Georgia State University, University Library. Digital Collections. http://digitalcollections.library.gsu.edu/cdm/singleitem/collection/ajc/id/342/rec/13. Accessed on February 03, 2018.

[11]   CSSBI – Canadian Sheet Steel Building Institute. Lightweight Steel Framing, Photo Gallery. http://cssbi.ca/products/steel-building-systems. Accessed on February 03, 2018.

[12] LEE, J.H., MAHENDRAN, M., MAKELAINEN, P., 2003, "Prediction of mechanical properties of light gauge steels at elevated temperatures", *Journal of Constructional Steel Research*, n. 59 (Jun), pp. 1517-1532.

[13] CHEN, J., YOUNG, B., 2007, "Cold-formed steel lipped channel columns at elevated temperatures", *Engineering Structures*, 29(10), 2445-56.

[14] RANAWAKA, T., MAHENDRAN, M., 2009, "Experimental study of the mechanical properties of light gauge cold-formed steels at elevated temperatures", *Fire Safety Journal*, 44(2), 219–29.

[15] LANDESMANN, A., SILVA, F.C.M., BATISTA, E. M., 2014, "Experimental investigation of the mechanical properties of ZAR-345 cold-formed steel at elevated temperatures", *Materials Research*, n. 17 (Jul), pp. 1082-1091.

[16] WEI, C., JIHONG, Y., 2012, "Mechanical properties of G550 cold-formed steel under transient and steady state conditions", *Journal of Constructional Steel Research*, n. 73 (Jun), pp. 1-11.

[17] LANDESMANN, A., CAMOTIM, D., SILVA, F.C.M., 2018, "DSM design of cold-formed steel columns failing in distortional modes at elevated temperatures" *International Journal of Steel Structures*, v.19(3), pp. 1023-1041.

[18] FENG, M., WANG, Y.C., DAVIES, J.M., 2003, "Structural behavior of cold-formed thin-walled short steel channel columns at elevated temperatures − Part 1: Experiments", *Thin-Walled Structures*, 41(6), 543-70.

[19] FENG, M., WANG, Y.C., DAVIES, J.M., 2003, "Structural behavior of cold-formed thin-walled short steel channel columns at elevated temperatures − Part 2: Design calculations and numerical analysis", *Thin-Walled Structures*, 41(6), 571-94.

[20] RANAWAKA, T., MAHENDRAN, M., 2009, "Distortional buckling tests of cold-formed steel compression members at elevated temperatures", *Journal of Constructional Steel Research*, 65(2), 249-59.

[21] RANAWAKA, T., MAHENDRAN, M., 2010, "Numerical modelling of light gauge cold-formed steel compression members subjected to distortional buckling at elevated temperatures", *Thin-Walled Structures*, 48(3-4), 334-44.

[22] LANDESMANN, A., CAMOTIM, D., 2011, "On the distortional buckling, post-buckling and strength of cold-formed steel lipped channel columns under fire conditions", *Journal of Structural Fire Engineering*, 2(1), 1-19.

[23] SHAHBAZIAN, A., WANG, Y.C., 2012, "Direct Strength Method for calculating distortional buckling capacity of cold-formed thin-walled steel columns with

uniform and non-uniform elevated temperatures", *Thin-Walled Structures*, 53(April), 188-199.

[24] EN 1993-1.2 - Eurocode 3 - *Design of steel structures - Part 1-2: General rules - Structural fire design*, CEN - European Committee for Standardization. Brussels, 2005.

[25] BUCHANAN, A.H., 2002, Structural Design for Fire Safety. JOHN WILEY & SONS, LTD, England.

[26] REIS, A., CAMOTIM, D., 2001. *Structural Stability*. McGraw-Hill. (Portuguese)

[27] ZIEMIAN, R.D., 2010, *Guide to Stability Design Criteria for Metal Structures*, 6th Edition, John Wiley & Sons, New York.

[28] HANCOCK, G.J., 2003, "Cold-formed steel structures", *Journal of Constructional Steel Research*, v.59, pp.473-487.

[29] SCHAFER, B.W., 2000, "Distortional Buckling of Cold-Formed Steel Columns", *The American Iron and Steel Institute (AISI) Final Report*.

[30] BEBIANO, R., PINA, P., SILVESTRE, N., CAMOTIM, D., 2008, GBTUL - "A code for the buckling analysis of cold-formed steel members", In: *Proceedings of 19th International Specialty Conference on Recent Research and Developments in Cold-Formed Steel Design and Construction* (St. Louis, 14-15/10), R LaBoube, WW Yu (eds.), 61-79.

[31] BEBIANO, R., PINA, P., SILVESTRE, N., CAMOTIM, D., 2008, *GBTUL 1.0β – Buckling and Vibration Analysis of Thin-Walled Members*, DECivil/IST, Technical University of Lisbon, Portugal. (http://www.civil.ist.utl.pt/gbt)

[32] SCHAFER, B.W., 2002, "Local, Distortional, and Euler buckling of thin-walled columns", *Journal of Structural Engineering*, v.128(3), pp. 289-299.

[33] ÁDÁNY, S., SILVESTRE, N., SCHAFER, B.W., CAMOTIM, D., 2009, "GBT and cFSM: two modal approaches to the buckling analysis of unbranched thin-walled members", *Advanced Steel Construction*, vol. 5, n. 2, pp. 195-223.

[34] SILVESTRE, N., CAMOTIM, D., 2004, "Local-plate and distortional post-buckling behavior of cold-formed steel lipped channel columns with intermediate stiffeners", *Seventeenth International Specialty Conference on Cold-Formed Steel Structures* (Orlando, 04-05/11), 1-18.

[35] LANDESMANN, A., CAMOTIM, D., 2013, "On the Direct Strength Method (DSM) design of cold-formed steel columns against distortional failure", *Thin-walled Structures*, v.67, pp. 168-187.

[36] HANCOCK, G.J., MURRAY, T.M., ELLIFRITT, D.S., 2001, *Cold-formed Steel Structures to the AISI Specification*, Marcel Dekker, New York.

[37] HANCOCK, G.J., KWON, Y.B., BERNARD, E.S., 1994, "Strength design curves for thin-walled sections undergoing distortional buckling", *Journal Construction*, v.31, pp. 169-186.

[38] BATISTA, E.M., 2010, "Effective section method: A general direct method for the design of steel cold-formed members under local–global buckling interaction", *Thin-Walled Structures*, v.48, pp. 345-356.

[39] SCHAFER, B.W., PEKÖZ, T., 1998, "Direct strength prediction of cold-formed steel members using numerical elastic buckling solutions", *Proceedings of 14th International Specialty Conference on Cold-formed Steel Structures* (St. Louis, 15-16/10), pp. 69-76.

[40] PFEIL, W., PFEIL, M., 2009, Estruturas de Aço - Dimensionamento Prático de Acordo com a NBR 8800:2008. 8a edição. Rio de Janeiro, Editora LTC.

[41] SIDEY, M.P., TEAGUE, D.P., 1988, *Elevated temperature data for structural grades of galvanised steel*. In: British Steel Report, Welsh Laboratories, UK.

[42] KANKANAMGE, N.D., MAHENDRAN, M., 2011, "Mechanical properties of cold-formed steels at elevated temperatures", *Thin-Walled Structures*, n. 49 (Set), pp. 26-44.

[43] CHEN, J., YOUNG B., 2007, "Experimental investigation of cold-formed steel material at elevated temperatures", *Thin-Walled Structures*, 45(1), 96-110.

[44] RAMBERG, W., OSGOOD, W. R., 1943, *Description of stress-strain curves by three parameters*. In: National Advisory Committee for Aeronautics (NACA), Technical Note 902, Washington.

[45] KIRBY, B.R., PRESTON, R.R., 1988, "High temperatures properties of hot-rolled structural steels for use in fire engineering design studies", *Fire Safety Journal*, n. 13, pp. 27-37.

[46] OUTINEN, J., KAITILA, O., MAKELÄINEN, P., 2000, "A study for the development of the design of steel structures in fire conditions", *Proceedings of First International Workshop on Structures in Fire* (SiF'2000 – Copenhagen, 19-20/6), J.M. Franssen (ed.), 267-281.

[47] KAITILA, O., "Imperfection sensitivity analysis of lipped channel columns at high temperatures", *Journal of Constructional Steel Research*, 58(3), 333-51.

[48] FENG, M., WANG, Y.C., DAVIES, J.M., 2003, "Thermal performance of cold-formed thin-walled steel panel systems in fire", *Fire Safety Journal*, 38(4), 365-94.

[49] FENG, M., WANG, Y.C., DAVIES, J.M., 2003, "Axial strength of cold-formed thin-walled steel channels under non-uniform temperatures in fire", *Fire Safety Journal*, 38(8), 679-707, 2003.

[50] FENG, M., WANG, Y.C., DAVIES, J.M., 2004, "A numerical imperfection sensitivity study of cold-formed thin-walled tubular steel columns at uniform elevated temperatures", *Thin-Walled Structures*, 42(4), 533-55.

[51] FENG, M., WANG, Y.C., 2005, "An analysis of the structural behaviour of axially loaded full-scale cold-formed thin-walled steel structural panels tested under fire conditions", *Thin-Walled Structures*, 43(2), 291-332.

[52] FENG, M., WANG, Y.C., 2005, "An experimental study of loaded full-scale cold-formed thin-walled steel structural panels under fire conditions, *Fire Safety Journal*, 40(1), 43-63.

[53] CHEN, J., YOUNG B., 2006, "Corner properties of cold-formed steel sections at elevated temperatures", *Thin-Walled Structures*, 44(2), 216-23.

[54] CHEN, J., YOUNG, B., 2008, "Design of high strength steel columns at elevated temperatures", *Journal of Constructional Steel Research*, 64(6), 689-703.

[55] RANAWAKA, T., 2006, *Distortional Buckling Behavior of Cold-Formed Steel Compression Members at Elevated Temperatures*, Ph.D. Thesis in Civil Engineering, Queensland University of Technology, Brisbane, Australia.

[56] LANDESMANN, A., CAMOTIM, D., 2010, "Distortional failure and design of cold-formed steel lipped channel columns under fire conditions", *Proceedings of SSRC Annual Stability Conference* (Orlando, 12-15/5), 505-532.

[57] LANDESMANN, A., CAMOTIM, D., 2011, "Distortional failure and design of cold-formed steel rack-section columns under fire conditions", *Proceedings of Fourth International Conference on Steel & Composite Structures* (ICSCS'2011 – Sydney, 21-23/7), B. Uy et al. (eds.), 287-289. (full paper in Cd-Rom Proceedings)

[58] LANDESMANN, A., CAMOTIM, D., 2012, "DSM design of cold-formed steel columns failing distortionally exposed to fire: how relevant is the temperature dependence of the material behavior?", *USB Proceedings of the SSRC Annual Stability Conference* (Grapevine, 18-21/4).

[59] SHAHBAZIAN, A., WANG, Y.C., 2011, "Calculating the global buckling resistance of thin-walled steel members with uniform and non-uniform elevated temperatures under axial compression", *Thin-Walled Structures*, 49(11), 1415-28.

[60] SHAHBAZIAN, A., WANG, Y.C., 2011, "Application of the Direct Strength Method to local buckling resistance of thin-walled steel members with non-uniform elevated temperatures under axial compression", *Thin-Walled Structures*, 49(12), 1573-83.

[61] ABREU, J.C.B., VIEIRA, L.M.C., ABU-HAMD, M.H., SCHAFER, B.W., 2014, "Review: development of performance-based fire design for cold-formed steel" *Fire Science Reviews*, 3(1), 1-15.

[62] SAS - Swanson Analysis Systems Inc., 2009, *Ansys Reference Manual* (vrs. 12).

[63] ELLOBODY, E., YOUNG, B., 2005, "Behavior of cold-formed steel plain angle columns", *Journal of Structural Engineering*, (ASCE), 131(3), pp. 457-466.

[64] LANDESMANN, A., CAMOTIM, D., BATISTA, E.M., 2009, "On the distortional buckling, post-buckling and strength of cold-formed steel lipped channel columns subjected to elevated temperatures", *Proceedings of International Conference on Applications of Structural Fire Engineering* (Prague), F. Wald, P. Kallerová, J. Chlouba (eds.), A8-A13.

[65] PROLA, L.C., CAMOTIM, D., 2002, "On the distortional post-buckling behavior of cold-formed lipped channel steel columns", *Proceedings of SSRC Annual Stability Conference* (Seattle, 24-27/4), 571-590.

[66] PROLA, L.C., CAMOTIM, D., 2002, "On the distortional post-buckling behavior of rack-section cold-formed steel columns", *Proceedings of Sixth International Conference on Computational Structures Technology* (CST 2002 – Prague, 4-6/9), B. Topping, Z. Bittnar (eds.), Civil-Comp Press (Stirling), 233-234. (full paper in Cd-Rom Proceedings – paper 98).

[67] SANTOS, W.S., 2017, *On the Strength and DSM Design of End-Bolted Cold-Formed Steel Columns Buckling Distortional Modes*, Ph.D. Thesis in Civil Engineering, COPPE–Federal University of Rio de Janeiro, Rio de Janeiro, Brazil.

[68] LANDESMANN, A., CAMOTIM, D., 2012, "Application of direct strength method design to distortional buckling resistance of thin-walled steel columns exposed to fire", In: Topping BHV, editor, *Proceedings of Eleventh International Conference on Computational Structures Technology*, (CST Dubrovnik, 4-7/9).

Annex A

Tables A1 to A16 provide information concerning the pinned-ended and fixed-ended lipped channel columns numerical failure loads and their DSM-based estimates, at room/moderate and elevated temperatures ($T = 20/100^oC$ to 800^oC). Each table deals with the three types of column cross-section dimensions (different web-to-flange width ratios), *i.e.*, C200x140, C200x200 and C200x280, submitted to the temperature value and the two end support conditions considered (P and F). It includes the values of the (*i*) reduction factors k_y, k_E and k_p, (*ii*) distortional slenderness $\lambda_{D.T}$, (*iii*) squash load $P_{y.T}$, (*iv*) numerical failure load $P_{u.T}$, (*v*) ratio $P_{u.T}/P_{y.T}$ and (*vi*) numerical-to-predicted failure load ratios $P_{u.T}/P_{n.D.T(P)}$, $P_{u.T}/P_{n.D.T(F)}$, $P_{u.T}/P_{n.D.T}^P$ (P columns) and $P_{u.T}/P_{n.D.T}^F$ (F columns).

Table A1: Numerical failure loads and their DSM estimates for the pinned lipped channel columns at 100ºC.

Column	k_y	k_E	k_p	$\lambda_{D.T}$	$P_{y.T}$ (kN)	$P_{u.T}$ (kN)	$\dfrac{P_{u.T}}{P_{y.T}}$	$\dfrac{P_{u.T}}{P_{n.D.T(P)}}$	$\dfrac{P_{u.T}}{P_{n.D.T}^P}$
				0.1	1.50	1.50	1.00	1.00	1.00
				0.2	5.99	5.98	1.00	1.00	1.00
				0.3	13.47	13.46	1.00	1.00	1.00
				0.4	23.95	23.91	1.00	1.00	1.00
				0.5	37.43	37.30	1.00	1.00	1.00
				0.6	53.90	53.42	0.99	1.00	1.00
				0.7	73.36	71.19	0.97	1.03	1.03
				0.9	121.27	97.72	0.81	0.99	0.99
C200x140	1.00	1.00	1.00	1.1	181.16	119.50	0.66	0.95	1.01
				1.3	253.02	130.96	0.52	0.98	1.03
				1.6	383.27	137.99	0.36	0.97	1.02
				1.9	540.47	141.26	0.26	0.94	1.01
				2.2	724.62	144.41	0.20	0.91	1.02
				2.5	935.72	176.37	0.19	0.97	1.12
				2.8	1173.77	187.56	0.16	1.08	1.29
				3.1	1438.77	198.17	0.14	1.09	1.36
				3.5	1834.02	210.12	0.11	1.10	1.43
				0.1	0.99	0.99	1.00	1.00	1.00
				0.2	3.97	3.97	1.00	1.00	1.00
				0.3	8.93	8.92	1.00	1.00	1.00
				0.4	15.87	15.85	1.00	1.00	1.00
				0.5	24.80	24.73	1.00	1.00	1.00
				0.6	35.71	35.43	0.99	1.00	1.00
				0.7	48.61	47.14	0.97	1.03	1.03
				0.9	80.36	63.63	0.79	0.97	0.97
C200x200	1.00	1.00	1.00	1.1	120.04	77.86	0.65	0.94	0.99
				1.3	167.66	85.54	0.51	0.96	1.01
				1.6	253.97	90.63	0.36	0.96	1.01
				1.9	358.14	92.64	0.26	0.93	1.00
				2.2	480.17	94.12	0.20	0.90	1.00
				2.5	620.05	95.94	0.15	0.87	1.01
				2.8	777.79	115.51	0.15	1.00	1.20
				3.1	953.39	120.74	0.13	1.01	1.25
				3.5	1215.30	127.38	0.10	1.01	1.31
				0.1	0.66	0.66	1.00	1.00	1.00
				0.2	2.63	2.63	1.00	1.00	1.00
				0.3	5.92	5.91	1.00	1.00	1.00
				0.4	10.52	10.50	1.00	1.00	1.00
				0.5	16.43	16.38	1.00	1.00	1.00
				0.6	23.66	23.47	0.99	1.00	1.00
				0.7	32.20	30.95	0.96	1.02	1.02
				0.9	53.24	40.69	0.76	0.94	0.94
C200x280	1.00	1.00	1.00	1.1	79.53	49.73	0.63	0.90	0.95
				1.3	111.07	55.15	0.50	0.94	0.98
				1.6	168.25	59.11	0.35	0.95	1.00
				1.9	237.26	60.95	0.26	0.93	1.00
				2.2	318.10	61.92	0.19	0.89	0.99
				2.5	410.77	62.83	0.15	0.86	1.00
				2.8	515.27	64.05	0.12	0.84	1.01
				3.1	631.60	76.00	0.12	0.96	1.19
				3.5	805.11	79.38	0.10	0.95	1.23

Table A2: Numerical failure loads and their DSM estimates for the pinned lipped channel columns at 200ºC.

Column	k_y	k_E	k_p	$\lambda_{D.T}$	$P_{y.T}$ (kN)	$P_{u.T}$ (kN)	$\dfrac{P_{u.T}}{P_{y.T}}$	$\dfrac{P_{u.T}}{P_{n.D.T(P)}}$	$\dfrac{P_{u.T}}{P_{n.D.T}^P}$
C200x140	0.89	0.90	0.807	0.1	1.35	1.24	0.92	0.92	1.02
				0.2	5.39	4.95	0.92	0.92	1.01
				0.3	12.13	11.12	0.92	0.92	1.01
				0.4	21.56	19.67	0.91	0.91	1.01
				0.5	33.69	30.49	0.91	0.91	1.00
				0.6	48.51	43.39	0.89	0.90	0.99
				0.7	66.02	58.26	0.88	0.93	1.00
				0.9	109.14	81.81	0.75	0.92	0.96
				1.1	163.04	101.37	0.62	0.90	0.97
				1.3	227.72	113.68	0.50	0.94	1.01
				1.6	344.94	121.80	0.35	0.95	1.01
				1.9	486.43	125.06	0.26	0.93	1.00
				2.2	652.16	127.06	0.19	0.89	1.00
				2.5	842.15	128.73	0.15	0.86	1.00
				2.8	1056.39	156.98	0.15	0.96	1.15
				3.1	1294.89	163.06	0.13	1.00	1.25
				3.5	1650.61	168.49	0.10	0.98	1.28
C200x200	0.89	0.90	0.807	0.1	0.89	0.82	0.92	0.92	1.01
				0.2	3.57	3.26	0.91	0.91	1.01
				0.3	8.04	7.32	0.91	0.91	1.00
				0.4	14.29	12.96	0.91	0.91	1.00
				0.5	22.32	20.17	0.90	0.90	1.00
				0.6	32.14	28.86	0.90	0.90	0.99
				0.7	43.75	38.84	0.89	0.94	1.00
				0.9	72.32	53.94	0.75	0.92	0.96
				1.1	108.04	66.67	0.62	0.89	0.97
				1.3	150.90	74.55	0.49	0.93	1.00
				1.6	228.58	80.21	0.35	0.95	1.01
				1.9	322.33	82.61	0.26	0.92	1.00
				2.2	432.15	83.84	0.19	0.89	1.00
				2.5	558.05	84.83	0.15	0.86	0.99
				2.8	700.01	86.02	0.12	0.83	1.00
				3.1	858.05	103.82	0.12	0.96	1.20
				3.5	1093.77	108.57	0.10	0.96	1.24
C200x280	0.89	0.90	0.807	0.1	0.59	0.54	0.91	0.91	1.00
				0.2	2.37	2.15	0.91	0.91	1.00
				0.3	5.32	4.83	0.91	0.91	1.00
				0.4	9.46	8.57	0.91	0.91	1.00
				0.5	14.79	13.35	0.90	0.90	1.00
				0.6	21.29	19.13	0.90	0.90	0.99
				0.7	28.98	25.64	0.88	0.94	1.00
				0.9	47.91	34.99	0.73	0.90	0.94
				1.1	71.57	42.76	0.60	0.86	0.94
				1.3	99.97	48.21	0.48	0.91	0.97
				1.6	151.43	52.44	0.35	0.94	0.99
				1.9	213.54	54.29	0.25	0.92	0.99
				2.2	286.29	55.28	0.19	0.89	0.99
				2.5	369.69	56.00	0.15	0.85	0.99
				2.8	463.74	56.71	0.12	0.83	0.99
				3.1	568.44	66.57	0.12	0.93	1.16
				3.5	724.60	69.33	0.10	0.92	1.20

Table A3: Numerical failure loads and their DSM estimates for the pinned lipped channel columns at 300ºC.

Column	k_y	k_E	k_p	$\lambda_{D.T}$	$P_{y.T}$ (kN)	$P_{u.T}$ (kN)	$\dfrac{P_{u.T}}{P_{y.T}}$	$\dfrac{P_{u.T}}{P_{n.D.T(P)}}$	$\dfrac{P_{u.T}}{P_{n.D.T}^{P}}$
C200x140	0.78	0.80	0.613	0.1	1.20	0.99	0.83	0.83	1.05
				0.2	4.79	3.95	0.82	0.82	1.05
				0.3	10.78	8.84	0.82	0.82	1.04
				0.4	19.16	15.59	0.81	0.81	1.04
				0.5	29.94	24.05	0.80	0.80	1.02
				0.6	43.12	33.66	0.78	0.79	0.99
				0.7	58.69	44.57	0.76	0.80	0.97
				0.9	97.02	67.39	0.69	0.85	0.96
				1.1	144.92	81.81	0.56	0.81	0.93
				1.3	202.42	94.14	0.47	0.88	0.97
				1.6	306.62	103.54	0.34	0.91	0.99
				1.9	432.38	107.82	0.25	0.90	0.99
				2.2	579.70	109.75	0.19	0.87	0.98
				2.5	748.58	110.67	0.15	0.83	0.97
				2.8	939.02	110.95	0.12	0.80	0.97
				3.1	1151.01	110.69	0.10	0.76	0.96
				3.5	1467.21	109.38	0.07	0.72	0.94
C200x200	0.78	0.80	0.613	0.1	0.79	0.65	0.81	0.81	1.04
				0.2	3.17	2.57	0.81	0.81	1.03
				0.3	7.14	5.76	0.81	0.81	1.03
				0.4	12.70	10.15	0.80	0.80	1.02
				0.5	19.84	15.67	0.79	0.79	1.00
				0.6	28.57	22.25	0.78	0.78	0.99
				0.7	38.89	29.83	0.77	0.81	0.98
				0.9	64.29	44.88	0.70	0.86	0.96
				1.1	96.03	54.56	0.57	0.82	0.93
				1.3	134.13	62.74	0.47	0.88	0.97
				1.6	203.18	69.05	0.34	0.92	0.99
				1.9	286.51	71.99	0.25	0.91	0.99
				2.2	384.13	73.39	0.19	0.88	0.99
				2.5	496.04	74.15	0.15	0.84	0.98
				2.8	622.23	74.70	0.12	0.81	0.98
				3.1	762.71	75.09	0.10	0.78	0.98
				3.5	972.24	75.45	0.08	0.75	0.98
C200x280	0.78	0.80	0.613	0.1	0.53	0.42	0.80	0.80	1.02
				0.2	2.10	1.67	0.80	0.80	1.01
				0.3	4.73	3.75	0.79	0.79	1.01
				0.4	8.41	6.63	0.79	0.79	1.00
				0.5	13.14	10.30	0.78	0.78	1.00
				0.6	18.93	14.74	0.78	0.78	0.99
				0.7	25.76	19.86	0.77	0.81	0.98
				0.9	42.59	29.25	0.69	0.84	0.95
				1.1	63.62	35.21	0.55	0.80	0.91
				1.3	88.86	40.71	0.46	0.87	0.95
				1.6	134.60	45.24	0.34	0.91	0.98
				1.9	189.81	47.38	0.25	0.90	0.99
				2.2	254.48	48.51	0.19	0.87	0.99
				2.5	328.62	49.15	0.15	0.84	0.98
				2.8	412.22	49.66	0.12	0.81	0.98
				3.1	505.28	50.09	0.10	0.79	0.99
				3.5	644.09	50.72	0.08	0.76	0.99

Table A4: Numerical failure loads and their DSM estimates for the pinned lipped channel columns at 400°C.

Column	k_y	k_E	k_p	$\lambda_{D.T}$	$P_{y.T}$ (kN)	$P_{u.T}$ (kN)	$\dfrac{P_{u.T}}{P_{y.T}}$	$\dfrac{P_{u.T}}{P_{n.D.T(P)}}$	$\dfrac{P_{u.T}}{P_{n.D.T}^P}$
C200x140	0.65	0.70	0.42	0.1	1.05	0.76	0.72	0.72	1.12
				0.2	4.19	3.02	0.72	0.72	1.11
				0.3	9.43	6.74	0.71	0.71	1.11
				0.4	16.77	11.84	0.71	0.71	1.09
				0.5	26.20	18.20	0.69	0.69	1.08
				0.6	37.73	25.42	0.67	0.68	1.04
				0.7	51.35	33.02	0.64	0.68	1.00
				0.9	84.89	49.18	0.58	0.71	0.91
				1.1	126.81	64.09	0.51	0.73	0.90
				1.3	177.11	72.52	0.41	0.77	0.90
				1.6	268.29	82.58	0.31	0.83	0.93
				1.9	378.33	87.46	0.23	0.83	0.93
				2.2	507.24	89.56	0.18	0.81	0.93
				2.5	655.01	89.86	0.14	0.77	0.91
				2.8	821.64	88.84	0.11	0.73	0.89
				3.1	1007.14	86.14	0.09	0.68	0.86
				3.5	1283.81	81.48	0.06	0.61	0.80
C200x200	0.65	0.70	0.42	0.1	0.69	0.49	0.70	0.70	1.08
				0.2	2.78	1.93	0.70	0.70	1.08
				0.3	6.25	4.33	0.69	0.69	1.07
				0.4	11.11	7.62	0.69	0.69	1.06
				0.5	17.36	11.70	0.67	0.67	1.04
				0.6	25.00	16.34	0.65	0.66	1.01
				0.7	34.03	21.65	0.64	0.67	0.98
				0.9	56.25	33.76	0.60	0.74	0.94
				1.1	84.03	43.13	0.51	0.74	0.91
				1.3	117.36	49.59	0.42	0.80	0.93
				1.6	177.78	56.83	0.32	0.86	0.96
				1.9	250.70	60.45	0.24	0.87	0.98
				2.2	336.12	62.17	0.18	0.85	0.97
				2.5	434.04	63.18	0.15	0.82	0.97
				2.8	544.45	63.67	0.12	0.79	0.96
				3.1	667.37	63.83	0.10	0.76	0.96
				3.5	850.71	63.80	0.07	0.72	0.95
C200x280	0.65	0.70	0.42	0.1	0.46	0.31	0.68	0.68	1.05
				0.2	1.84	1.24	0.67	0.67	1.04
				0.3	4.14	2.76	0.67	0.67	1.03
				0.4	7.36	4.86	0.66	0.66	1.02
				0.5	11.50	7.50	0.65	0.65	1.01
				0.6	16.56	10.66	0.64	0.65	1.00
				0.7	22.54	14.32	0.64	0.67	0.98
				0.9	37.27	22.59	0.61	0.75	0.95
				1.1	55.67	28.01	0.50	0.73	0.90
				1.3	77.75	32.54	0.42	0.79	0.92
				1.6	117.78	37.47	0.32	0.86	0.96
				1.9	166.08	40.12	0.24	0.87	0.98
				2.2	222.67	41.42	0.19	0.85	0.98
				2.5	287.54	42.22	0.15	0.83	0.98
				2.8	360.69	42.71	0.12	0.80	0.98
				3.1	442.12	43.01	0.10	0.77	0.97
				3.5	563.58	43.29	0.08	0.74	0.97

Table A5: Numerical failure loads and their DSM estimates for the pinned lipped channel columns at 500°C.

Column	k_y	k_E	k_p	$\lambda_{D.T}$	$P_{y.T}$ (kN)	$P_{u.T}$ (kN)	$\dfrac{P_{u.T}}{P_{y.T}}$	$\dfrac{P_{u.T}}{P_{n.D.T(P)}}$	$\dfrac{P_{u.T}}{P_{n.D.T}^P}$
C200x140	0.53	0.60	0.36	0.1	0.90	0.67	0.75	0.75	1.10
				0.2	3.59	2.67	0.74	0.74	1.09
				0.3	8.08	5.97	0.74	0.74	1.09
				0.4	14.37	10.50	0.73	0.73	1.08
				0.5	22.46	16.16	0.72	0.72	1.06
				0.6	32.34	22.54	0.70	0.70	1.03
				0.7	44.02	29.43	0.67	0.71	0.98
				0.9	72.76	44.26	0.61	0.75	0.92
				1.1	108.69	56.58	0.52	0.75	0.91
				1.3	151.81	64.30	0.42	0.80	0.92
				1.6	229.96	72.66	0.32	0.85	0.94
				1.9	324.28	76.84	0.24	0.85	0.95
				2.2	434.77	78.53	0.18	0.83	0.95
				2.5	561.43	78.97	0.14	0.79	0.93
				2.8	704.26	78.48	0.11	0.75	0.92
				3.1	863.26	76.96	0.09	0.71	0.89
				3.5	1100.41	72.74	0.07	0.64	0.83
C200x200	0.53	0.60	0.36	0.1	0.60	0.43	0.73	0.73	1.07
				0.2	2.38	1.72	0.72	0.72	1.06
				0.3	5.36	3.85	0.72	0.72	1.06
				0.4	9.52	6.78	0.71	0.71	1.05
				0.5	14.88	10.41	0.70	0.70	1.03
				0.6	21.43	14.61	0.68	0.69	1.00
				0.7	29.17	19.40	0.67	0.70	0.98
				0.9	48.22	30.32	0.63	0.77	0.95
				1.1	72.03	37.70	0.52	0.76	0.91
				1.3	100.60	43.73	0.43	0.82	0.94
				1.6	152.38	49.65	0.33	0.88	0.97
				1.9	214.88	52.36	0.24	0.88	0.98
				2.2	288.10	53.89	0.19	0.86	0.98
				2.5	372.03	54.57	0.15	0.83	0.97
				2.8	466.68	54.99	0.12	0.80	0.97
				3.1	572.03	55.16	0.10	0.77	0.96
				3.5	729.18	55.23	0.08	0.73	0.96
C200x280	0.53	0.60	0.36	0.1	0.39	0.28	0.70	0.70	1.04
				0.2	1.58	1.10	0.70	0.70	1.03
				0.3	3.55	2.47	0.70	0.70	1.02
				0.4	6.31	4.35	0.69	0.69	1.02
				0.5	9.86	6.73	0.68	0.68	1.00
				0.6	14.20	9.58	0.67	0.68	0.99
				0.7	19.32	12.89	0.67	0.71	0.98
				0.9	31.94	20.10	0.63	0.77	0.95
				1.1	47.72	24.43	0.51	0.74	0.89
				1.3	66.64	28.58	0.43	0.81	0.93
				1.6	100.95	32.64	0.32	0.87	0.97
				1.9	142.36	34.71	0.24	0.88	0.98
				2.2	190.86	35.80	0.19	0.86	0.98
				2.5	246.46	36.41	0.15	0.83	0.98
				2.8	309.16	36.74	0.12	0.80	0.98
				3.1	378.96	37.02	0.10	0.78	0.98
				3.5	483.07	37.30	0.08	0.74	0.98

Table A6: Numerical failure loads and their DSM estimates for the pinned lipped channel columns at 600°C.

Column	k_y	k_E	k_p	$\lambda_{D.T}$	$P_{y.T}$ (kN)	$P_{u.T}$ (kN)	$\dfrac{P_{u.T}}{P_{y.T}}$	$\dfrac{P_{u.T}}{P_{n.D.T(P)}}$	$\dfrac{P_{u.T}}{P_{n.D.T}^P}$
C200x140	0.30	0.31	0.18	0.1	0.46	0.32	0.69	0.69	1.15
				0.2	1.86	1.27	0.68	0.68	1.14
				0.3	4.18	2.83	0.68	0.68	1.13
				0.4	7.43	4.98	0.67	0.67	1.12
				0.5	11.60	7.64	0.66	0.66	1.10
				0.6	16.71	10.70	0.64	0.64	1.07
				0.7	22.74	13.89	0.61	0.65	1.02
				0.9	37.59	20.36	0.54	0.67	0.91
				1.1	56.16	26.89	0.48	0.69	0.88
				1.3	78.44	31.05	0.40	0.75	0.89
				1.6	118.81	34.96	0.29	0.80	0.90
				1.9	167.55	37.24	0.22	0.80	0.91
				2.2	224.63	38.06	0.17	0.78	0.90
				2.5	290.07	37.95	0.13	0.74	0.88
				2.8	363.87	37.19	0.10	0.69	0.85
				3.1	446.02	36.15	0.08	0.64	0.81
				3.5	568.54	33.08	0.06	0.56	0.74
C200x200	0.30	0.31	0.18	0.1	0.31	0.20	0.66	0.66	1.11
				0.2	1.23	0.81	0.66	0.66	1.10
				0.3	2.77	1.81	0.65	0.65	1.09
				0.4	4.92	3.19	0.65	0.65	1.08
				0.5	7.69	4.89	0.64	0.64	1.06
				0.6	11.07	6.83	0.62	0.62	1.03
				0.7	15.07	8.98	0.60	0.63	0.99
				0.9	24.91	13.92	0.56	0.69	0.93
				1.1	37.21	18.38	0.49	0.71	0.91
				1.3	51.98	21.02	0.40	0.76	0.91
				1.6	78.73	24.49	0.31	0.84	0.95
				1.9	111.02	26.11	0.24	0.85	0.96
				2.2	148.85	27.13	0.18	0.84	0.97
				2.5	192.22	27.49	0.14	0.81	0.96
				2.8	241.12	27.80	0.12	0.78	0.95
				3.1	295.55	27.88	0.09	0.75	0.95
				3.5	376.74	27.79	0.07	0.71	0.94
C200x280	0.30	0.31	0.18	0.1	0.20	0.13	0.64	0.64	1.06
				0.2	0.81	0.51	0.63	0.63	1.05
				0.3	1.83	1.15	0.62	0.62	1.04
				0.4	3.26	2.02	0.62	0.62	1.03
				0.5	5.09	3.11	0.61	0.61	1.02
				0.6	7.33	4.41	0.60	0.60	1.00
				0.7	9.98	5.90	0.59	0.63	0.99
				0.9	16.50	9.39	0.57	0.70	0.95
				1.1	24.65	12.06	0.49	0.71	0.90
				1.3	34.43	13.82	0.40	0.76	0.90
				1.6	52.16	16.19	0.31	0.84	0.95
				1.9	73.55	17.42	0.24	0.85	0.97
				2.2	98.61	18.06	0.18	0.84	0.97
				2.5	127.34	18.43	0.14	0.82	0.97
				2.8	159.73	18.73	0.12	0.79	0.97
				3.1	195.80	18.92	0.10	0.77	0.97
				3.5	249.58	19.03	0.08	0.73	0.97

Table A7: Numerical failure loads and their DSM estimates for the pinned lipped channel columns at 700°C.

Column	k_y	k_E	k_p	$\lambda_{D.T}$	$P_{y.T}$ (kN)	$P_{u.T}$ (kN)	$\dfrac{P_{u.T}}{P_{y.T}}$	$\dfrac{P_{u.T}}{P_{n.D.T(P)}}$	$\dfrac{P_{u.T}}{P_{n.D.T}^P}$
C200x140	0.13	0.13	0.075	0.1	0.19	0.13	0.67	0.67	1.17
				0.2	0.78	0.52	0.67	0.67	1.16
				0.3	1.75	1.16	0.66	0.66	1.15
				0.4	3.11	2.03	0.65	0.65	1.13
				0.5	4.87	3.12	0.64	0.64	1.11
				0.6	7.01	4.37	0.62	0.63	1.08
				0.7	9.54	5.69	0.60	0.63	1.03
				0.9	15.77	8.27	0.52	0.65	0.91
				1.1	23.55	10.88	0.46	0.67	0.87
				1.3	32.89	12.74	0.39	0.73	0.88
				1.6	49.83	14.29	0.29	0.78	0.88
				1.9	70.26	15.25	0.22	0.78	0.89
				2.2	94.20	15.59	0.17	0.76	0.88
				2.5	121.64	15.52	0.13	0.72	0.86
				2.8	152.59	15.21	0.10	0.67	0.83
				3.1	187.04	14.70	0.08	0.62	0.79
				3.5	238.42	13.31	0.06	0.54	0.71
C200x200	0.13	0.13	0.075	0.1	0.13	0.08	0.64	0.64	1.12
				0.2	0.52	0.33	0.64	0.64	1.11
				0.3	1.16	0.74	0.64	0.64	1.10
				0.4	2.06	1.30	0.63	0.63	1.09
				0.5	3.22	1.99	0.62	0.62	1.07
				0.6	4.64	2.78	0.60	0.60	1.04
				0.7	6.32	3.65	0.58	0.61	1.00
				0.9	10.45	5.62	0.54	0.66	0.93
				1.1	15.61	7.54	0.48	0.70	0.91
				1.3	21.80	8.63	0.40	0.75	0.90
				1.6	33.02	10.03	0.30	0.82	0.94
				1.9	46.56	10.85	0.23	0.84	0.96
				2.2	62.42	11.16	0.18	0.82	0.95
				2.5	80.61	11.38	0.14	0.80	0.95
				2.8	101.11	11.51	0.11	0.77	0.94
				3.1	123.94	11.55	0.09	0.74	0.94
				3.5	157.99	11.49	0.07	0.70	0.92
C200x280	0.13	0.13	0.075	0.1	0.09	0.05	0.62	0.62	1.07
				0.2	0.34	0.21	0.61	0.61	1.06
				0.3	0.77	0.46	0.60	0.60	1.05
				0.4	1.37	0.82	0.60	0.60	1.04
				0.5	2.14	1.26	0.59	0.59	1.02
				0.6	3.08	1.78	0.58	0.58	1.00
				0.7	4.19	2.38	0.57	0.60	0.99
				0.9	6.92	3.79	0.55	0.67	0.95
				1.1	10.34	4.96	0.48	0.69	0.91
				1.3	14.44	5.68	0.39	0.74	0.89
				1.6	21.87	6.67	0.31	0.82	0.94
				1.9	30.84	7.25	0.23	0.85	0.96
				2.2	41.35	7.49	0.18	0.83	0.96
				2.5	53.40	7.74	0.15	0.82	0.97
				2.8	66.99	7.75	0.12	0.78	0.96
				3.1	82.11	7.85	0.10	0.76	0.96
				3.5	104.66	7.95	0.08	0.73	0.96

Table A8: Numerical failure loads and their DSM estimates for the pinned lipped channel columns at 800ºC.

Column	k_y	k_E	k_p	$\lambda_{D.T}$	$P_{y.T}$ (kN)	$P_{u.T}$ (kN)	$\dfrac{P_{u.T}}{P_{y.T}}$	$\dfrac{P_{u.T}}{P_{n.D.T(P)}}$	$\dfrac{P_{u.T}}{P_{n.D.T}^{P}}$
C200x140	0.07	0.09	0.05	0.1	0.13	0.10	0.77	0.77	1.08
				0.2	0.54	0.41	0.77	0.77	1.07
				0.3	1.21	0.93	0.76	0.76	1.07
				0.4	2.16	1.63	0.76	0.76	1.06
				0.5	3.37	2.50	0.74	0.74	1.04
				0.6	4.85	3.51	0.72	0.73	1.01
				0.7	6.60	4.59	0.69	0.73	0.97
				0.9	10.91	6.98	0.64	0.79	0.94
				1.1	16.30	8.68	0.53	0.77	0.91
				1.3	22.77	9.97	0.44	0.83	0.93
				1.6	34.49	11.20	0.32	0.88	0.96
				1.9	48.64	11.66	0.24	0.86	0.96
				2.2	65.22	11.98	0.18	0.84	0.96
				2.5	84.21	12.09	0.14	0.81	0.95
				2.8	105.64	12.06	0.11	0.77	0.94
				3.1	129.49	11.91	0.09	0.73	0.92
				3.5	165.06	11.49	0.07	0.67	0.88
C200x200	0.07	0.09	0.05	0.1	0.09	0.07	0.75	0.75	1.06
				0.2	0.36	0.27	0.75	0.75	1.05
				0.3	0.80	0.60	0.75	0.75	1.04
				0.4	1.43	1.05	0.74	0.74	1.03
				0.5	2.23	1.62	0.73	0.73	1.02
				0.6	3.21	2.29	0.71	0.72	1.00
				0.7	4.38	3.06	0.70	0.74	0.98
				0.9	7.23	4.74	0.65	0.81	0.96
				1.1	10.80	5.76	0.53	0.77	0.91
				1.3	15.09	6.73	0.45	0.84	0.95
				1.6	22.86	7.50	0.33	0.89	0.97
				1.9	32.23	7.96	0.25	0.89	0.99
				2.2	43.22	8.02	0.19	0.85	0.97
				2.5	55.80	8.23	0.15	0.83	0.98
				2.8	70.00	8.30	0.12	0.80	0.97
				3.1	85.81	8.30	0.10	0.77	0.97
				3.5	109.38	8.30	0.08	0.73	0.96
C200x280	0.07	0.09	0.05	0.1	0.06	0.04	0.73	0.73	1.03
				0.2	0.24	0.17	0.73	0.73	1.02
				0.3	0.53	0.39	0.73	0.73	1.02
				0.4	0.95	0.68	0.72	0.72	1.01
				0.5	1.48	1.06	0.72	0.72	1.00
				0.6	2.13	1.51	0.71	0.71	0.99
				0.7	2.90	2.03	0.70	0.74	0.98
				0.9	4.79	3.12	0.65	0.80	0.95
				1.1	7.16	3.74	0.52	0.75	0.89
				1.3	10.00	4.39	0.44	0.83	0.94
				1.6	15.14	4.86	0.32	0.87	0.95
				1.9	21.35	5.26	0.25	0.89	0.98
				2.2	28.63	5.33	0.19	0.85	0.97
				2.5	36.97	5.48	0.15	0.84	0.98
				2.8	46.37	5.49	0.12	0.80	0.97
				3.1	56.84	5.57	0.10	0.78	0.98
				3.5	72.46	5.62	0.08	0.75	0.98

Table A9: Numerical failure loads and their DSM estimates for the fixed lipped channel columns at 100ºC.

Column	k_y	k_E	k_p	$\lambda_{D.T}$	$P_{y.T}$ (kN)	$P_{u.T}$ (kN)	$\dfrac{P_{u.T}}{P_{y.T}}$	$\dfrac{P_{u.T}}{P_{n.D.T(F)}}$	$\dfrac{P_{u.T}}{P_{n.D.T}^F}$
C200x140	1.00	1.00	1.00	0.1	2.15	2.15	1.00	1.00	1.00
				0.2	8.59	8.59	1.00	1.00	1.00
				0.3	19.33	19.32	1.00	1.00	1.00
				0.4	34.37	34.33	1.00	1.00	1.00
				0.5	53.70	53.56	1.00	1.00	1.00
				0.6	77.33	76.92	0.99	1.00	1.00
				0.7	105.26	104.19	0.99	1.05	1.02
				0.9	174.00	161.61	0.93	1.14	1.13
				1.1	259.93	190.67	0.73	1.06	1.07
				1.3	363.04	216.66	0.60	1.00	1.04
				1.6	549.94	250.41	0.46	0.93	1.01
				1.9	775.50	298.42	0.38	0.94	1.05
				2.2	1039.72	347.37	0.33	0.95	1.10
				2.5	1342.62	395.04	0.29	0.96	1.14
				2.8	1684.18	440.20	0.26	0.97	1.17
				3.1	2064.41	483.48	0.23	0.97	1.20
				3.5	2631.53	537.98	0.20	0.97	1.23
C200x200	1.00	1.00	1.00	0.1	1.52	1.52	1.00	1.00	1.00
				0.2	6.07	6.07	1.00	1.00	1.00
				0.3	13.66	13.65	1.00	1.00	1.00
				0.4	24.28	24.24	1.00	1.00	1.00
				0.5	37.94	37.82	1.00	1.00	1.00
				0.6	54.64	54.30	0.99	1.00	0.99
				0.7	74.37	73.46	0.99	1.04	1.02
				0.9	122.93	113.63	0.92	1.14	1.12
				1.1	183.64	129.61	0.71	1.02	1.03
				1.3	256.49	147.98	0.58	0.97	1.01
				1.6	388.53	185.53	0.48	0.98	1.06
				1.9	547.89	219.58	0.40	0.98	1.10
				2.2	734.57	256.71	0.35	1.00	1.15
				2.5	948.56	294.14	0.31	1.02	1.20
				2.8	1189.88	330.90	0.28	1.03	1.25
				3.1	1458.51	366.61	0.25	1.04	1.29
				3.5	1859.19	412.60	0.22	1.06	1.34
C200x280	1.00	1.00	1.00	0.1	1.08	1.08	1.00	1.00	1.00
				0.2	4.31	4.31	1.00	1.00	1.00
				0.3	9.70	9.68	1.00	1.00	1.00
				0.4	17.24	17.19	1.00	1.00	1.00
				0.5	26.93	26.79	0.99	0.99	0.99
				0.6	38.78	38.47	0.99	1.00	0.99
				0.7	52.79	51.97	0.98	1.04	1.02
				0.9	87.26	77.97	0.89	1.10	1.09
				1.1	130.35	87.47	0.67	0.97	0.98
				1.3	182.06	96.44	0.53	0.92	0.96
				1.6	275.79	134.53	0.49	1.00	1.08
				1.9	388.91	165.31	0.43	1.04	1.16
				2.2	521.41	193.32	0.37	1.06	1.22
				2.5	673.31	220.68	0.33	1.07	1.27
				2.8	844.60	248.10	0.29	1.09	1.32
				3.1	1035.29	275.67	0.27	1.11	1.37
				3.5	1319.70	312.34	0.24	1.13	1.43

Table A10: Numerical failure loads and their DSM estimates for the fixed lipped channel columns at 200ºC.

Column	k_y	k_E	k_p	$\lambda_{D.T}$	$P_{y.T}$ (kN)	$P_{u.T}$ (kN)	$\dfrac{P_{u.T}}{P_{y.T}}$	$\dfrac{P_{u.T}}{P_{n.D.T(F)}}$	$\dfrac{P_{u.T}}{P_{n.D.T}^{F}}$
C200x140	0.89	0.90	0.807	0.1	1.93	1.78	0.92	0.92	1.01
				0.2	7.73	7.00	0.90	0.90	1.00
				0.3	17.40	15.72	0.90	0.90	1.00
				0.4	30.93	28.07	0.91	0.91	1.00
				0.5	48.33	43.53	0.90	0.90	0.99
				0.6	69.60	62.25	0.89	0.90	0.99
				0.7	94.74	83.35	0.88	0.93	0.98
				0.9	156.60	132.03	0.84	1.04	1.07
				1.1	233.94	168.23	0.72	1.04	1.08
				1.3	326.74	188.04	0.58	0.96	1.03
				1.6	494.94	208.93	0.42	0.86	0.95
				1.9	697.95	239.38	0.34	0.84	0.95
				2.2	935.75	269.51	0.29	0.82	0.96
				2.5	1208.36	298.12	0.25	0.81	0.96
				2.8	1515.76	324.87	0.21	0.80	0.97
				3.1	1857.97	349.03	0.19	0.78	0.97
				3.5	2368.38	377.63	0.16	0.76	0.97
C200x200	0.89	0.90	0.807	0.1	1.37	1.24	0.91	0.91	1.00
				0.2	5.46	4.95	0.91	0.91	1.00
				0.3	12.29	11.15	0.91	0.91	1.00
				0.4	21.85	19.77	0.90	0.90	1.00
				0.5	34.15	30.74	0.90	0.90	0.99
				0.6	49.17	43.99	0.89	0.90	0.99
				0.7	66.93	59.39	0.89	0.94	0.99
				0.9	110.64	93.97	0.85	1.04	1.08
				1.1	165.28	117.49	0.71	1.03	1.07
				1.3	230.84	129.44	0.56	0.94	1.00
				1.6	349.68	156.11	0.45	0.91	1.01
				1.9	493.10	181.83	0.37	0.90	1.02
				2.2	661.11	208.70	0.32	0.90	1.05
				2.5	853.71	235.16	0.28	0.90	1.08
				2.8	1070.89	260.11	0.24	0.90	1.10
				3.1	1312.66	283.93	0.22	0.90	1.12
				3.5	1673.27	313.53	0.19	0.89	1.14
C200x280	0.89	0.90	0.807	0.1	0.97	0.88	0.91	0.91	1.00
				0.2	3.88	3.52	0.91	0.91	1.00
				0.3	8.73	7.90	0.91	0.91	1.00
				0.4	15.51	14.01	0.90	0.90	1.00
				0.5	24.24	21.82	0.90	0.90	0.99
				0.6	34.90	31.28	0.90	0.90	0.99
				0.7	47.51	42.26	0.89	0.94	0.99
				0.9	78.54	65.86	0.84	1.03	1.06
				1.1	117.32	77.97	0.66	0.99	1.04
				1.3	163.86	84.11	0.51	0.90	0.96
				1.6	248.21	112.37	0.45	0.93	1.02
				1.9	350.02	137.73	0.39	0.96	1.09
				2.2	469.27	160.93	0.34	0.98	1.14
				2.5	605.98	182.59	0.30	0.99	1.18
				2.8	760.14	203.46	0.27	0.99	1.21
				3.1	931.76	223.55	0.24	1.00	1.24
				3.5	1187.73	249.36	0.21	1.00	1.27

Table A11: Numerical failure loads and their DSM estimates for the fixed lipped channel columns at 300ºC.

Column	k_y	k_E	k_p	$\lambda_{D.T}$	$P_{y.T}$ (kN)	$P_{u.T}$ (kN)	$\dfrac{P_{u.T}}{P_{y.T}}$	$\dfrac{P_{u.T}}{P_{n.D.T(F)}}$	$\dfrac{P_{u.T}}{P_{n.D.T}^F}$
C200x140	0.78	0.80	0.613	0.1	1.72	1.42	0.83	0.83	1.05
				0.2	6.87	5.65	0.82	0.82	1.05
				0.3	15.47	12.63	0.82	0.82	1.04
				0.4	27.50	22.27	0.81	0.81	1.03
				0.5	42.96	34.42	0.80	0.80	1.02
				0.6	61.87	48.47	0.78	0.79	1.00
				0.7	84.21	64.11	0.76	0.80	0.97
				0.9	139.20	98.66	0.71	0.87	0.97
				1.1	207.94	133.81	0.64	0.93	1.02
				1.3	290.44	155.78	0.54	0.90	0.99
				1.6	439.95	172.97	0.39	0.81	0.91
				1.9	620.40	184.77	0.30	0.77	0.89
				2.2	831.78	212.81	0.26	0.73	0.86
				2.5	1074.09	240.73	0.22	0.73	0.89
				2.8	1347.34	268.01	0.20	0.74	0.91
				3.1	1651.53	294.56	0.18	0.74	0.93
				3.5	2105.23	323.25	0.15	0.73	0.94
C200x200	0.78	0.80	0.613	0.1	1.21	0.99	0.81	0.81	1.03
				0.2	4.86	3.94	0.81	0.81	1.03
				0.3	10.93	8.81	0.81	0.81	1.03
				0.4	19.43	15.55	0.80	0.80	1.02
				0.5	30.35	23.54	0.78	0.78	0.99
				0.6	43.71	33.46	0.77	0.77	0.97
				0.7	59.49	45.36	0.76	0.81	0.97
				0.9	98.35	72.01	0.73	0.90	1.00
				1.1	146.91	97.03	0.66	0.95	1.05
				1.3	205.19	109.95	0.54	0.90	0.99
				1.6	310.83	125.16	0.40	0.83	0.93
				1.9	438.31	145.05	0.33	0.81	0.93
				2.2	587.65	160.67	0.27	0.78	0.92
				2.5	758.85	182.69	0.24	0.79	0.95
				2.8	951.90	204.46	0.21	0.80	0.98
				3.1	1166.81	226.03	0.19	0.80	1.01
				3.5	1487.35	253.92	0.17	0.81	1.04
C200x280	0.78	0.80	0.613	0.1	0.86	0.69	0.80	0.80	1.02
				0.2	3.45	2.75	0.80	0.80	1.01
				0.3	7.76	6.16	0.79	0.79	1.01
				0.4	13.79	10.86	0.79	0.79	1.00
				0.5	21.55	16.83	0.78	0.78	0.99
				0.6	31.03	24.02	0.77	0.78	0.99
				0.7	42.23	32.38	0.77	0.81	0.98
				0.9	69.81	51.75	0.74	0.91	1.01
				1.1	104.28	66.25	0.64	0.92	1.01
				1.3	145.65	72.84	0.50	0.84	0.93
				1.6	220.63	89.79	0.41	0.83	0.94
				1.9	311.12	109.61	0.35	0.86	0.99
				2.2	417.13	127.41	0.31	0.87	1.03
				2.5	538.65	143.17	0.27	0.87	1.05
				2.8	675.68	157.37	0.23	0.86	1.06
				3.1	828.23	173.60	0.21	0.87	1.09
				3.5	1055.76	195.61	0.19	0.88	1.13

Table A12: Numerical failure loads and their DSM estimates for the fixed lipped channel columns at 400ºC.

Column	k_y	k_E	k_p	$\lambda_{D.T}$	$P_{y.T}$ (kN)	$P_{u.T}$ (kN)	$\dfrac{P_{u.T}}{P_{y.T}}$	$\dfrac{P_{u.T}}{P_{n.D.T(F)}}$	$\dfrac{P_{u.T}}{P_{n.D.T}^{F}}$
C200x140	0.65	0.70	0.42	0.1	1.50	1.10	0.73	0.73	1.13
				0.2	6.01	4.36	0.72	0.72	1.12
				0.3	13.53	9.72	0.72	0.72	1.11
				0.4	24.06	17.07	0.71	0.71	1.10
				0.5	37.59	26.28	0.70	0.70	1.08
				0.6	54.13	37.07	0.68	0.69	1.06
				0.7	73.68	49.30	0.67	0.71	1.04
				0.9	121.80	72.67	0.60	0.73	0.93
				1.1	181.95	93.20	0.51	0.78	0.93
				1.3	254.13	113.32	0.45	0.75	0.88
				1.6	384.96	131.69	0.34	0.70	0.83
				1.9	542.85	138.57	0.26	0.65	0.78
				2.2	727.81	138.11	0.19	0.63	0.77
				2.5	939.83	216.01	0.23	0.75	0.93
				2.8	1178.93	230.47	0.20	0.73	0.91
				3.1	1445.09	255.59	0.18	0.73	0.94
				3.5	1842.07	286.57	0.16	0.74	0.96
C200x200	0.65	0.70	0.42	0.1	1.06	0.75	0.71	0.71	1.09
				0.2	4.25	2.98	0.70	0.70	1.09
				0.3	9.56	6.65	0.70	0.70	1.08
				0.4	17.00	11.72	0.69	0.69	1.07
				0.5	26.56	18.09	0.68	0.68	1.05
				0.6	38.25	25.54	0.67	0.67	1.03
				0.7	52.06	33.56	0.64	0.68	1.00
				0.9	86.05	51.52	0.60	0.74	0.94
				1.1	128.55	71.00	0.55	0.80	0.95
				1.3	179.54	87.56	0.49	0.82	0.96
				1.6	271.97	99.42	0.37	0.75	0.88
				1.9	383.52	109.43	0.29	0.70	0.83
				2.2	514.20	119.10	0.23	0.67	0.82
				2.5	663.99	145.65	0.22	0.72	0.89
				2.8	832.91	166.03	0.20	0.74	0.93
				3.1	1020.96	186.20	0.18	0.76	0.97
				3.5	1301.43	212.76	0.16	0.78	1.01
C200x280	0.65	0.70	0.42	0.1	0.75	0.51	0.68	0.68	1.05
				0.2	3.02	2.05	0.68	0.68	1.05
				0.3	6.79	4.59	0.68	0.68	1.05
				0.4	12.07	8.07	0.67	0.67	1.03
				0.5	18.85	12.40	0.66	0.66	1.02
				0.6	27.15	17.51	0.65	0.65	1.00
				0.7	36.95	23.41	0.63	0.67	0.98
				0.9	61.08	37.14	0.61	0.75	0.95
				1.1	91.25	51.84	0.57	0.82	0.98
				1.3	127.44	60.23	0.47	0.79	0.93
				1.6	193.05	68.37	0.35	0.73	0.86
				1.9	272.23	83.34	0.31	0.75	0.89
				2.2	364.99	96.42	0.26	0.75	0.91
				2.5	471.32	108.73	0.23	0.76	0.93
				2.8	591.22	122.66	0.21	0.77	0.97
				3.1	724.70	137.23	0.19	0.79	1.00
				3.5	923.79	157.35	0.17	0.81	1.05

Table A13: Numerical failure loads and their DSM estimates for the fixed lipped channel columns at 500ºC.

Column	k_y	k_E	k_p	$\lambda_{D.T}$	$P_{y.T}$ (kN)	$P_{u.T}$ (kN)	$\dfrac{P_{u.T}}{P_{y.T}}$	$\dfrac{P_{u.T}}{P_{n.D.T(F)}}$	$\dfrac{P_{u.T}}{P_{n.D.T}^{F}}$
C200x140	0.53	0.60	0.36	0.1	1.29	0.97	0.75	0.75	1.11
				0.2	5.16	3.85	0.75	0.75	1.10
				0.3	11.60	8.58	0.74	0.74	1.09
				0.4	20.62	15.10	0.73	0.73	1.08
				0.5	32.22	23.25	0.72	0.72	1.06
				0.6	46.40	32.91	0.71	0.71	1.04
				0.7	63.16	43.31	0.69	0.73	1.01
				0.9	104.40	64.44	0.62	0.76	0.93
				1.1	155.96	85.96	0.55	0.80	0.93
				1.3	217.83	102.97	0.47	0.79	0.92
				1.6	329.96	118.31	0.36	0.73	0.86
				1.9	465.30	124.08	0.27	0.68	0.80
				2.2	623.83	124.86	0.20	0.64	0.77
				2.5	805.57	184.36	0.23	0.75	0.92
				2.8	1010.51	198.04	0.20	0.73	0.91
				3.1	1238.65	219.58	0.18	0.74	0.93
				3.5	1578.92	245.99	0.16	0.74	0.96
C200x200	0.53	0.60	0.36	0.1	0.91	0.66	0.72	0.72	1.06
				0.2	3.64	2.64	0.73	0.73	1.07
				0.3	8.20	5.91	0.72	0.72	1.06
				0.4	14.57	10.35	0.71	0.71	1.05
				0.5	22.77	16.09	0.71	0.71	1.04
				0.6	32.78	22.59	0.69	0.69	1.01
				0.7	44.62	29.88	0.67	0.71	0.99
				0.9	73.76	46.75	0.63	0.78	0.95
				1.1	110.19	64.08	0.58	0.84	0.98
				1.3	153.89	77.31	0.50	0.84	0.97
				1.6	233.12	87.08	0.37	0.77	0.89
				1.9	328.73	97.37	0.30	0.72	0.86
				2.2	440.74	106.39	0.24	0.69	0.83
				2.5	569.14	127.16	0.22	0.73	0.90
				2.8	713.93	144.38	0.20	0.75	0.94
				3.1	875.11	161.40	0.18	0.77	0.97
				3.5	1115.51	183.70	0.16	0.78	1.02
C200x280	0.53	0.60	0.36	0.1	0.65	0.46	0.71	0.71	1.05
				0.2	2.59	1.83	0.71	0.71	1.04
				0.3	5.82	4.09	0.70	0.70	1.03
				0.4	10.34	7.20	0.70	0.70	1.02
				0.5	16.16	11.08	0.69	0.69	1.01
				0.6	23.27	15.69	0.67	0.68	0.99
				0.7	31.67	21.01	0.66	0.70	0.98
				0.9	52.36	33.50	0.64	0.79	0.96
				1.1	78.21	46.13	0.59	0.85	0.99
				1.3	109.24	52.43	0.48	0.80	0.93
				1.6	165.47	60.66	0.37	0.75	0.87
				1.9	233.34	73.91	0.32	0.77	0.92
				2.2	312.85	85.58	0.27	0.78	0.94
				2.5	403.99	95.74	0.24	0.78	0.95
				2.8	506.76	107.85	0.21	0.79	0.99
				3.1	621.17	120.12	0.19	0.80	1.02
				3.5	791.82	137.20	0.17	0.82	1.07

Table A14: Numerical failure loads and their DSM estimates for the fixed lipped channel columns at 600ºC.

Column	k_y	k_E	k_p	$\lambda_{D.T}$	$P_{y.T}$ (kN)	$P_{u.T}$ (kN)	$\dfrac{P_{u.T}}{P_{y.T}}$	$\dfrac{P_{u.T}}{P_{n.D.T(F)}}$	$\dfrac{P_{u.T}}{P_{n.D.T}^{F}}$
C200x140	0.30	0.31	0.18	0.1	0.67	0.47	0.70	0.70	1.17
				0.2	2.66	1.85	0.69	0.69	1.16
				0.3	5.99	4.12	0.69	0.69	1.15
				0.4	10.66	7.22	0.68	0.68	1.13
				0.5	16.65	11.09	0.67	0.67	1.11
				0.6	23.97	15.64	0.65	0.66	1.09
				0.7	32.63	20.67	0.63	0.67	1.06
				0.9	53.94	30.86	0.57	0.70	0.95
				1.1	80.58	39.49	0.49	0.71	0.88
				1.3	112.54	46.50	0.41	0.72	0.87
				1.6	170.48	53.63	0.31	0.64	0.77
				1.9	240.40	56.30	0.23	0.63	0.77
				2.2	322.31	76.29	0.24	0.68	0.83
				2.5	416.21	89.67	0.22	0.71	0.88
				2.8	522.10	101.29	0.19	0.72	0.91
				3.1	639.97	112.42	0.18	0.73	0.94
				3.5	815.77	126.25	0.15	0.74	0.96
C200x200	0.30	0.31	0.18	0.1	0.47	0.32	0.67	0.67	1.12
				0.2	1.88	1.23	0.65	0.65	1.09
				0.3	4.23	2.73	0.65	0.65	1.08
				0.4	7.53	4.92	0.65	0.65	1.09
				0.5	11.76	7.59	0.64	0.64	1.07
				0.6	16.94	10.69	0.63	0.63	1.05
				0.7	23.05	14.08	0.61	0.65	1.02
				0.9	38.11	21.39	0.56	0.69	0.94
				1.1	56.93	29.09	0.51	0.74	0.92
				1.3	79.51	36.49	0.46	0.77	0.93
				1.6	120.44	42.66	0.35	0.73	0.87
				1.9	169.85	46.45	0.27	0.67	0.81
				2.2	227.72	49.78	0.22	0.62	0.77
				2.5	294.05	62.93	0.21	0.70	0.87
				2.8	368.86	72.09	0.20	0.73	0.92
				3.1	452.14	81.21	0.18	0.75	0.96
				3.5	576.35	93.24	0.16	0.77	1.01
C200x280	0.30	0.31	0.18	0.1	0.33	0.22	0.65	0.65	1.08
				0.2	1.34	0.86	0.64	0.64	1.07
				0.3	3.01	1.92	0.64	0.64	1.06
				0.4	5.34	3.37	0.63	0.63	1.05
				0.5	8.35	5.17	0.62	0.62	1.03
				0.6	12.02	7.27	0.60	0.61	1.01
				0.7	16.36	9.70	0.59	0.63	0.99
				0.9	27.05	15.28	0.56	0.69	0.94
				1.1	40.41	21.53	0.53	0.77	0.96
				1.3	56.44	25.98	0.46	0.77	0.93
				1.6	85.49	29.01	0.34	0.70	0.84
				1.9	120.56	35.00	0.29	0.71	0.86
				2.2	161.64	40.51	0.25	0.72	0.88
				2.5	208.73	46.36	0.22	0.73	0.91
				2.8	261.83	52.50	0.20	0.74	0.94
				3.1	320.94	59.06	0.18	0.76	0.98
				3.5	409.11	68.09	0.17	0.79	1.04

Table A15: Numerical failure loads and their DSM estimates for the fixed lipped channel columns at 700ºC.

Column	k_y	k_E	k_p	$\lambda_{D.T}$	$P_{y.T}$ (kN)	$P_{u.T}$ (kN)	$\dfrac{P_{u.T}}{P_{y.T}}$	$\dfrac{P_{u.T}}{P_{n.D.T(F)}}$	$\dfrac{P_{u.T}}{P_{n.D.T}^F}$
				0.1	0.28	0.19	0.69	0.69	1.19
				0.2	1.12	0.76	0.68	0.68	1.18
				0.3	2.51	1.69	0.67	0.67	1.16
				0.4	4.47	2.96	0.66	0.66	1.15
				0.5	6.98	4.55	0.65	0.65	1.13
				0.6	10.05	6.40	0.64	0.64	1.10
				0.7	13.68	8.49	0.62	0.66	1.08
C200x140	0.13	0.13	0.075	0.9	22.62	12.62	0.56	0.69	0.97
				1.1	33.79	16.12	0.48	0.69	0.88
				1.3	47.20	18.81	0.40	0.71	0.87
				1.6	71.49	21.55	0.30	0.65	0.79
				1.9	100.81	22.45	0.22	0.60	0.73
				2.2	135.16	31.94	0.24	0.67	0.83
				2.5	174.54	37.08	0.21	0.70	0.87
				2.8	218.94	42.00	0.19	0.71	0.90
				3.1	268.37	46.72	0.17	0.72	0.93
				3.5	342.10	52.19	0.15	0.73	0.95
				0.1	0.20	0.13	0.64	0.64	1.11
				0.2	0.79	0.51	0.65	0.65	1.13
				0.3	1.78	1.14	0.64	0.64	1.11
				0.4	3.16	2.01	0.64	0.64	1.11
				0.5	4.93	3.09	0.63	0.63	1.09
				0.6	7.10	4.37	0.62	0.62	1.07
				0.7	9.67	5.75	0.59	0.63	1.03
C200x200	0.13	0.13	0.075	0.9	15.98	8.73	0.55	0.67	0.95
				1.1	23.87	11.75	0.49	0.71	0.91
				1.3	33.34	14.72	0.44	0.74	0.91
				1.6	50.51	17.42	0.34	0.71	0.86
				1.9	71.23	18.89	0.27	0.65	0.79
				2.2	95.49	22.20	0.23	0.66	0.82
				2.5	123.31	25.96	0.21	0.69	0.86
				2.8	154.68	29.84	0.19	0.72	0.91
				3.1	189.61	33.68	0.18	0.74	0.95
				3.5	241.69	38.76	0.16	0.76	1.00
				0.1	0.14	0.09	0.63	0.63	1.09
				0.2	0.56	0.35	0.62	0.62	1.08
				0.3	1.26	0.78	0.62	0.62	1.07
				0.4	2.24	1.37	0.61	0.61	1.06
				0.5	3.50	2.10	0.60	0.60	1.04
				0.6	5.04	2.95	0.59	0.59	1.02
				0.7	6.86	3.94	0.57	0.61	0.99
C200x280	0.13	0.13	0.075	0.9	11.34	6.18	0.54	0.67	0.94
				1.1	16.95	8.70	0.51	0.74	0.94
				1.3	23.67	10.68	0.45	0.76	0.93
				1.6	35.85	12.24	0.34	0.70	0.85
				1.9	50.56	14.20	0.28	0.69	0.84
				2.2	67.78	16.50	0.24	0.69	0.86
				2.5	87.53	19.09	0.22	0.71	0.89
				2.8	109.80	21.66	0.20	0.73	0.93
				3.1	134.59	24.42	0.18	0.75	0.97
				3.5	171.56	28.21	0.16	0.78	1.03

Table A16: Numerical failure loads and their DSM estimates for the fixed lipped channel columns at 800°C.

Column	k_y	k_E	k_p	$\lambda_{D.T}$	$P_{y.T}$ (kN)	$P_{u.T}$ (kN)	$\dfrac{P_{u.T}}{P_{y.T}}$	$\dfrac{P_{u.T}}{P_{n.D.T(F)}}$	$\dfrac{P_{u.T}}{P_{n.D.T}^F}$
C200x140	0.07	0.09	0.05	0.1	0.19	0.15	0.78	0.78	1.09
				0.2	0.77	0.60	0.77	0.77	1.08
				0.3	1.74	1.33	0.76	0.76	1.07
				0.4	3.09	2.34	0.76	0.76	1.06
				0.5	4.83	3.61	0.75	0.75	1.04
				0.6	6.96	5.08	0.73	0.73	1.02
				0.7	9.47	6.71	0.71	0.75	0.99
				0.9	15.66	10.07	0.64	0.79	0.93
				1.1	23.39	13.47	0.58	0.83	0.95
				1.3	32.67	16.25	0.50	0.83	0.95
				1.6	49.49	18.06	0.36	0.75	0.86
				1.9	69.79	19.31	0.28	0.71	0.84
				2.2	93.58	19.72	0.21	0.65	0.78
				2.5	120.84	19.22	0.16	0.67	0.82
				2.8	151.58	18.23	0.12	0.68	0.85
				3.1	185.80	32.54	0.18	0.73	0.92
				3.5	236.84	36.45	0.15	0.73	0.95
C200x200	0.07	0.09	0.05	0.1	0.14	0.10	0.76	0.76	1.06
				0.2	0.55	0.41	0.75	0.75	1.05
				0.3	1.23	0.92	0.75	0.75	1.05
				0.4	2.19	1.63	0.74	0.74	1.04
				0.5	3.41	2.50	0.73	0.73	1.03
				0.6	4.92	3.54	0.72	0.72	1.01
				0.7	6.69	4.67	0.70	0.74	0.98
				0.9	11.06	7.27	0.66	0.81	0.95
				1.1	16.53	10.10	0.61	0.88	1.01
				1.3	23.08	11.92	0.52	0.87	0.98
				1.6	34.97	13.27	0.38	0.78	0.89
				1.9	49.31	15.12	0.31	0.75	0.88
				2.2	66.11	16.88	0.26	0.73	0.87
				2.5	85.37	19.33	0.23	0.74	0.90
				2.8	107.09	21.73	0.20	0.75	0.93
				3.1	131.27	24.31	0.19	0.77	0.97
				3.5	167.33	27.58	0.16	0.78	1.01
C200x280	0.07	0.09	0.05	0.1	0.10	0.07	0.74	0.74	1.04
				0.2	0.39	0.29	0.74	0.74	1.03
				0.3	0.87	0.64	0.73	0.73	1.02
				0.4	1.55	1.12	0.72	0.72	1.01
				0.5	2.42	1.74	0.72	0.72	1.00
				0.6	3.49	2.46	0.71	0.71	0.99
				0.7	4.75	3.31	0.70	0.74	0.97
				0.9	7.85	5.29	0.67	0.83	0.98
				1.1	11.73	7.06	0.60	0.87	0.99
				1.3	16.39	7.99	0.49	0.82	0.93
				1.6	24.82	9.39	0.38	0.78	0.89
				1.9	35.00	11.21	0.32	0.78	0.92
				2.2	46.93	13.23	0.28	0.80	0.96
				2.5	60.60	14.78	0.24	0.80	0.97
				2.8	76.01	16.49	0.22	0.80	1.00
				3.1	93.18	18.34	0.20	0.82	1.03
				3.5	118.77	20.83	0.18	0.84	1.08